

Synthesis of Nanoparticles and Surface Modifications

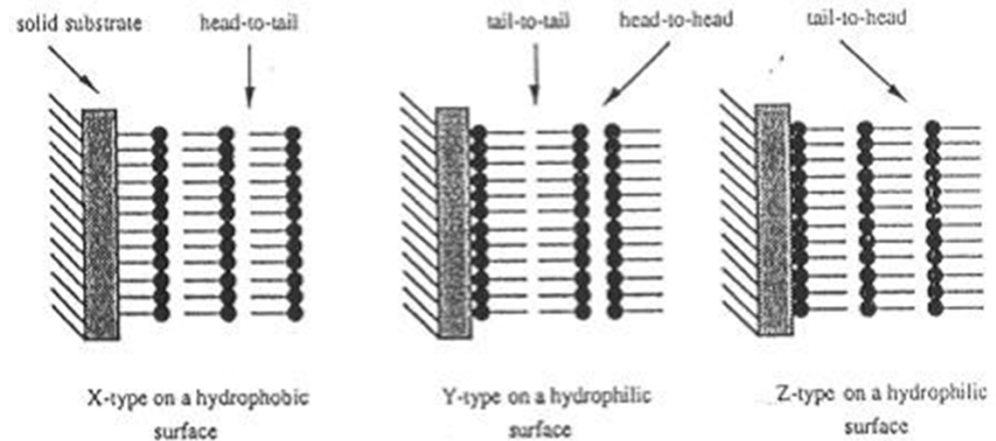
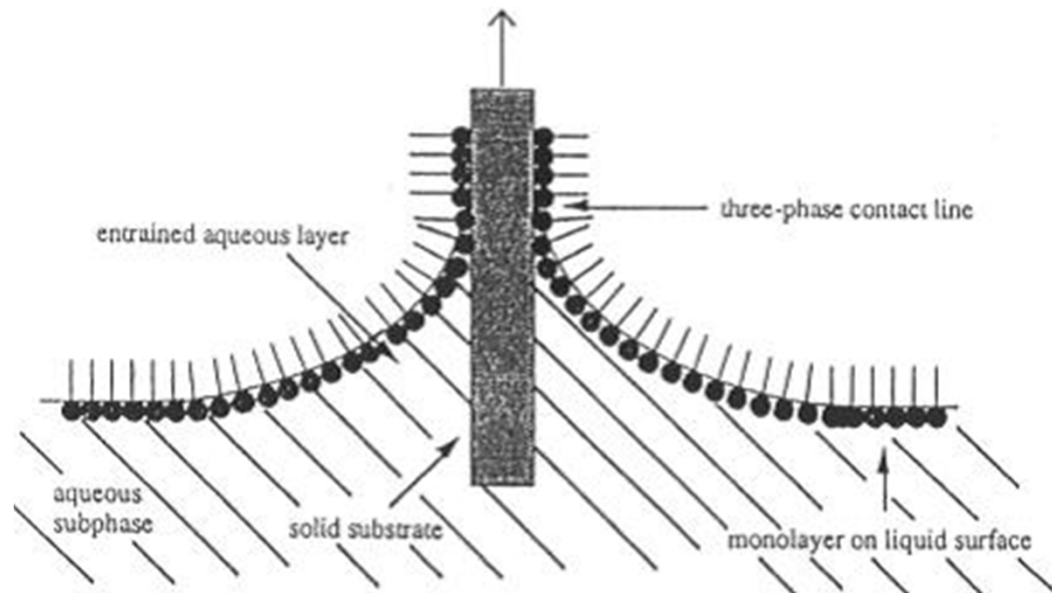
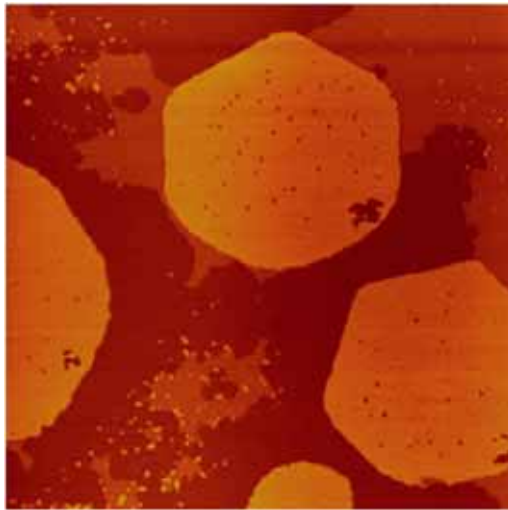


Self-Assembly

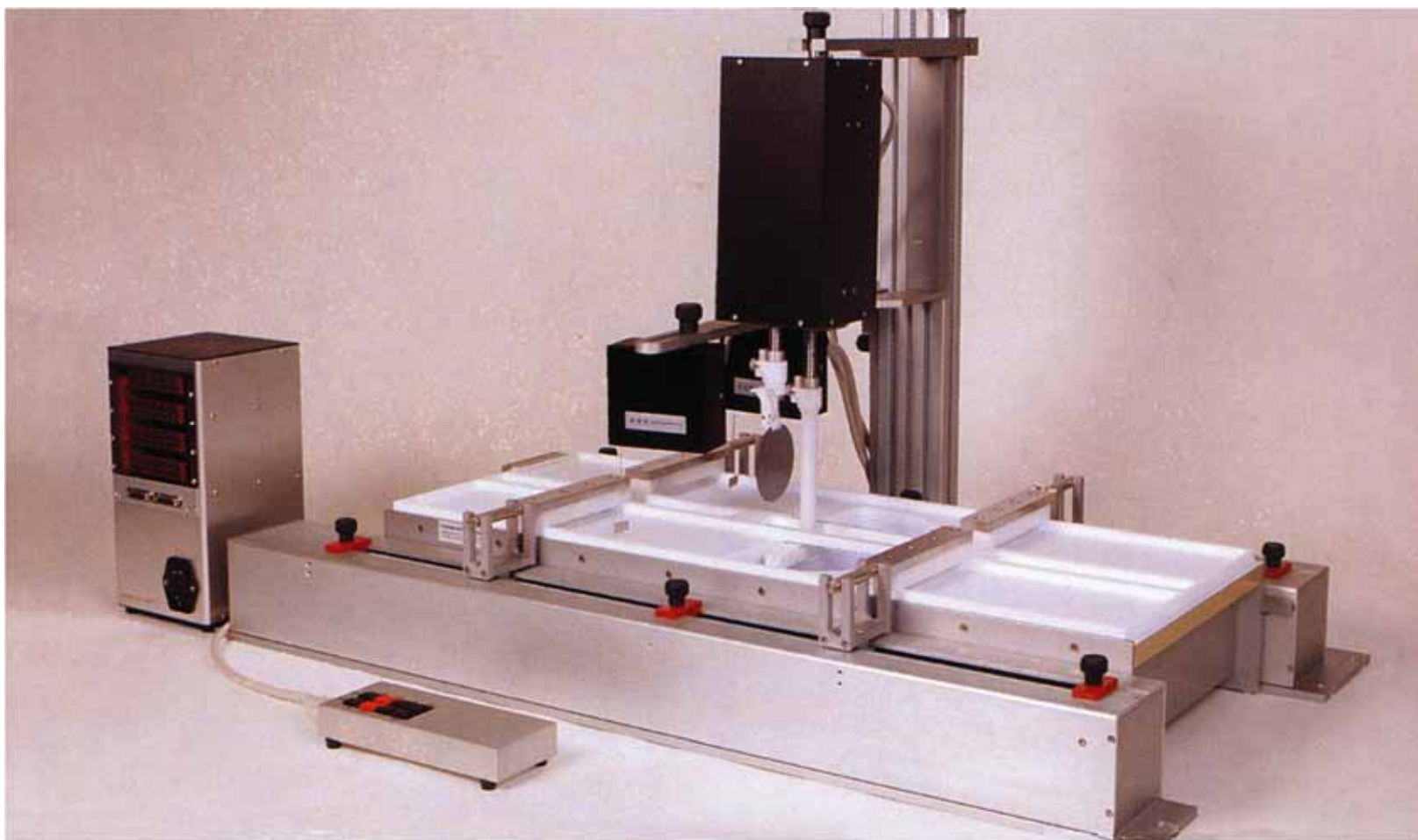
- Static assembly
- Dynamic assembly
 - $RT = 8.314 \text{ J/mol} \times 300 = 2.4 \text{ kJ/mol}$
- Driving forces
 - Chemisorption
 - Surface effect
 - Hydrophobic-hydrophilic
 - Intermolecular forces
 - Capillary force



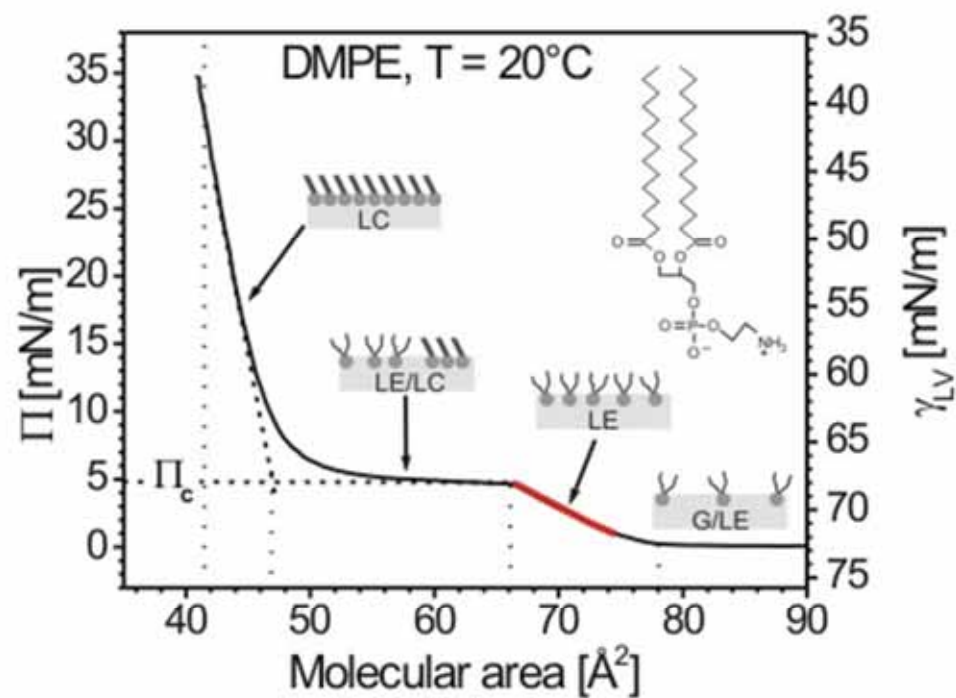
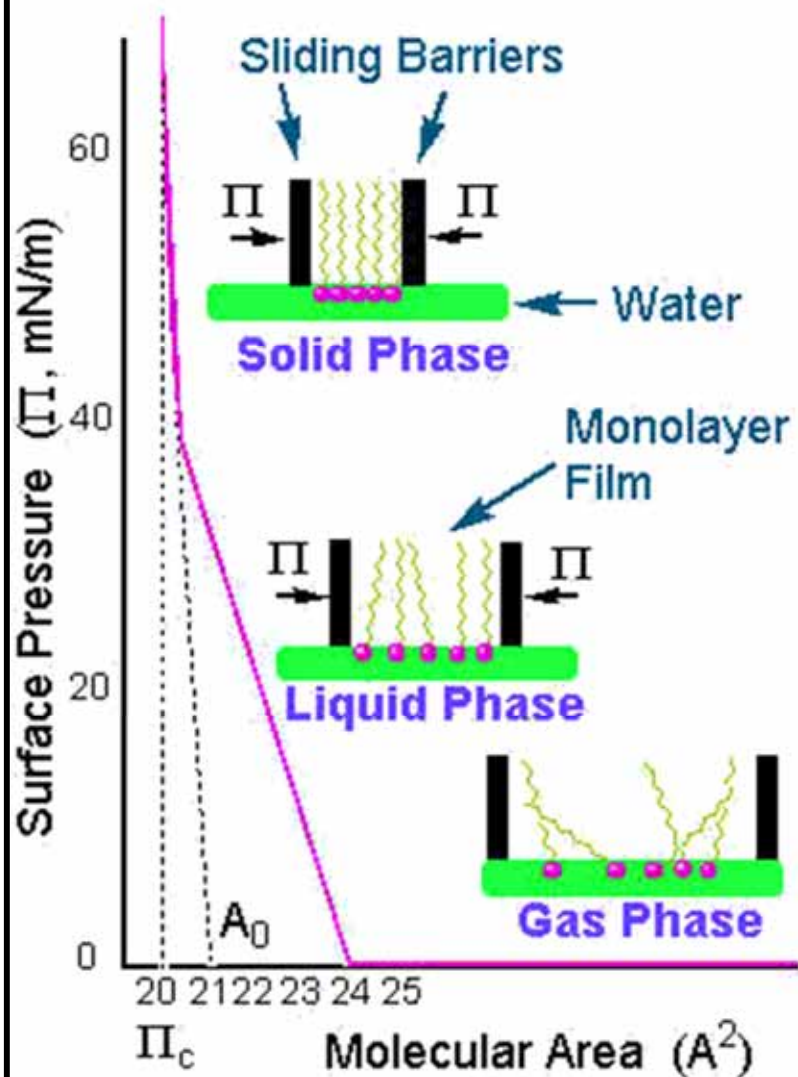
Langmuir-Blodgett Films



Langmuir-Blodgett Films



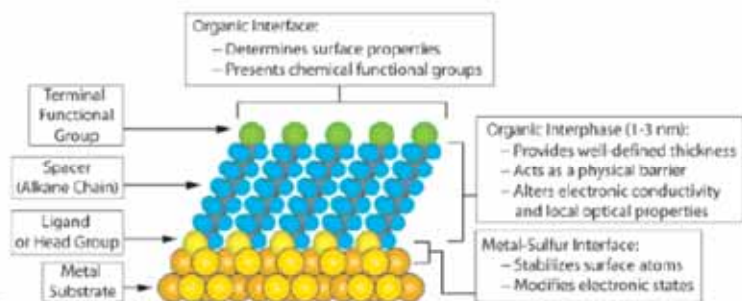
Isotherm



Self-Assemble Monolayer

(SAM)

Chem. Rev. 2005, 105, 1103–1169



S-Au 25-30 Kcal/mole
Si-O 190 kcal/mole

Morphology of Substrate				Morphology of Substrate			
Ligand	Substrates	Thin Films or Bulk Material	Nanoparticles or Other Nanostructures	Ligand	Substrates	Thin Films or Bulk Material	Nanoparticles or Other Nanostructures
ROH	Fe ₂ O ₃	36	35	RSSR'	Ag	89	90
	Si-H	37			Au	20	90-92
	Si				CdS		61
RCOO-/RCOOH	α -Al ₂ O ₃	38,39			Pd	30	
	Fe ₂ O ₃		40		Au	93	
	Ni		41,42				
RCOO-/OOCR	Ti/TiO ₂	43		RCSSH	Au	94	
	Si(111):H	44			CdSe		95
Ene-diol	Si(100):H			RS ₂ O ₂ Na ⁺	Au	96	
	Fe ₂ O ₃		45		Cu	97	
RNH ₂	FeS ₂	46		RSeH	Ag	99	
	Mica	47			Au	100,101	
	Stainless Steel 316L	48			CdS		60
	YBa ₂ Cu ₃ O _{7-δ}	49	50		CdSe		102
RCaN	CdSe			RSeSeR'	Au	101	
	Ag	51		R ₃ P	Au		103
R-N=N'(BF ₄)	Au				FeS ₂	46	
	GaAs(100)	52			CdS		104
	Pd	52			CdSe		104
RSH	Si(111):H	52			CdTe		104
	Ag	26	53,54	R ₃ P=O	Co		105,106
	Ag ₂ Ni ₁₀	55			CdS		104
	AgS		56		CdSe		104
	Au	26	57		CdTe		104
	AuAg		58	RPO ₃ ²⁻ /RPO(OH) ₂	Al	107	
	AuCu		58		Al-OH	108	
	Au ₂ Pd ₁₀		58		Ca ₁₀ (PO ₄) ₆ (OH) ₂	109	
	CdTe		59		GaAs	110	
	CdSe		60		GaN	110	
	CdS		61,62		Indium tin oxide	111	
	Cu	26	58		(ITO)		
	FePt		63-66		Mica	112	
	GaAs	67			TiO ₂	113,114	
	Ge	68			ZrO ₂	114,115	
	Hg	69-71			CdSe		116-118
	HgTe		72		CdTe		118,119
	InP	73		RPO ₃ ³⁻	Al ₂ O ₃	120	
	Ir		74		Nb ₂ O ₅	120	
	Ni	75			Ta ₂ O ₅	121	
	PbS		76-78		TiO ₂	120,122	
	Pd	30	74,79				
RSX ₃ X = H, Cl, OCH ₂ CH ₃	PdAg		58	RNaC	Pt	123	124
	Pt	32	80		Si	37	
	Ru		81		Si(111):H	125	
	Stainless Steel 316L	48		RSSX ₃ X = H, Cl, OCH ₂ CH ₃	HfO ₂	126	
	YBa ₂ Cu ₃ O _{7-δ}	82			ITO	127	
	Zn	83			PtO	128	
	ZnSe	84			TiO ₂	113,126,129	
	ZnS		85		ZrO ₂	126,129	
RSAc	Au	86					
	Au		87				
RSR'	Au	88					



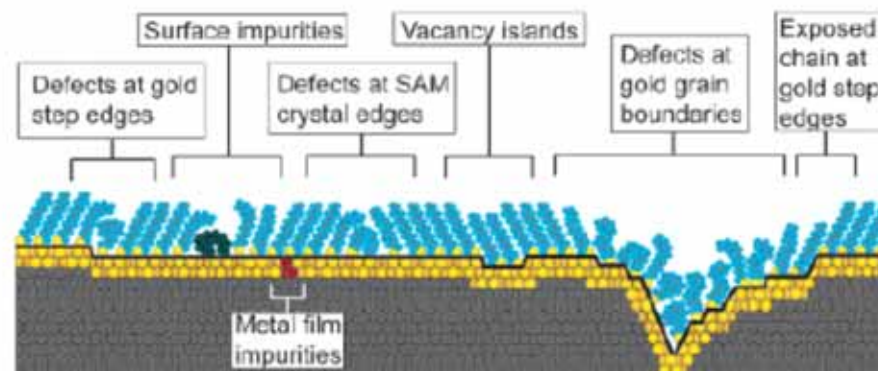
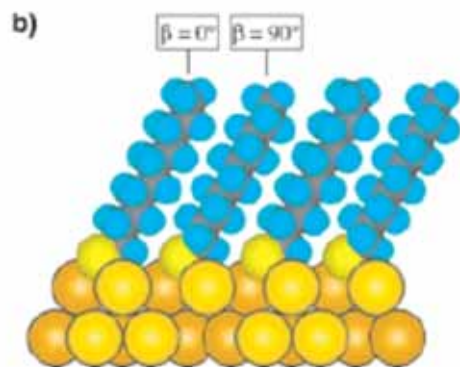
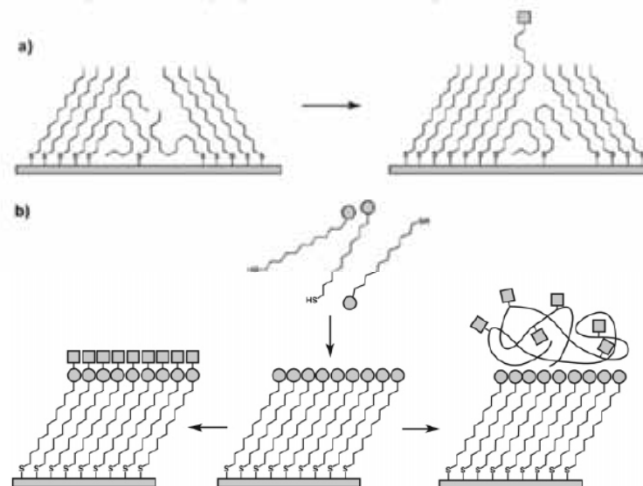
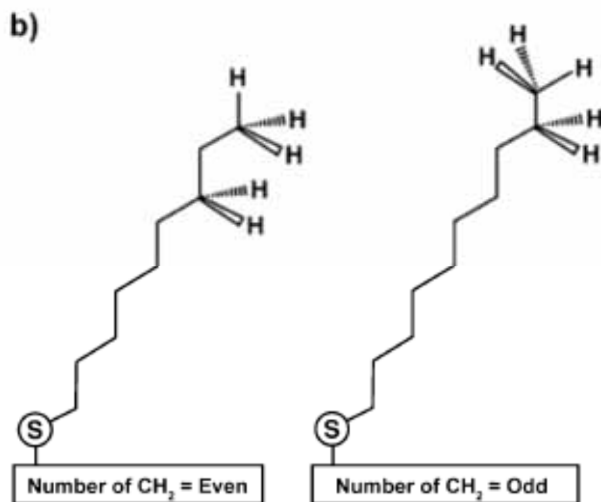


Figure 7. Schematic illustration of some of the intrinsic and extrinsic defects found in SAMs formed on polycrystalline substrates. The dark line at the metal–sulfur interface is a visual guide for the reader and indicates the changing topography of the substrate itself.



^a (a) Insertion of a functional adsorbate at a defect site in a preformed SAM. (b) Transformation of a SAM with exposed functional groups (circles) by either chemical reaction or adsorption of another material.



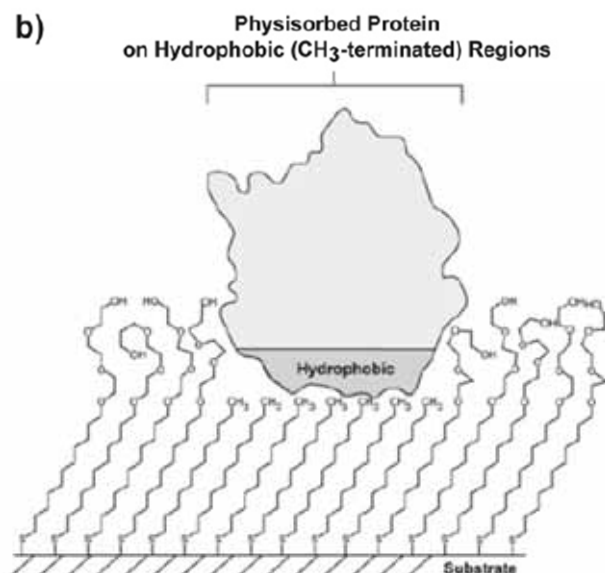
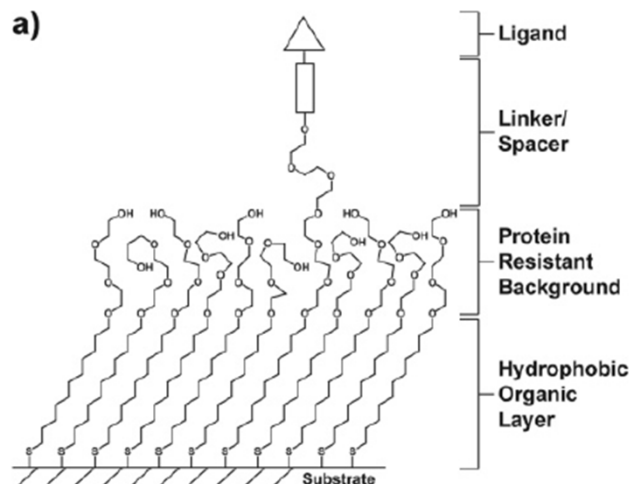


Figure 21. Schematic illustrations of (a) a mixed SAM and (b) a patterned SAM. Both types are used for applications in biology and biochemistry.

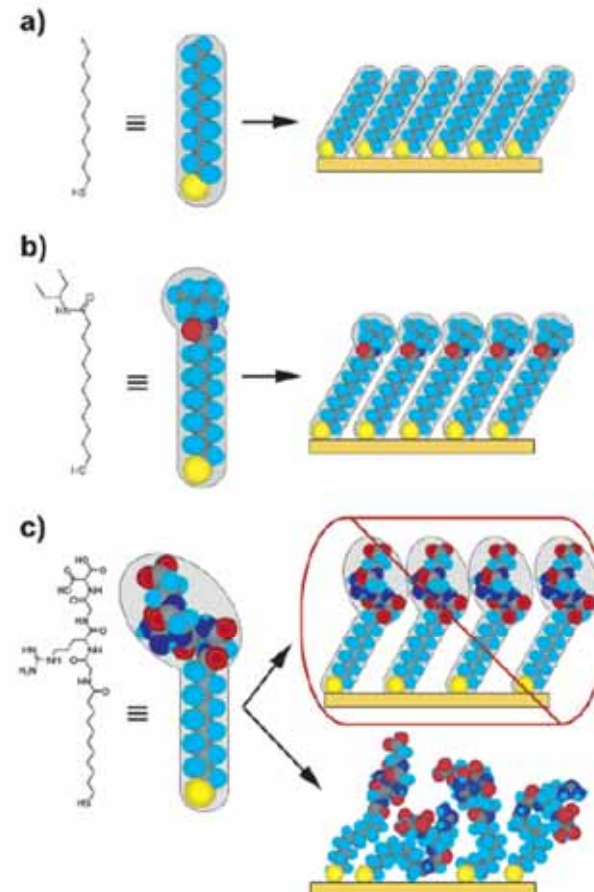


Figure 22. Schematic diagram illustrating the effects that large terminal groups have on the packing density and organization of SAMs. (a) Small terminal groups such as $-\text{CH}_3$, $-\text{CN}$, etc., do not distort the secondary organization of the organic layer and have no effect on the sulfur arrangement. (b) Slightly larger groups (like the branched amide shown here) begin to distort the organization of the organic layer, but the strongly favorable energetics of metal-sulfur binding drive a highly dense arrangement of adsorbates. (c) Large terminal groups (peptides, proteins, antibodies) sterically are unable to adopt a secondary organization similar to that for alkanethiols with small terminal groups. The resulting structures probably are more disordered and less dense than those formed with the types of molecules in a and b.



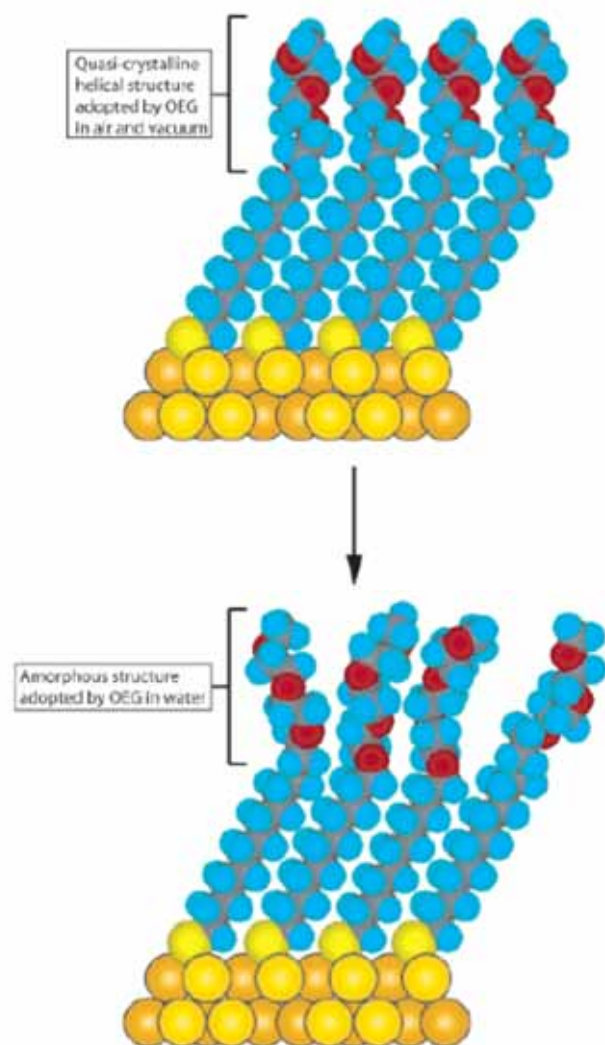
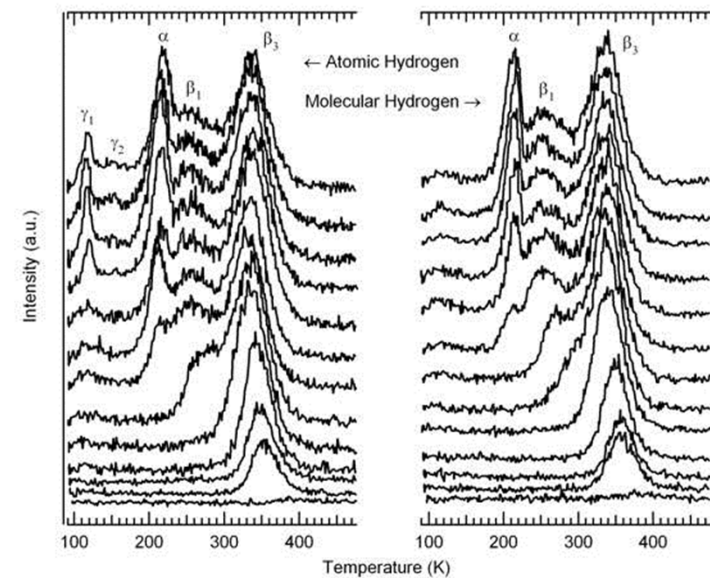


Figure 23. Schematic illustration of the order–disorder transition evidenced by SAMs of alkanethiolates terminated with triethylene glycol. The EG₃ group loses conformational ordering upon solvation in water.



Temperature Programmed Desorption



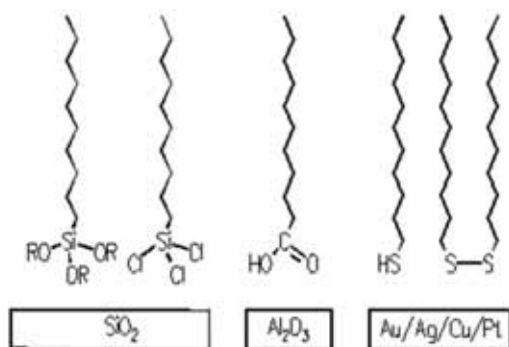
Self-Assembly

- Substrates
- Interstitial adhesion layer
- Noble metal layer
- Organo-sulfur



Organosilanes

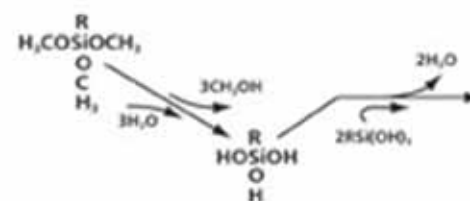
Self-assembled monolayers



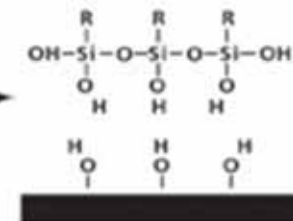
Immersion of substrate in a solution containing the adequate molecules for 12 - 24 hours yields an ordered monolayer

- Surface
- silicon oxide: silanisation
- aluminum oxide: fatty acids
- metals: thiols and sulfides

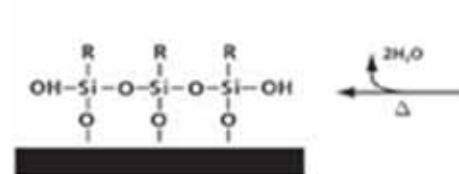
Hydrolysis (1)



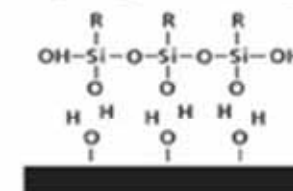
Condensation of Oligomers (2)



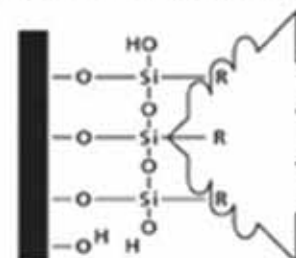
Bond Formation (4)



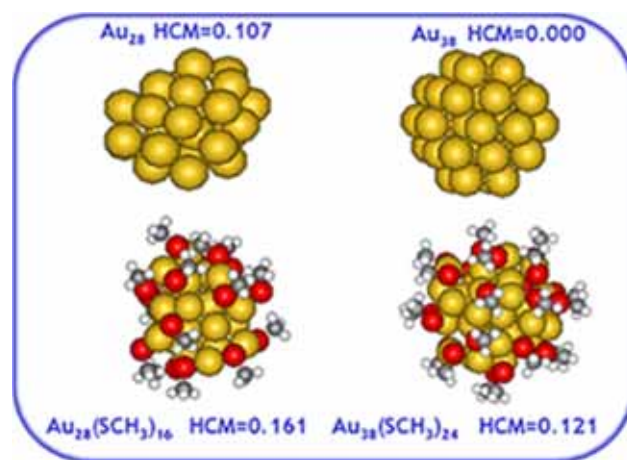
Hydrogen Bonding (3)



Reaction and bond formation of the R group (5)

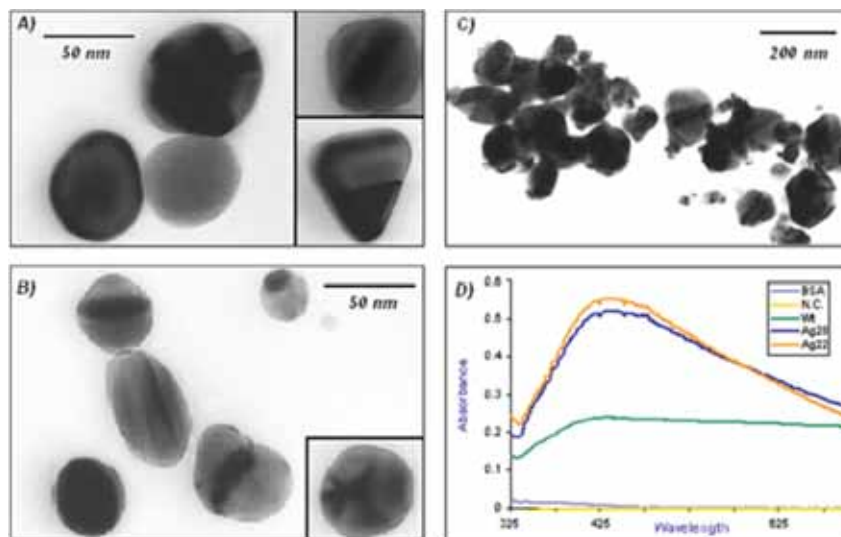
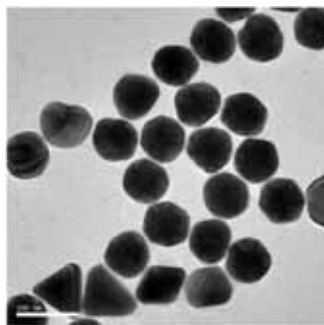
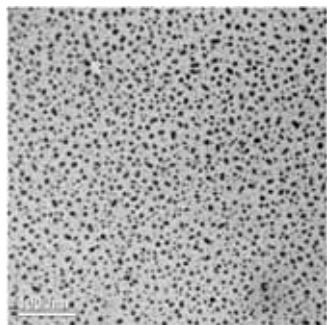
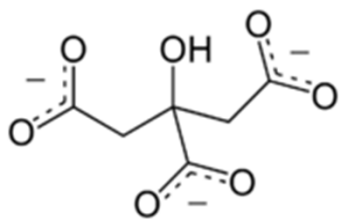


Metal Reduction



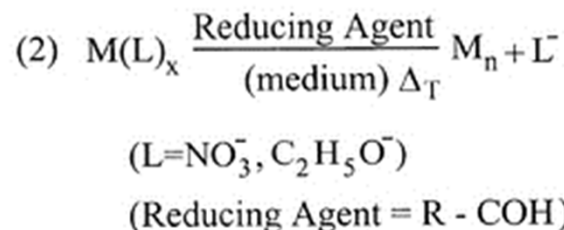
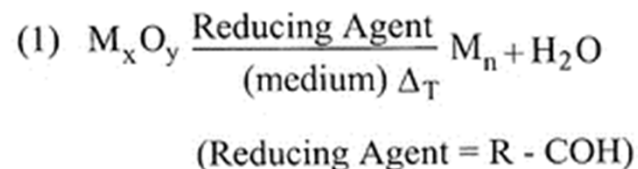
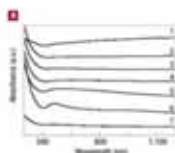
Synthesis of Silver Nanoparticles

1. ***A solution of AgNO_3 ($1.0 \times 10^{-3} \text{ M}$) in deionized water was heated until it began to boil.***
2. ***Sodium citrate solution was added dropwise to the silver nitrate solution as soon as the boiling commenced. The color of the solution slowly turned into grayish yellow, indicating the reduction of the Ag^+ ions.***
3. ***Heating was continued for an additional 15 min, and then the solution was cooled to room temperature before employing for further experimentation.***



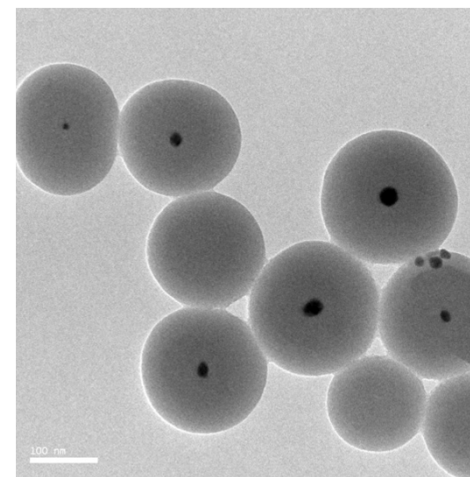
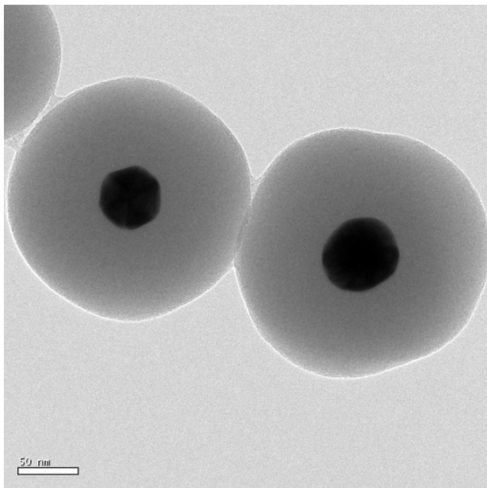
Synthesis of Gold Nanoparticles

1. Add 20 mL of 1.0 mM HAuCl_4 to a 50 mL round bottom flask on a stirring hot plate.
2. Add a magnetic stir bar and bring the solution to a boil.
3. To the boiling solution, add 2 mL of a 1% solution of trisodium citrate dihydrate
4. The gold sol gradually forms as the citrate reduces the gold(III). Stop heating when a deep red color is obtained.

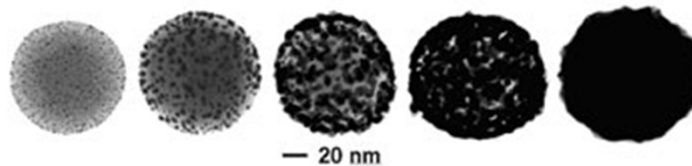
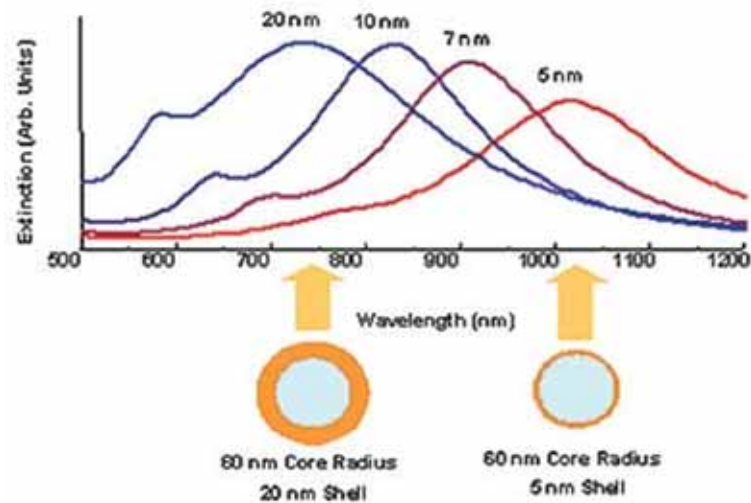


Construction of Core Shell Ag/Au@SiO₂ Nanoparticles

1. Under vigorous stirring, 1 ml of the silver/ gold colloids solution was mixed with 250 mL of isopropanol and 25 mL of deionized water.
2. Immediately after the addition of 4 mL of 30% ammonium hydroxide, different amounts of tetraethoxysilane (TEOS) were added to the reaction mixture.
3. To obtain different silica layer thicknesses, TEOS solutions with a concentration between 50% and 100% was added to the suspension. The reaction was stirred at room temperature for 30 minutes and then was allowed to age without agitation at 4°C overnight.
4. Each suspension of silica-coated silver/gold nanoparticles was washed and centrifuged, followed by re-suspension in water. The thickness of the silica layers was determined from TEM images .



Core-Shell Nanoparticles



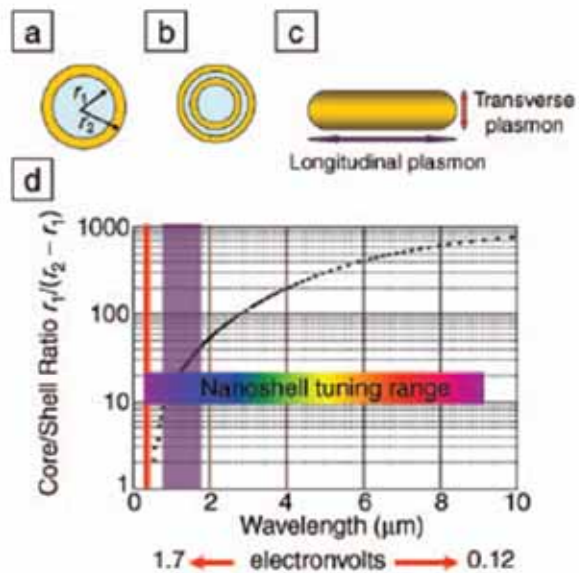


Figure 1. (a) Schematic illustration of a silica-core, gold-shell nanoshell, indicating inner (r_1) and outer (r_2) radii of the shell layers. (b) Depiction of a four-layer, concentric nanoshell. (c) Schematic illustration of a metallic nanorod. (d) Plot of nanoshell resonance as a function of core and shell dimensions, overlaid with reported spectral ranges of nanorod resonances (red, transverse plasmon; purple, longitudinal plasmon), and reported nanoshell and concentric nanoshell combined spectral range of plasmon response.

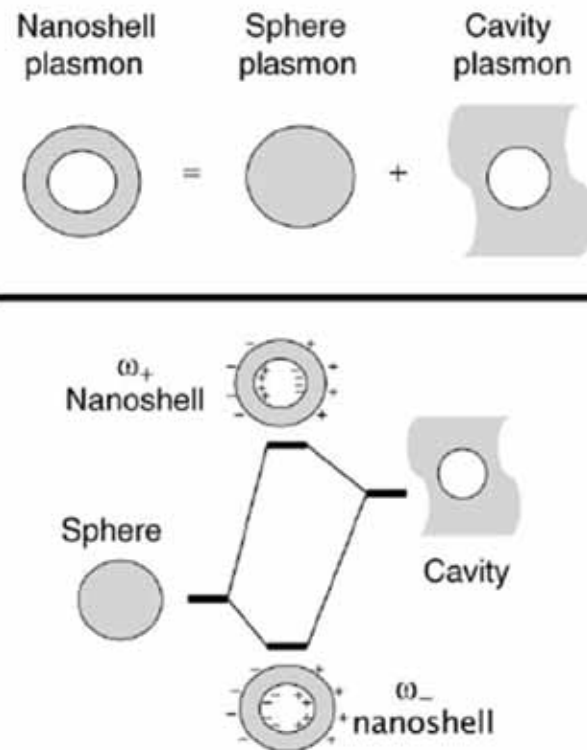
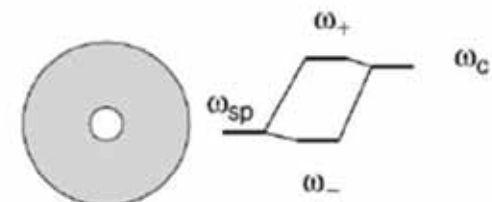
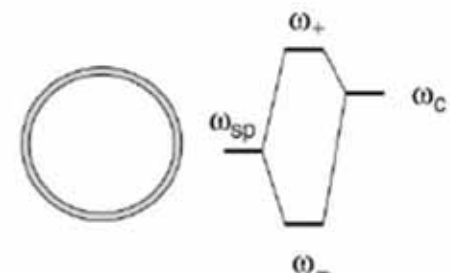


Figure 2. Plasmon hybridization and the sphere-cavity model for nanoshells: the interaction between a sphere (resonance frequency, ω_{sp}) and a cavity plasmon (resonance frequency, ω_c) is tuned by varying the thickness of the shell layer of the nanoparticle. Two hybrid plasmon resonances, the ω_- "bright," or "bonding," plasmon and the ω_+ "dark," or "anti-bonding," plasmon resonances are formed. The lower-energy plasmon couples most strongly to the optical field.

Thick shell, weak interaction:



Thin shell, strong interaction:



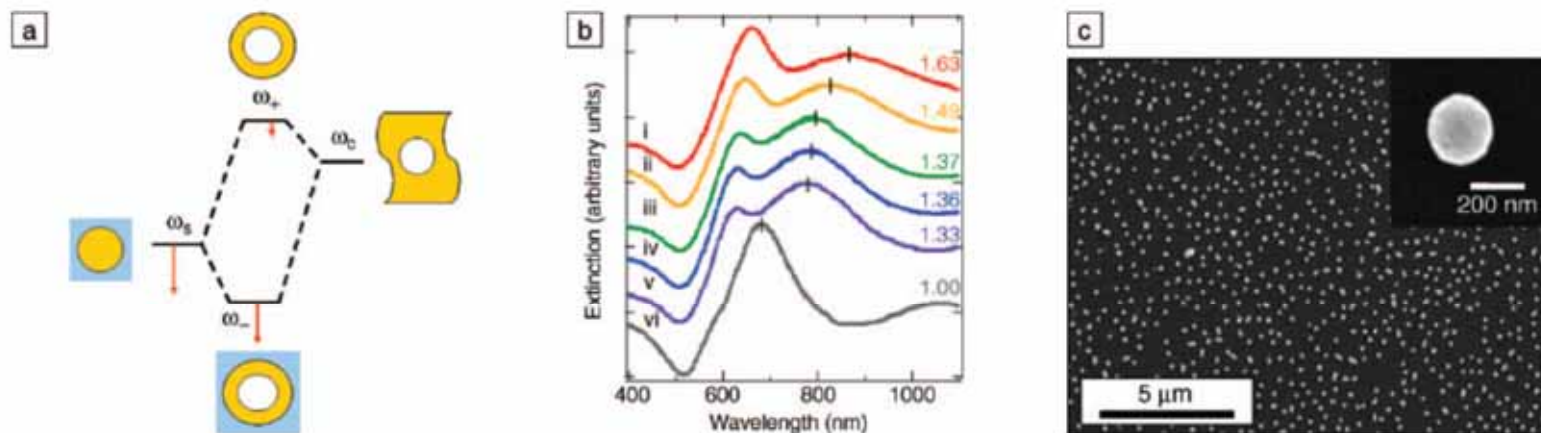


Figure 5. (a) Plasmon hybridization picture applied to surface plasmon resonance sensing with nanoshells: the low-energy “bonding” plasmon, ω_- , is sensitized to changes in its dielectric environment. The blue background schematically denotes the embedding medium for the nanoparticle. (b) Experimental curves showing plasmon resonance shifts for nanoshell-coated films in various media: (i) carbon disulfide, (ii) toluene, (iii) hexane, (iv) ethanol, (v) H_2O , and (vi) air. The index of refraction for each embedding medium is noted on the far right of the spectra. Spectra are offset for clarity. (c) Scanning electron micrograph of nanoshells deposited onto a poly(vinyl pyridine) functionalized glass surface, as used to acquire data in (b). Inset: individual nanoshell.



Preparation of $\text{Fe}_3\text{O}_4@\text{Ag}/\text{Au}$

1. *To the magnetic nanoparticle suspension obtained from commercial company, add 50 ml of a solution of Au (III) salt or Ag (I) salt at concentration of 0.01–1% mmol/L , shaking for 30 minutes, allowing Au (III) or Ag (I) ion to absorb on the surface of magnetic nanoparticle sufficiently,*
2. *Then adding 15–40 ml of reducing agent, such as hydroxylamine hydrochloride at concentration of 40 mmol/L, reacting for 5–40 minutes.*
3. *Further adding 1–10 ml of a solution of Au (III) salt or Ag (I) salt at concentration of 0.01–1%, shaking for 10 minutes, coating a reduced layer of gold or silver on the surface of the magnetic nanoparticle, forming super-paramagnetic composite particles having core/shell structure, separating magnetically, washing repeatedly with distilled water.*



Synthesis of Quantum Dots

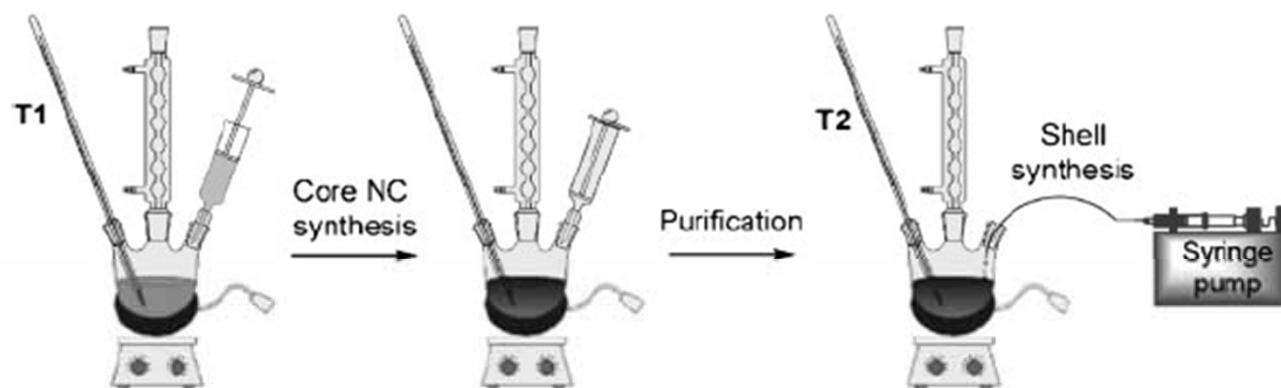
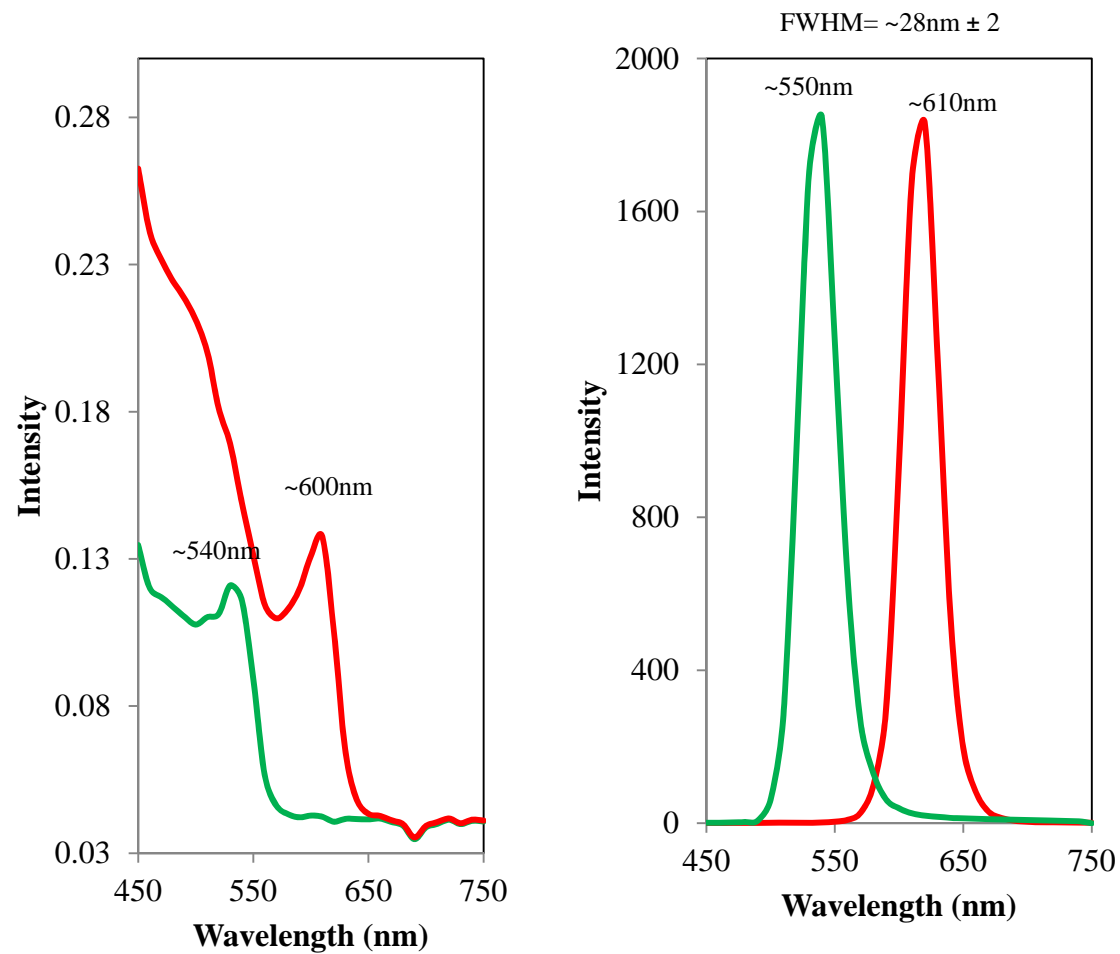


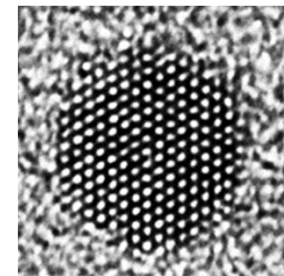
Figure 2. Two-step synthesis of core/shell nanocrystals.



Synthesis of CdSe Quantum dots



Cooperative UV and PL spectra of CdSe core

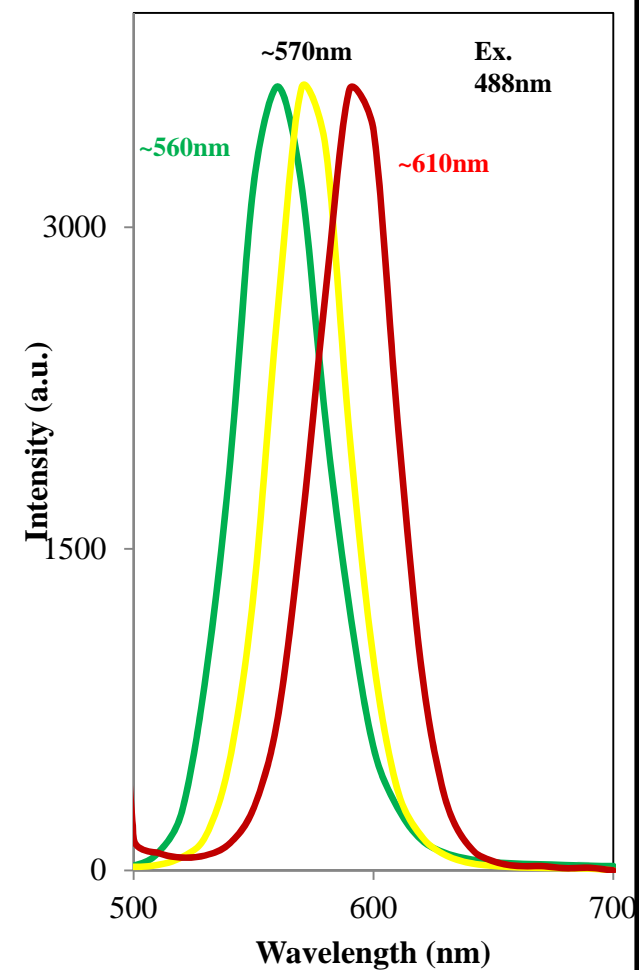
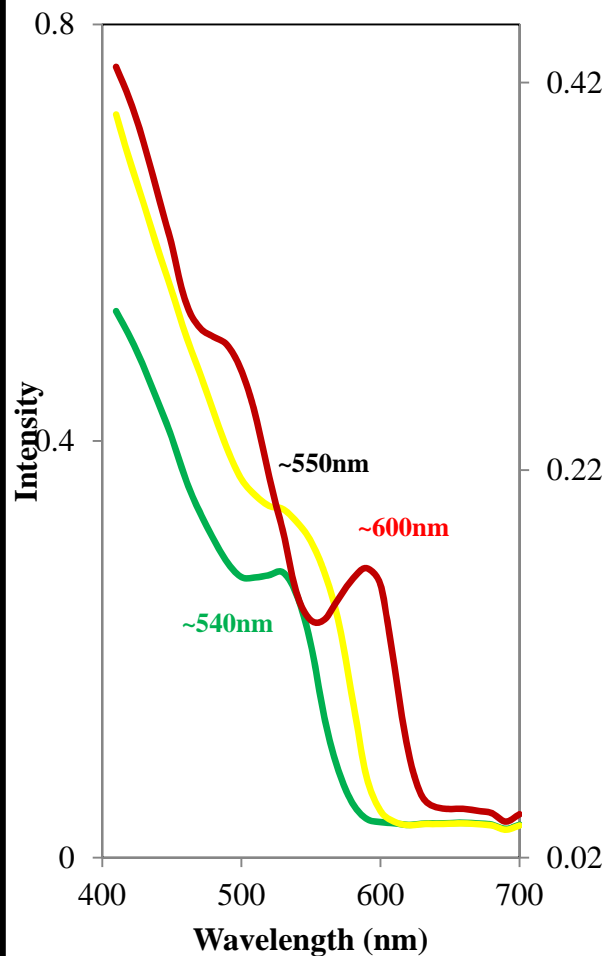
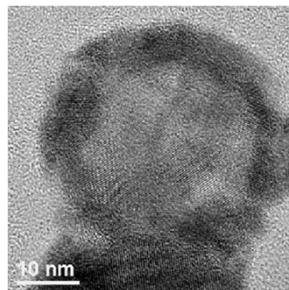


Synthesis of CdSe/ZnS Quantum Dots

20mL (31mg, 0.16 mmol) colloidal solution of CdSe QDs from stock solution (54mg dissolved in 35mL toluene) was placed in a two-neck flask. TOPO (6g) and HAD (6g) were added and then toluene was removed through vacuum, flask refilled with nitrogen. The reaction mixture was heated at 350 °C for two hours. In another flask zinc acetate in 1:3 ratio with respect of CdSe and was dissolved in 4mL of oleic acid stirred at 120 °C for 2 hours obtained a light yellow coloured solution and temperature reduced to 60-70 °C. After cooling to room temperature, TOPSe was mixed with Zn salt solution. And the mixture was injected slowly through syringe in to reaction solution of CdSe-TOPO at 180-200 °C. The stirring was done for another an hour. The similar procedure was followed for work up of reaction as avobe experiment. The final product was re-dispersed in toluene.



Light emission from CdSe/ZnSe Quantum dots



UV-Visible and PL spectra of CdSe/ZnSe re-dispersed in toluene



Nanorods

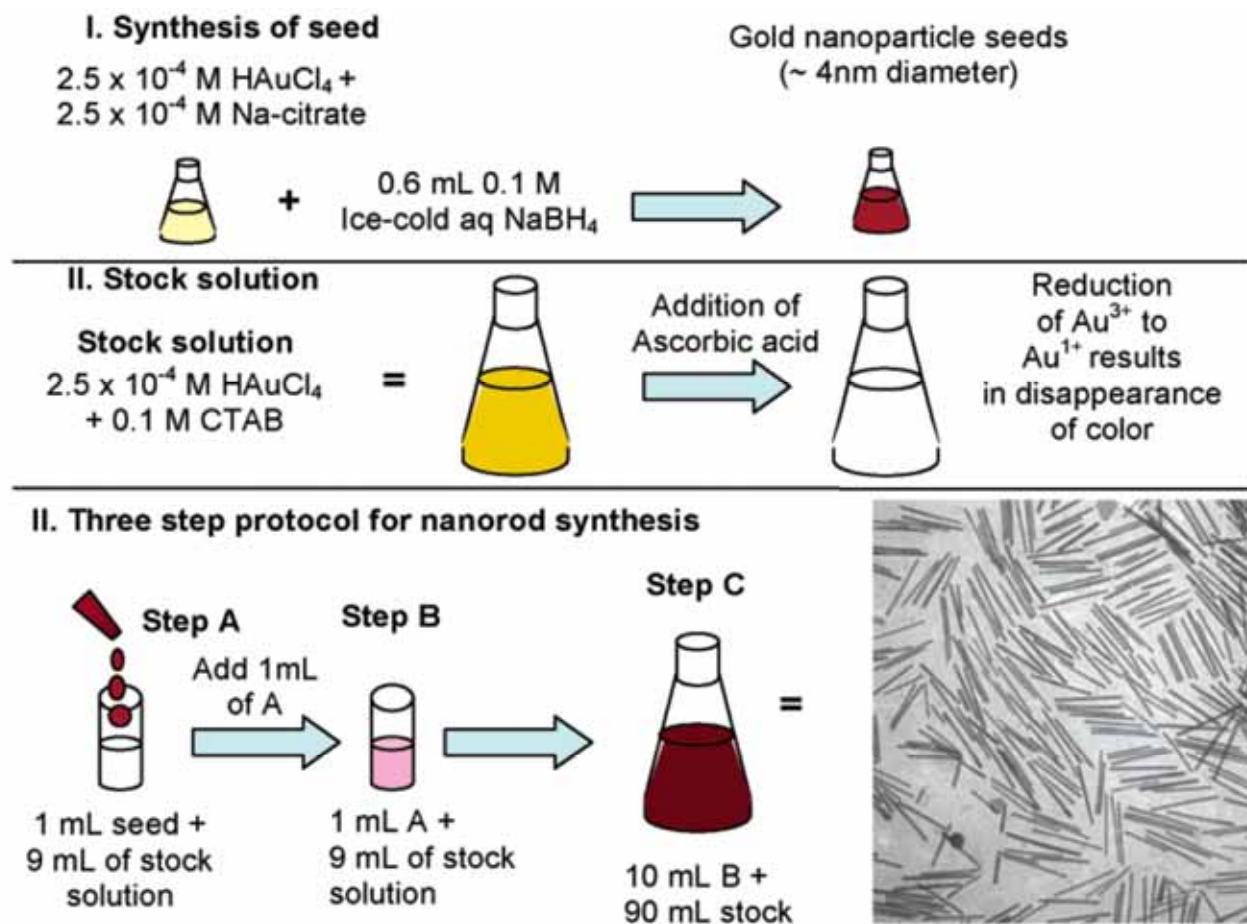
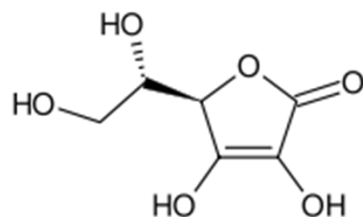
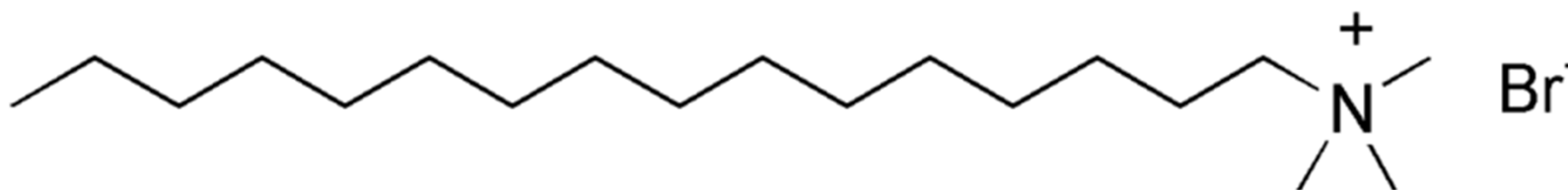


Figure 2. Seed-mediated growth approach to making gold and silver nanorods of controlled aspect ratio. The specific conditions shown here, for 20 mL volume of seed solution, lead to high-aspect ratio gold nanorods. (bottom right) Transmission electron micrograph of gold nanorods that are an average of 500 nm long.

Directional Growth

Cetrimonium bromide ((C₁₆H₃₃)N(CH₃)₃Br) (CTAB)



Ascorbic acid

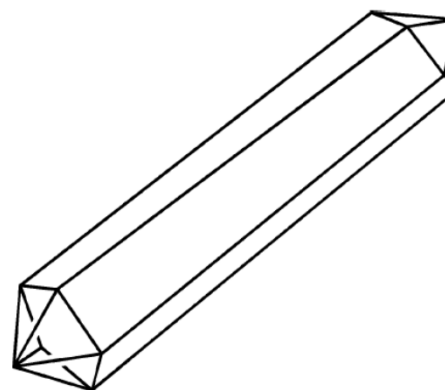


Figure 5. Cartoon of the crystallography of gold nanorods. The direction of elongation is [110]. The cross-sectional view is a pentagon; each end of the rod is capped with five triangular faces that are Au{111}. The sides of the rods are not as well-defined; either Au{100} or Au{110} faces, or both.



STEP 1: SYMMETRY BREAKING IN FCC METALS



STEP 2: PREFERENTIAL SURFACTANT BINDING TO SPECIFIC CRYSTAL FACES

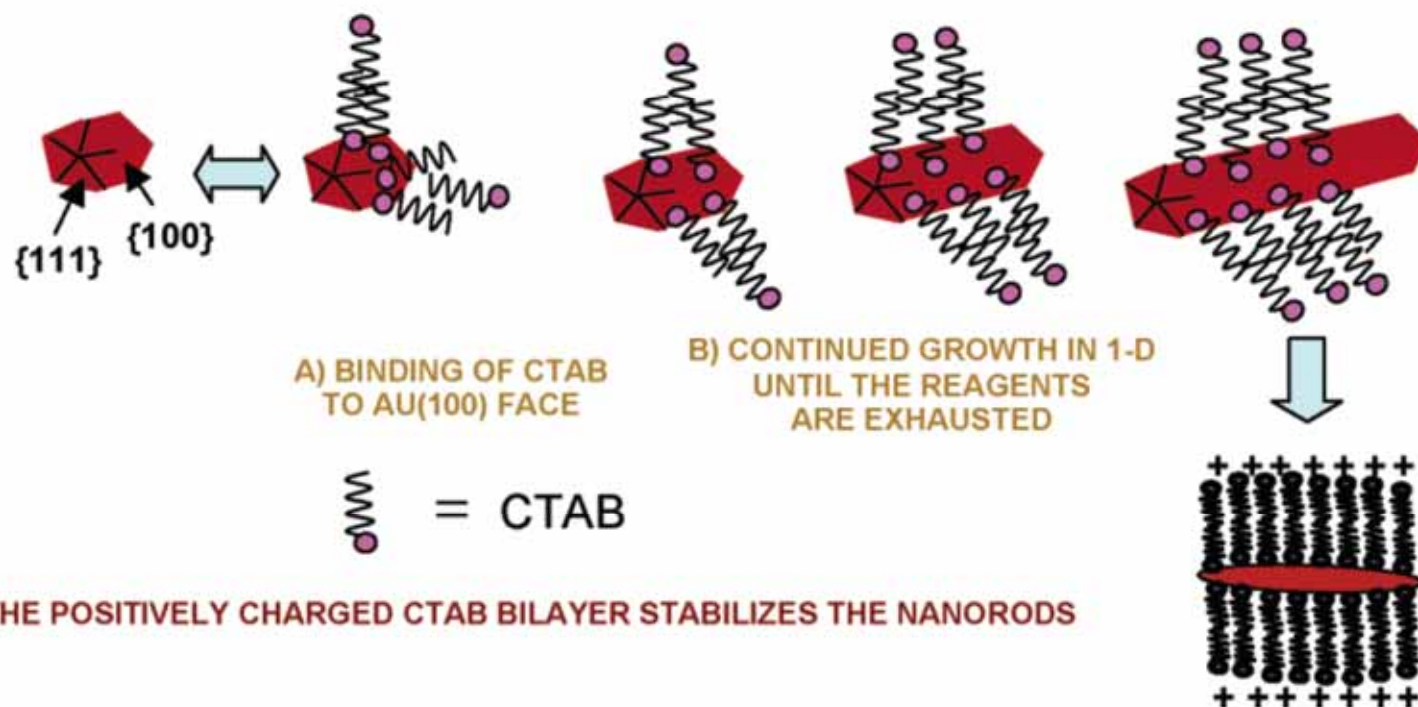


Figure 8. Proposed mechanism of surfactant-directed metal nanorod growth. The single crystalline seed particles have facets that are differentially blocked by surfactant (or an initial halide layer that then electrostatically attracts the cationic surfactant). Subsequent addition of metal ions and weak reducing agent lead to metallic growth at the exposed particle faces. In this example, the pentatetrahedral twin formation leads to Au {111} faces that are on the ends of the nanorods, leaving less stable faces of gold as the side faces, which are bound by the surfactant bilayer.



Nanorods

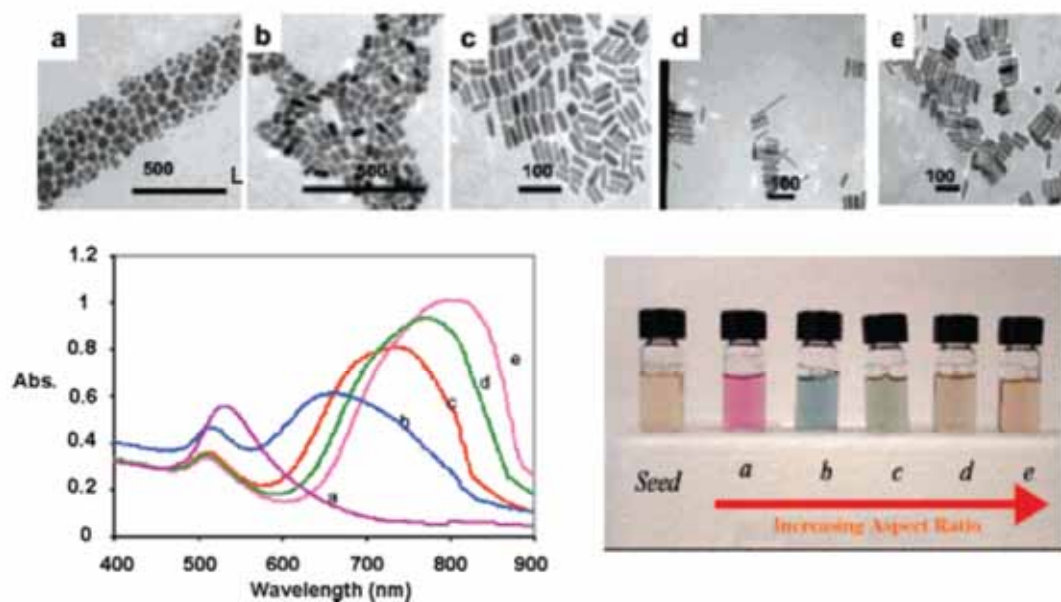
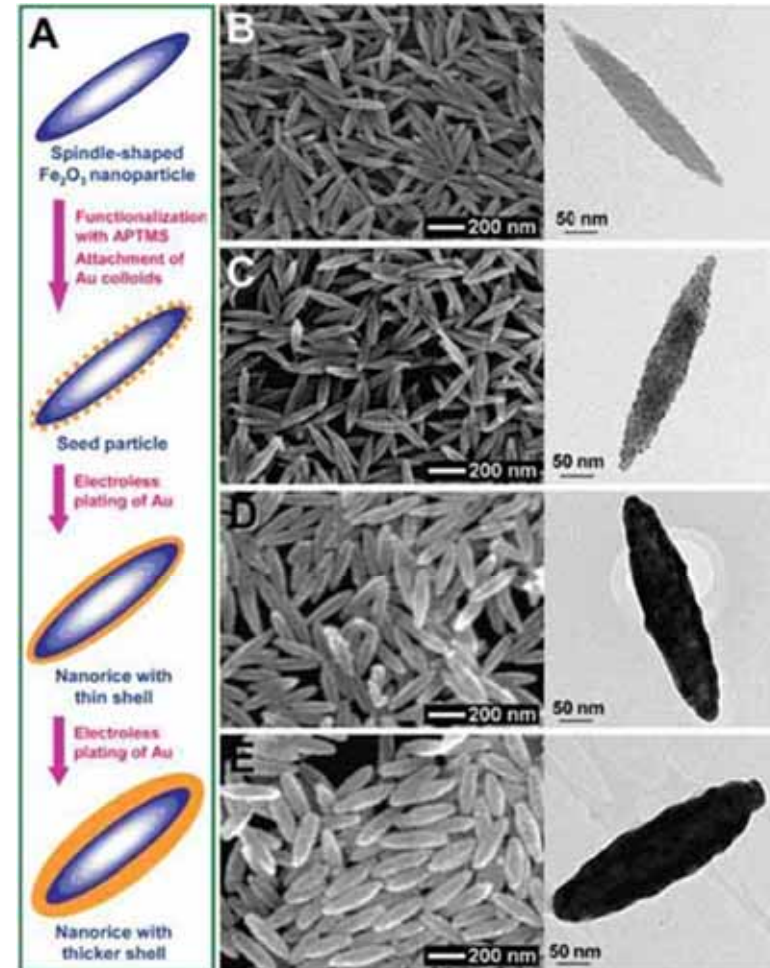
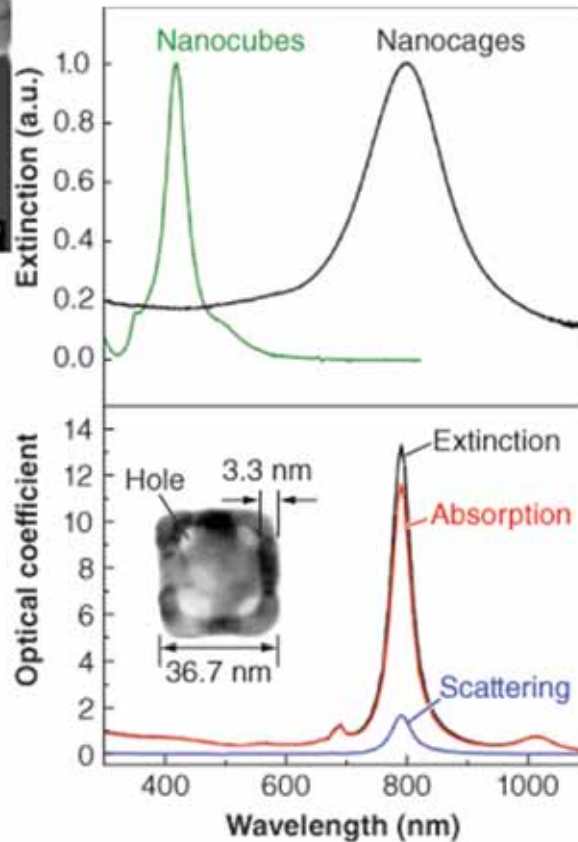
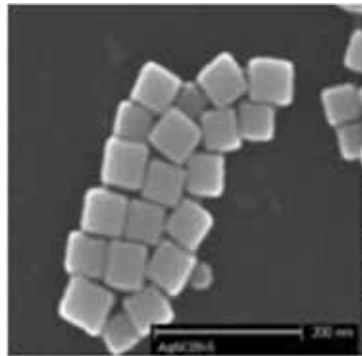


Figure 3. Transmission electron micrographs (top), optical spectra (left), and photographs (right) of aqueous solutions of Au nanorods of various aspect ratios. The seed sample has an aspect ratio of 1. Samples a, b, c, d, and e have aspect ratios of 1.35 ± 0.32 , 1.95 ± 0.34 , 3.06 ± 0.28 , 3.50 ± 0.29 , and 4.42 ± 0.23 , respectively. Scale bars: 500 nm for a and b, 100 nm for c–e. Reprinted with permission from ref 16. Copyright 2005 American Chemical Society.



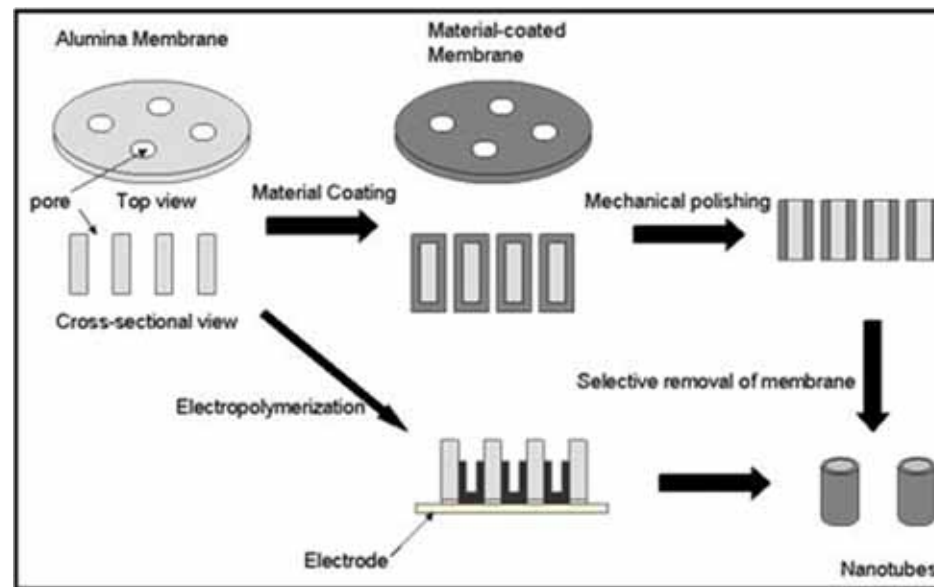
Nanocube and Nanorice



The graphic above depicts various magnitudes of nanorice, which is a rice-shaped nanoparticle with a non-conducting core made of iron oxide and covered by a metallic shell made of gold. Scientists plan to attach the nanorice to scanning probe microscopes to obtain very clear image quality that surpasses today's technology. For the Air Force, this technology could be used as a tool to develop new high-speed optoelectronic materials and to monitor chemical reactions. (Graphic provided by Prof. Naomi Halas)



Template Synthesis

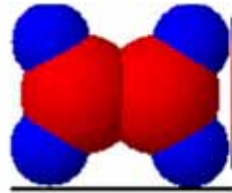


Porous Materials

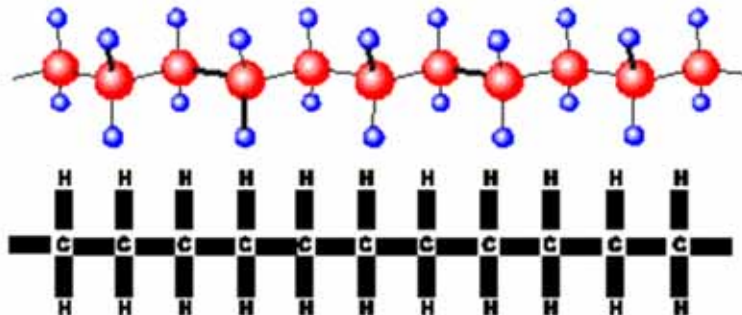
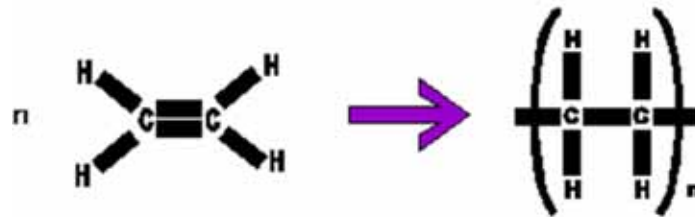
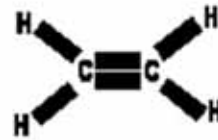
- AAO
- MCM-41
- Micro-
- Meso
- Macro-



Polymer



a monomer ethene

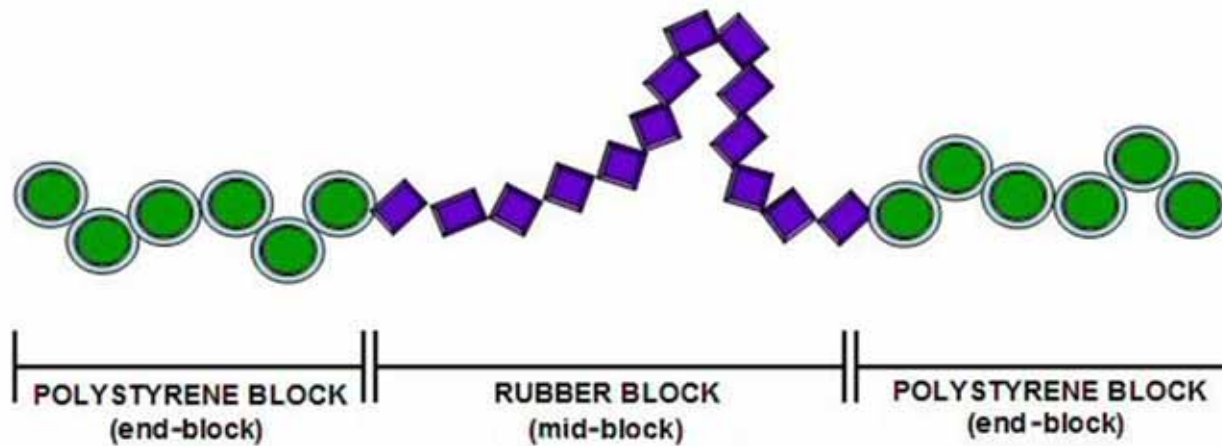


a polymer

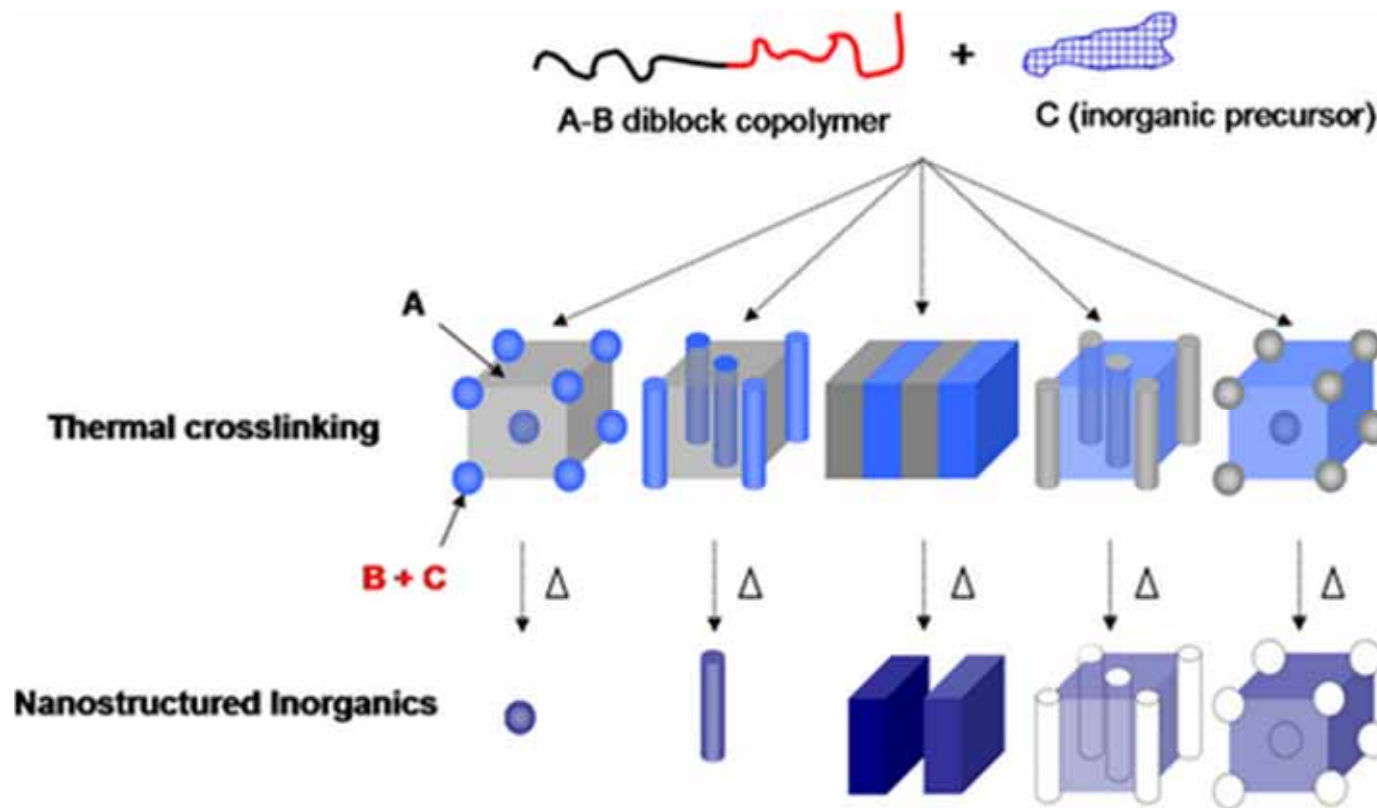
poly(ethene)



Block copolymer



Phase Segregation

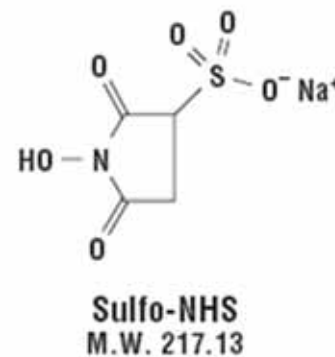
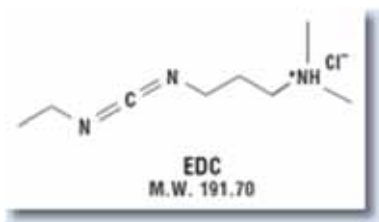
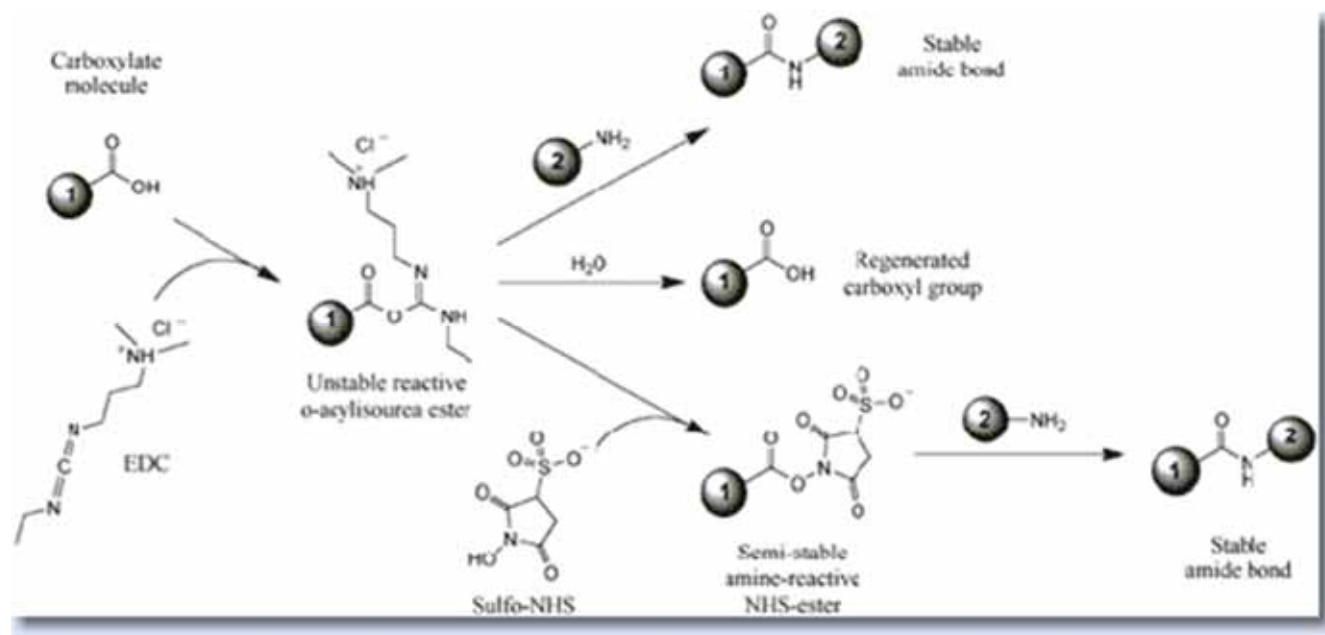


Surface Functionalization

- Recognition
 - Molecular Recognition
 - Protein
 - DNA
 - Saccharide
- Reporting/Detection
 - Dye
 - Quantum dots
 - SPR
 - SERS/LSPR
- Separation
 - Gel/Chromatography
 - Magnetic
- Surfaces
 - Gold and silver
 - Silicon oxide (glass)
 - Quantum dots
 - Polymer

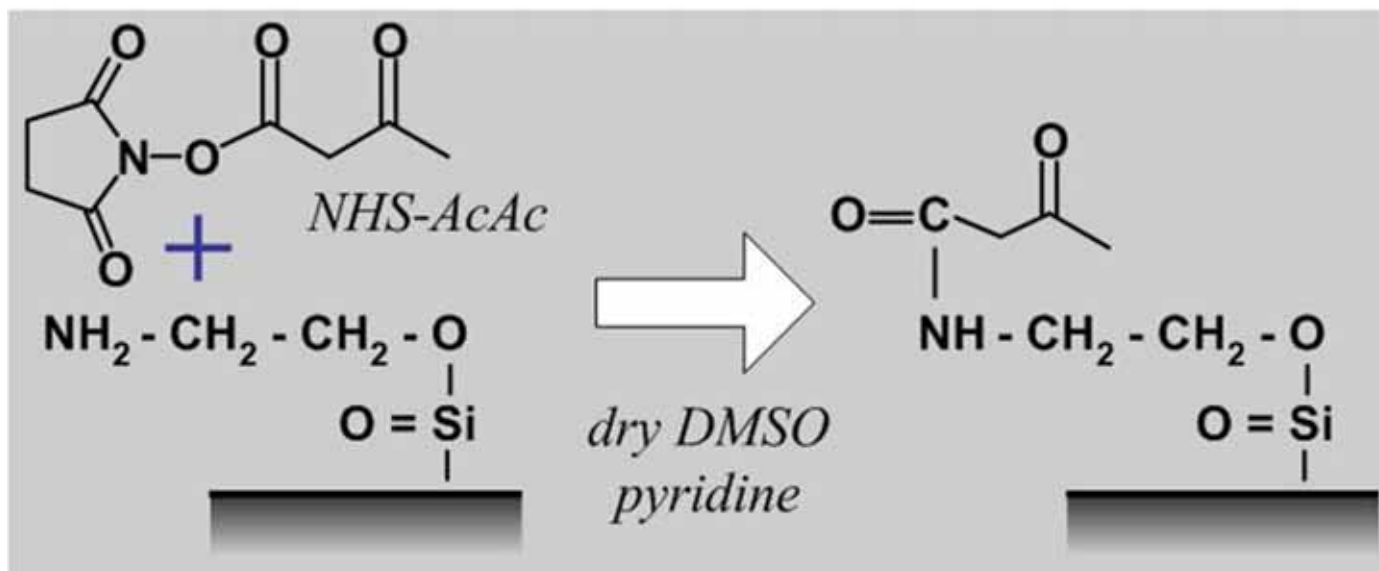


Carboxyl Presenting Surfaces

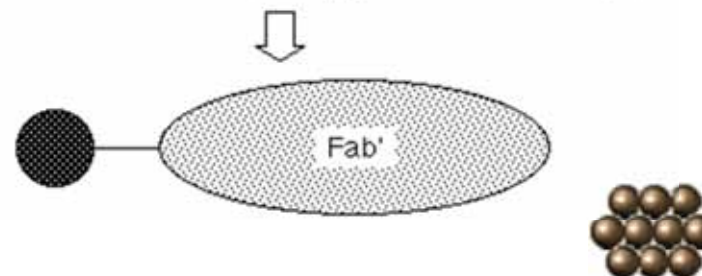
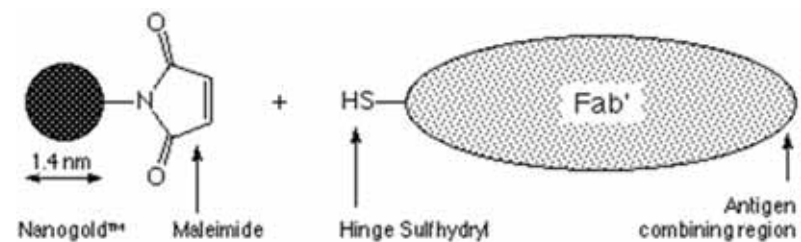
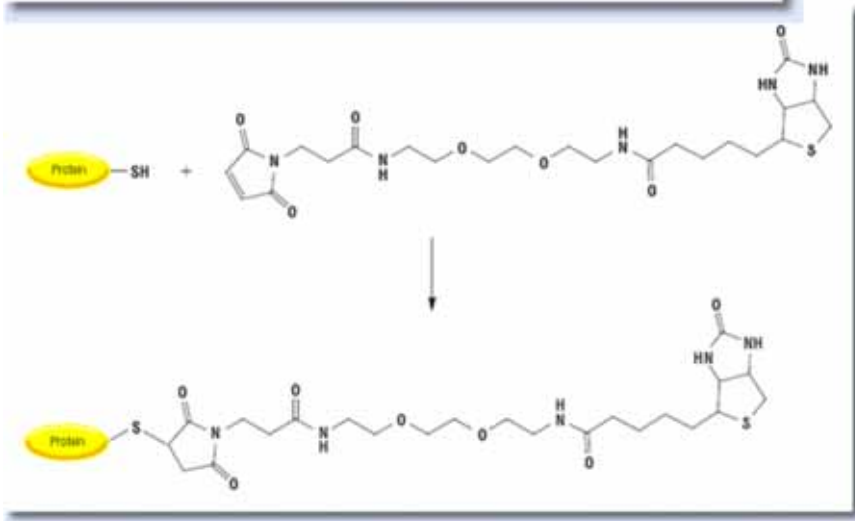
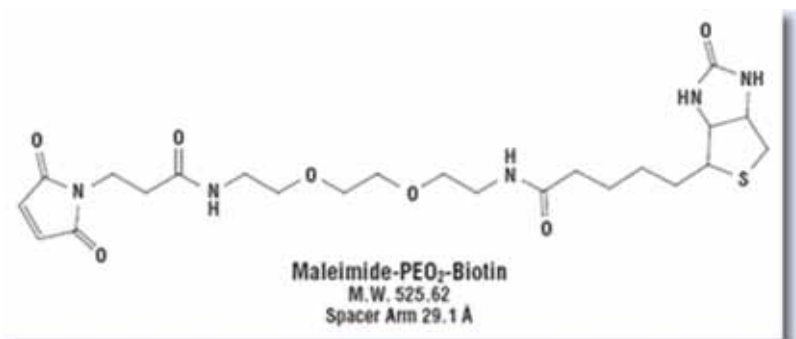
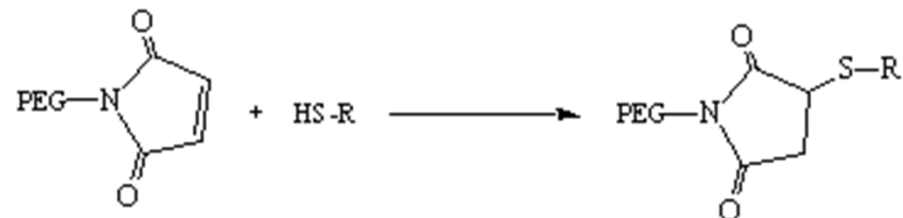


EDC (1-Ethyl-3-[3-dimethylaminopropyl]carbodiimide Hydrochloride)

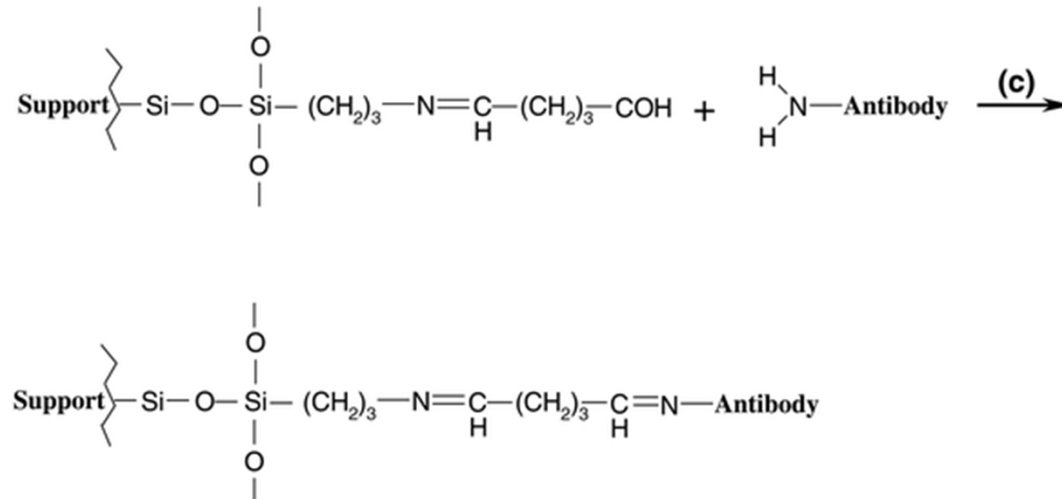
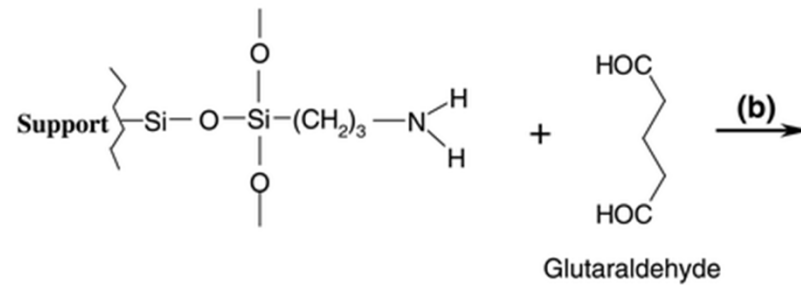
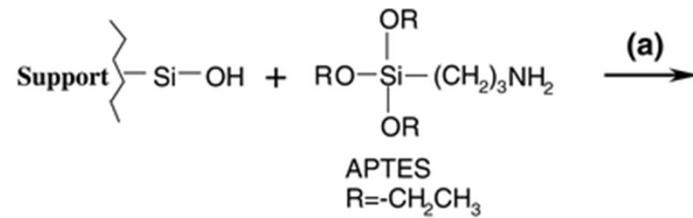
Amine Presenting Surface



Sulfhydryl Labeling



Silica Modification



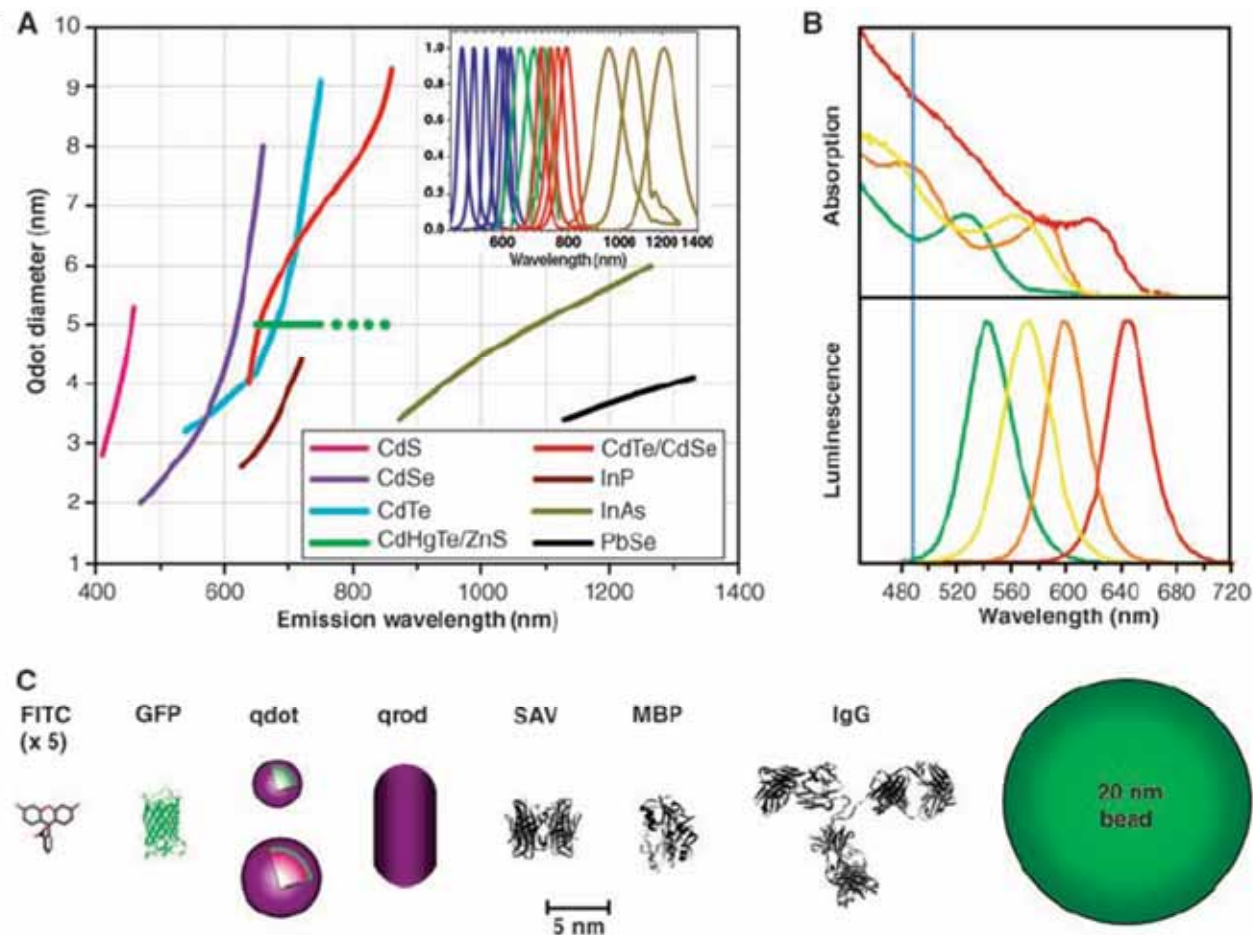
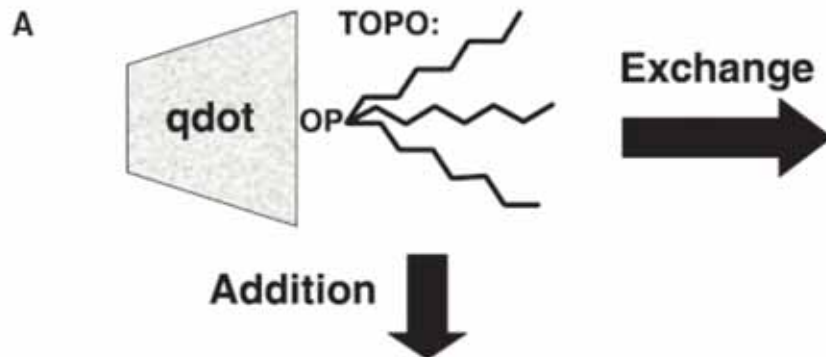
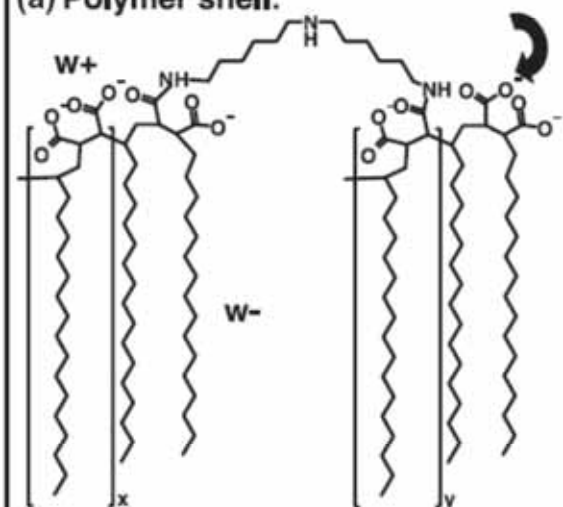


Fig. 1. (A) Emission maxima and sizes of quantum dots of different composition. Quantum dots can be synthesized from various types of semiconductor materials (II-VI: CdS, CdSe, CdTe...; III-V: InP, InAs...; IV-VI: PbSe...) characterized by different bulk band gap energies. The curves represent experimental data from the literature on the dependence of peak emission wavelength on qdot diameter. The range of emission wavelength is 400 to 1350 nm, with size varying from 2 to 9.5 nm (organic passivation/solubilization layer not included). All spectra are typically around 30 to 50 nm (full width at half maximum). Inset: Representative emission spectra for some materials. Data are from (12, 18, 27, 76–82). Data for CdHgTe/ZnS have been extrapolated to the maximum emission wavelength obtained in our group. (B) Absorption (upper curves) and emission (lower curves) spectra of four CdSe/ZnS qdot samples. The blue vertical line indicates the 488-nm line of an argon-ion laser, which can be used to efficiently excite all four types of qdots simultaneously. [Adapted from (28)] (C) Size comparison of qdots and comparable objects. FITC, fluorescein isothiocyanate; GFP, green fluorescent protein; qdot, green (4 nm, top) and red (6.5 nm, bottom) CdSe/ZnS qdot; qrod, rod-shaped qdot (size from Quantum Dot Corp.'s Web site). Three proteins—streptavidin (SAV), maltose binding protein (MBP), and immunoglobulin G (IgG)—have been used for further functionalization of qdots (see text) and add to the final size of the qdot, in conjunction with the solubilization chemistry (Fig. 2).

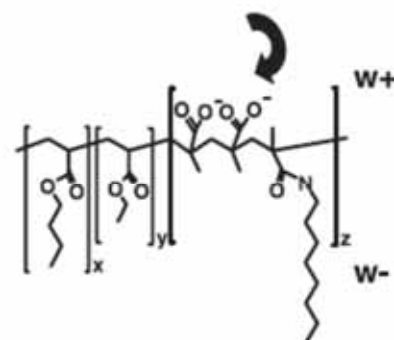




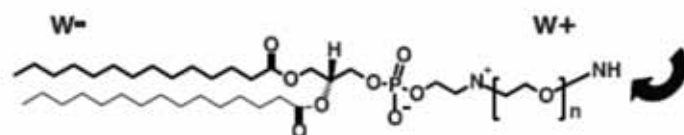
(a) Polymer shell:





(b) Triblock copolymer:




(c) Phospholipids:

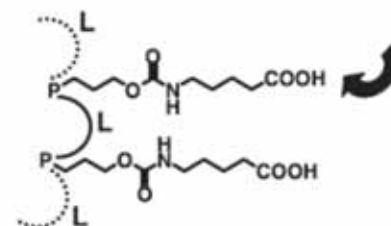


(d) MAA: 

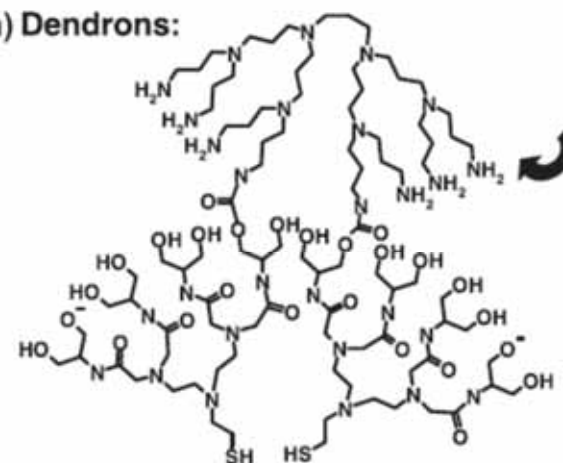
(e) DTT: 

(f) DHLA: 

(g) Oligomeric phosphine:

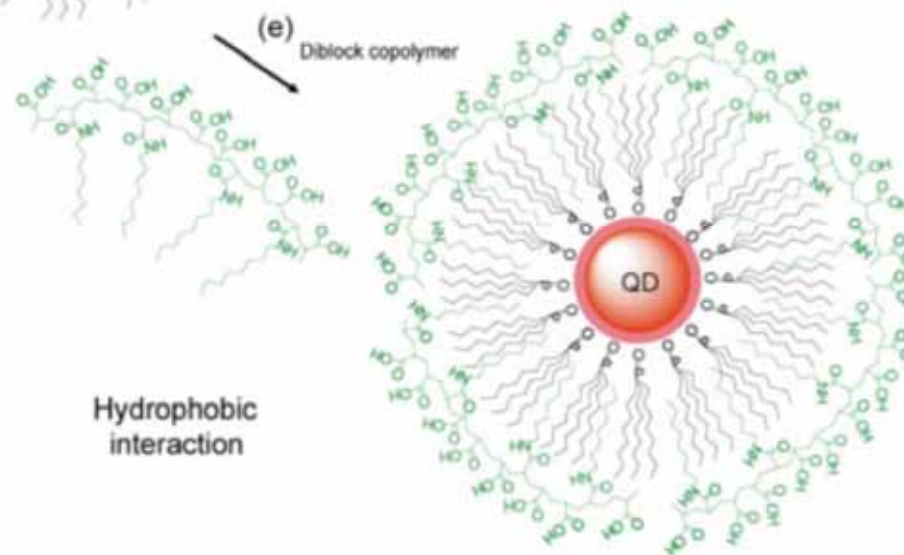
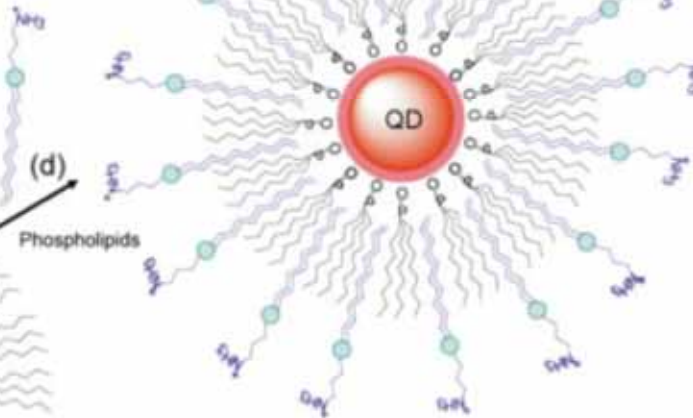
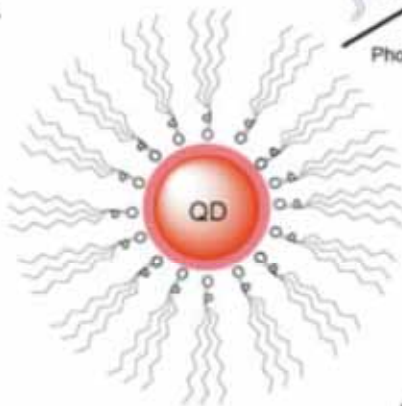
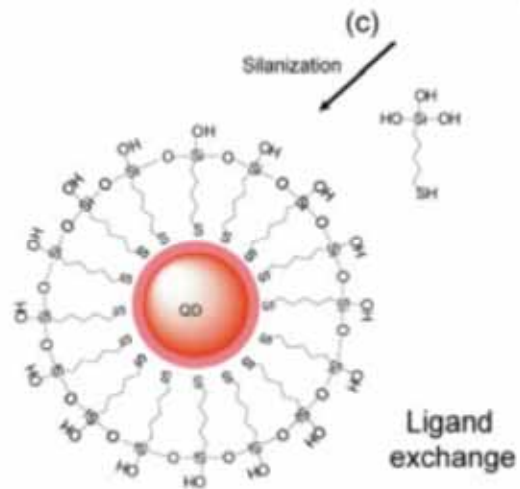
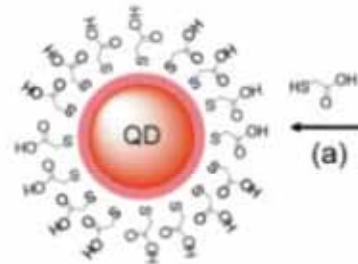
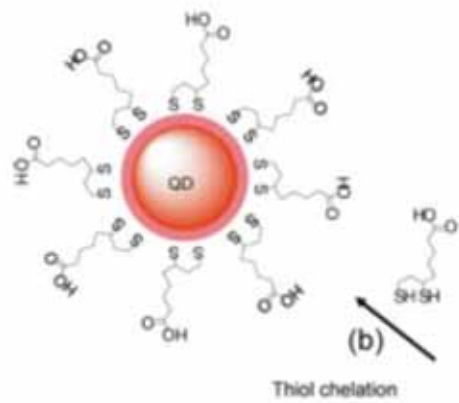


(h) Dendrons:



(i) Peptides:





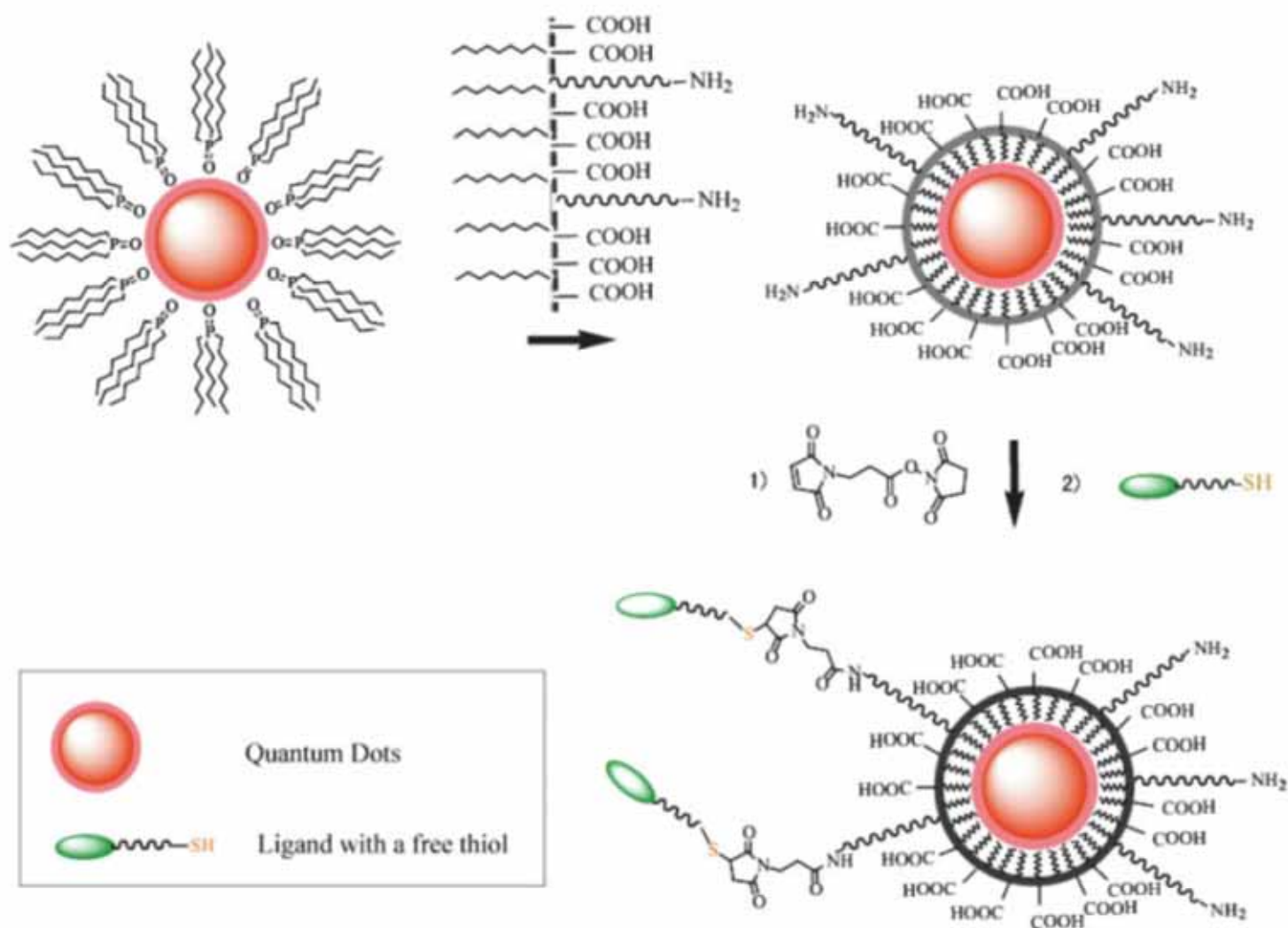
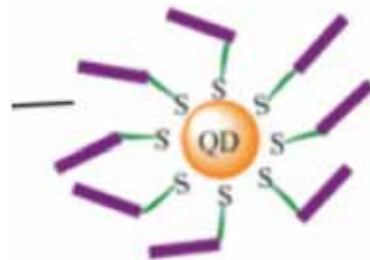


FIGURE 3 Maleimide functionalized QDs for conjugating thiol-containing ligands. TOPO stabilized QDs are coated with a primary amine functionalized tri-block amphiphilic copolymer for producing water-soluble QDs, which facilitate further conjugation to ligands with free thiols through bi-functional cross-linkers.

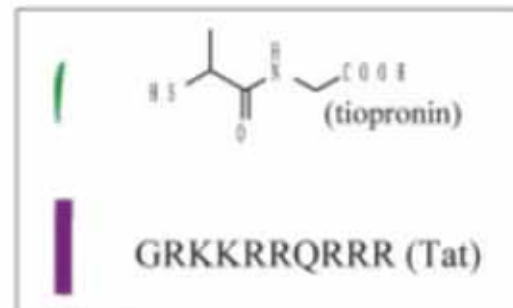




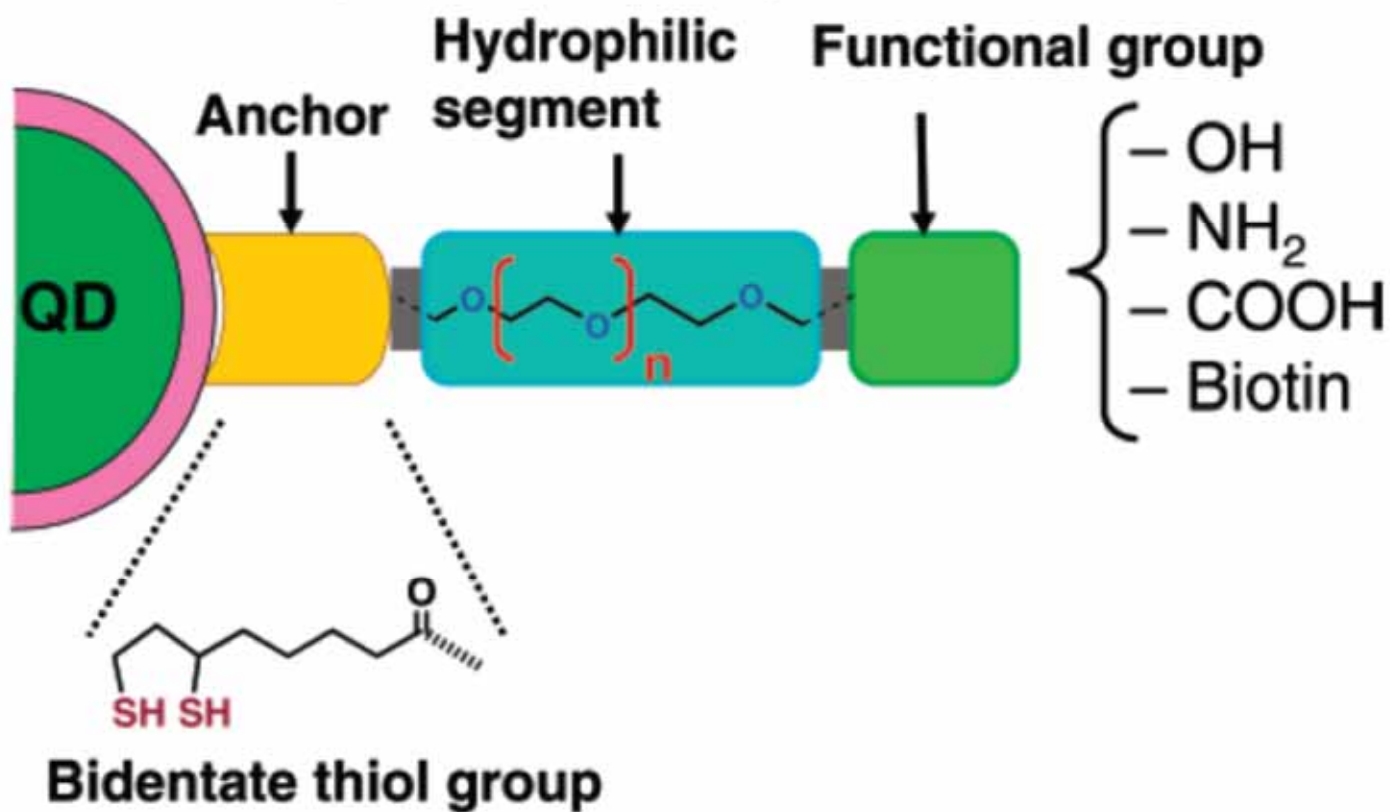
Cells incubated with tiopronin coated QDs



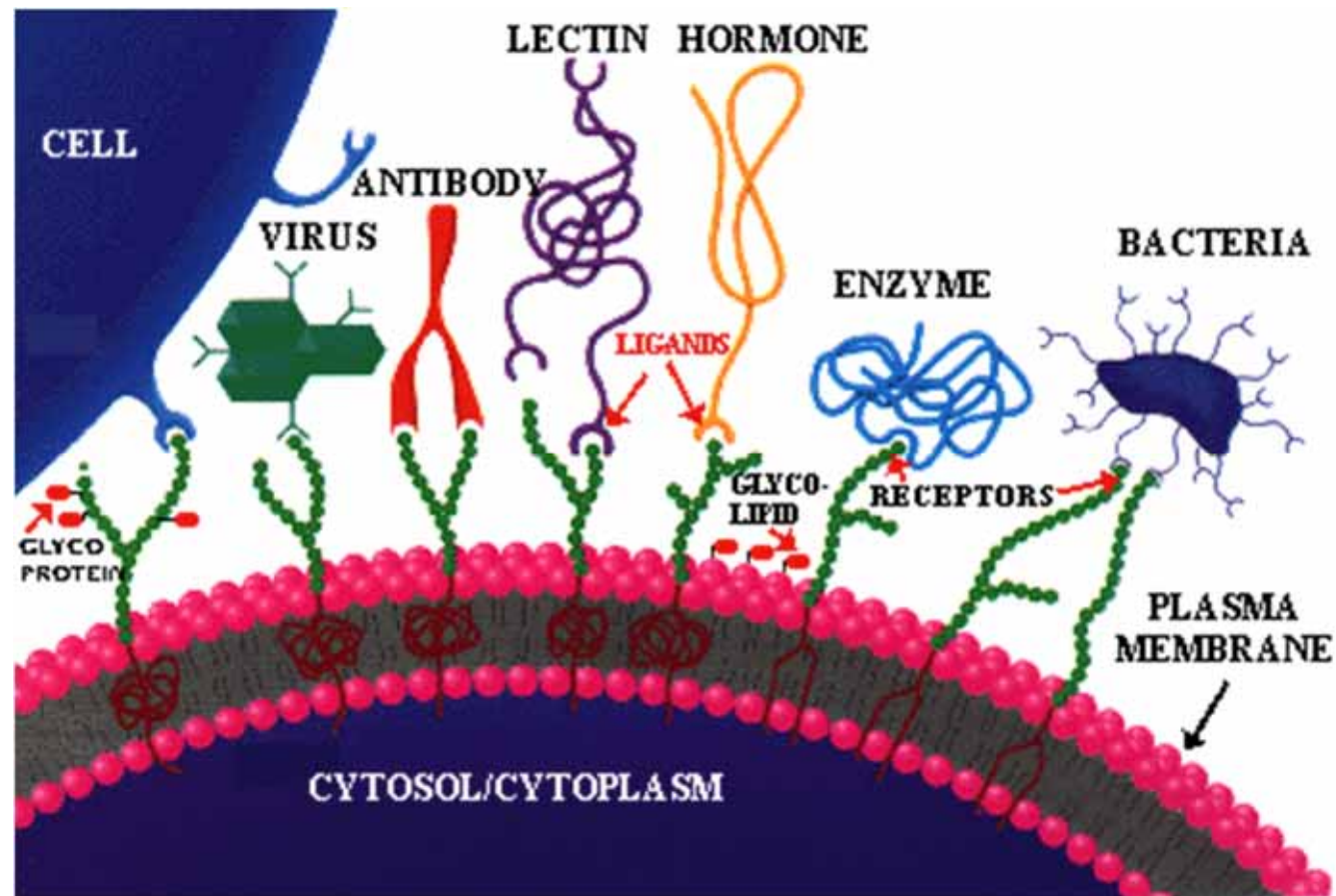
Cells incubated with Tat functionalized QDs



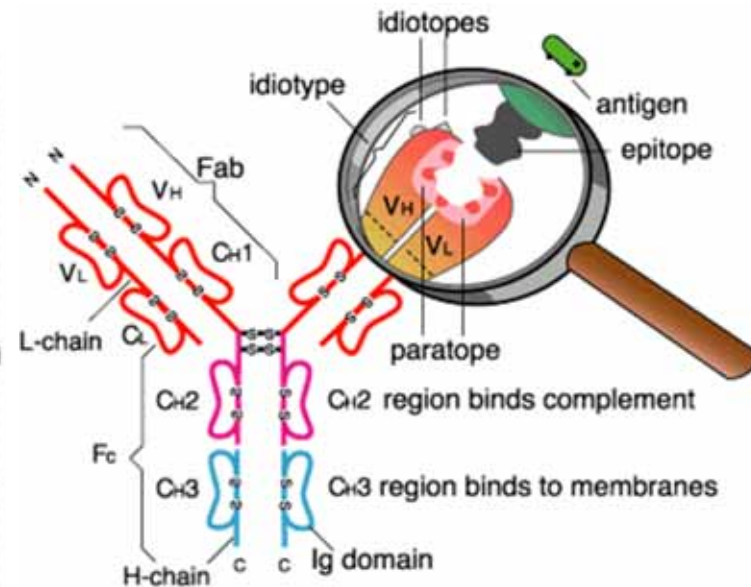
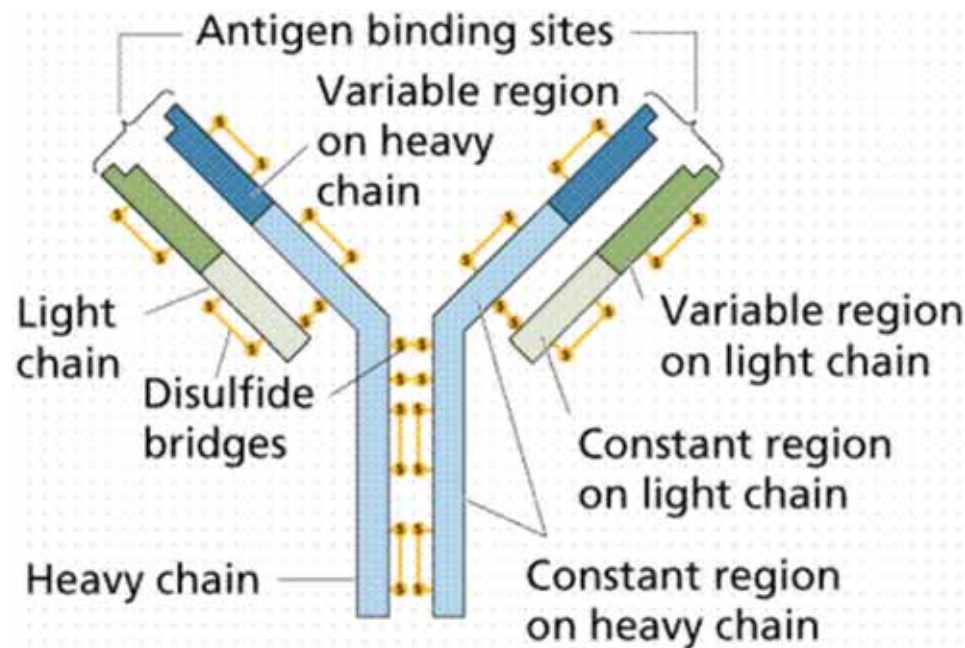
Scheme 1. Modular Design of Hydrophilic Ligands with Terminal Functional Groups Used in This Study



Molecular Recognition



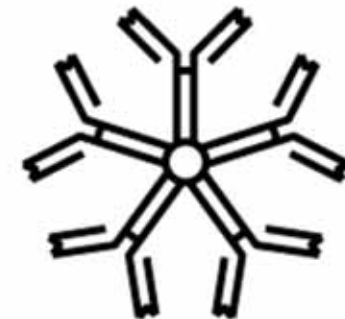
Antibody and Antigen



Bendzen 1996



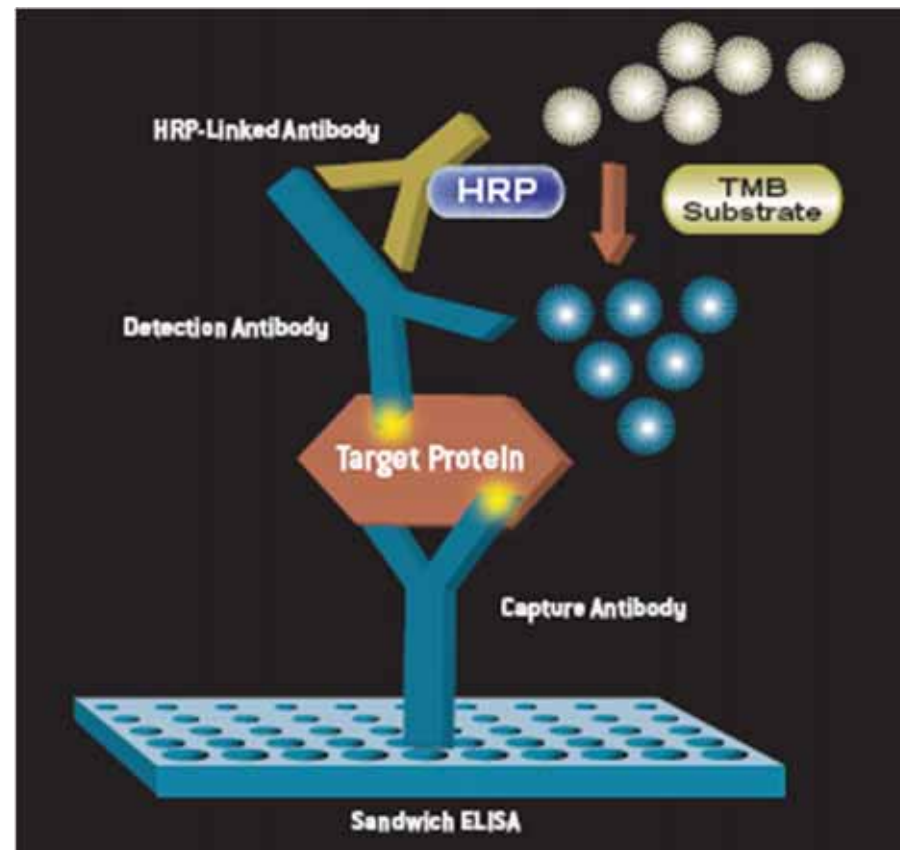
IgG



IgM



Enzyme-Linked ImmunoSorbent Assay (ELISA)

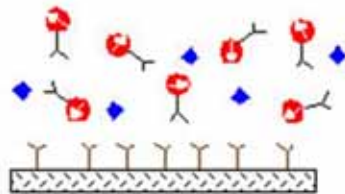


Labeling
BSA/PEG

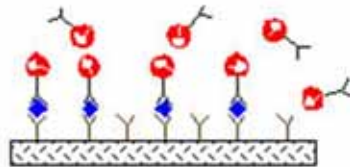


Microarray

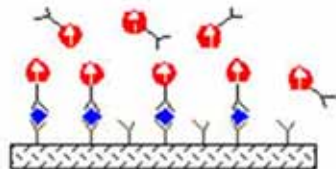
◆ Biomolecules of interest Y Capture antibody ▨ Solid support ● Magnetically labeled antibody



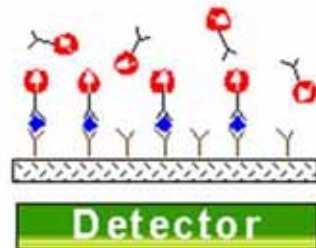
Add biomolecules of interest and magnetically labeled detect antibodies to well coated with capture antibody.



Immobilized immune complexes form on solid support.



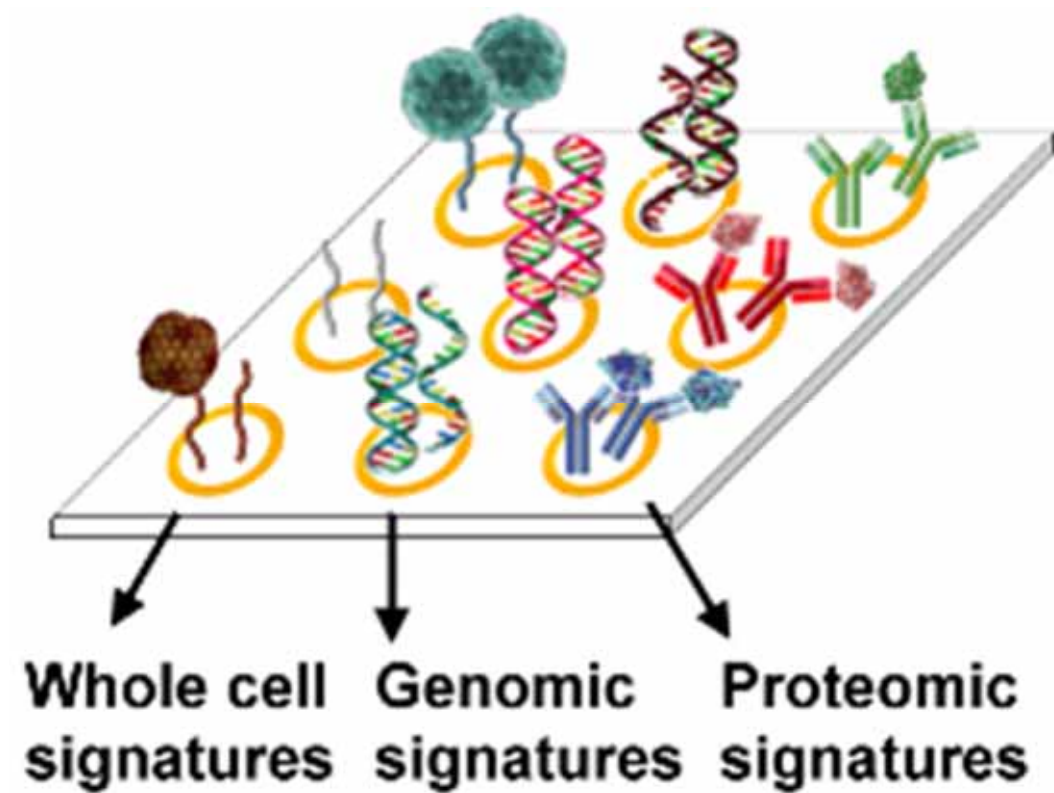
Apply external magnetic field, magnetic dipoles align.



Remove field, measure net magnetization due to bound antibody labels. Unbound labels randomize quickly and contribute no net signal.



Microarray



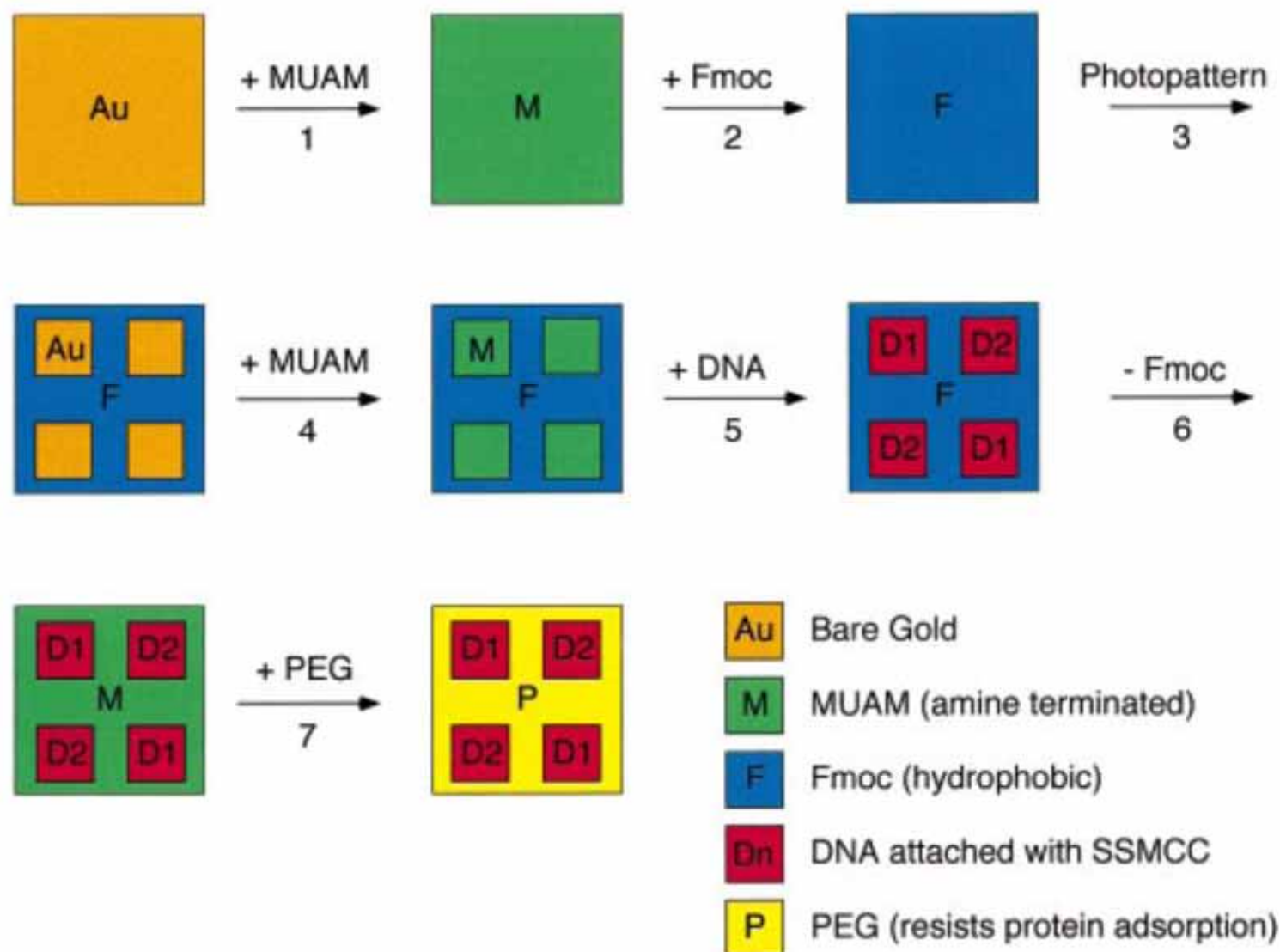


Figure 1. Fabrication scheme for the construction of multi-element DNA arrays. A clean gold surface is reacted with the amine-terminated alkanethiol MUAM, and subsequently reacted with Fmoc-NHS to create a hydrophobic surface. This surface is then exposed to UV radiation through a quartz mask and rinsed with solvent to remove the MUAM+Fmoc from specific areas of the surface, leaving bare gold pads. These bare gold areas on the sample surface are filled in with MUAM, resulting in an array of MUAM pads surrounded by a hydrophobic Fmoc background. Solutions of DNA are then delivered by pipet onto the specific array locations and are covalently bound to the surface via the bifunctional linker SSMCC. In the final two steps, the Fmoc-terminal groups on the array background are removed and replaced by PEG groups which prohibit the nonspecific binding of analyte proteins to the background.



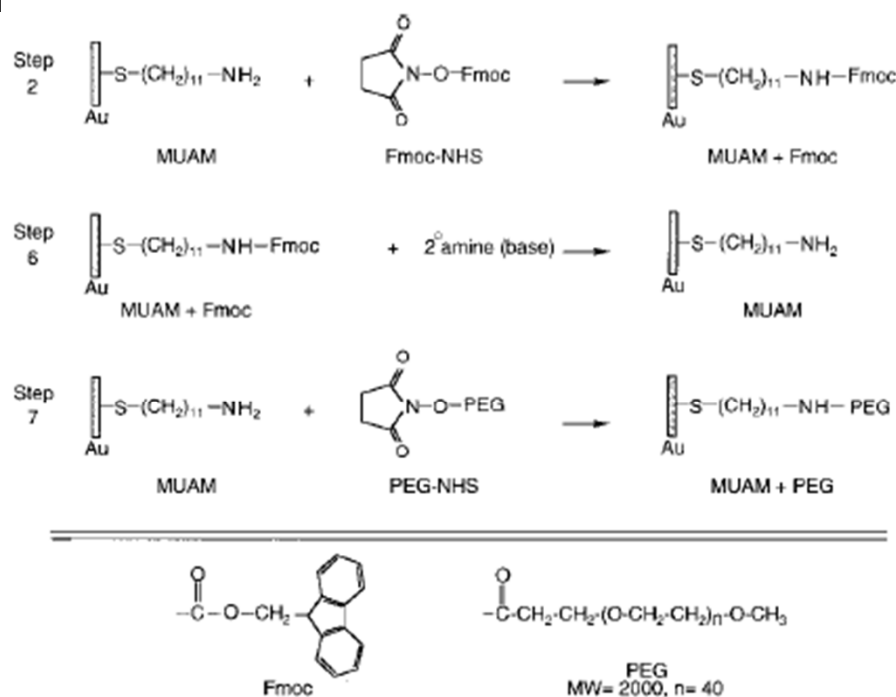


Figure 2. Surface reaction scheme showing the steps involved in the reversible modification of the array background. (Step 2) The starting amine-terminated alkanethiol surface (MUAM) is reacted with the Fmoc-NHS protecting group to form a carbamate linkage thus creating a hydrophobic Fmoc-terminated surface. (Step 6) After DNA immobilization (see Figure 3), the hydrophobic Fmoc group is removed from the surface with a basic secondary amine, resulting in the return of the original MUAM surface. (Step 7) In the final array fabrication step, the deprotected MUAM is reacted with PEG-NHS to form an amide bond that covalently attaches PEG to the array surface.

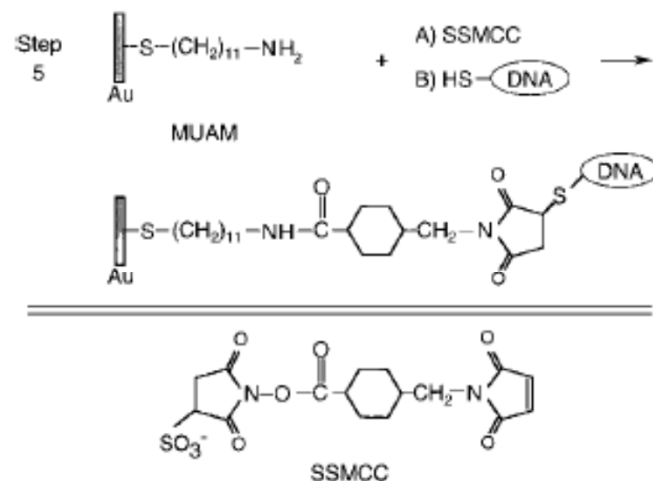
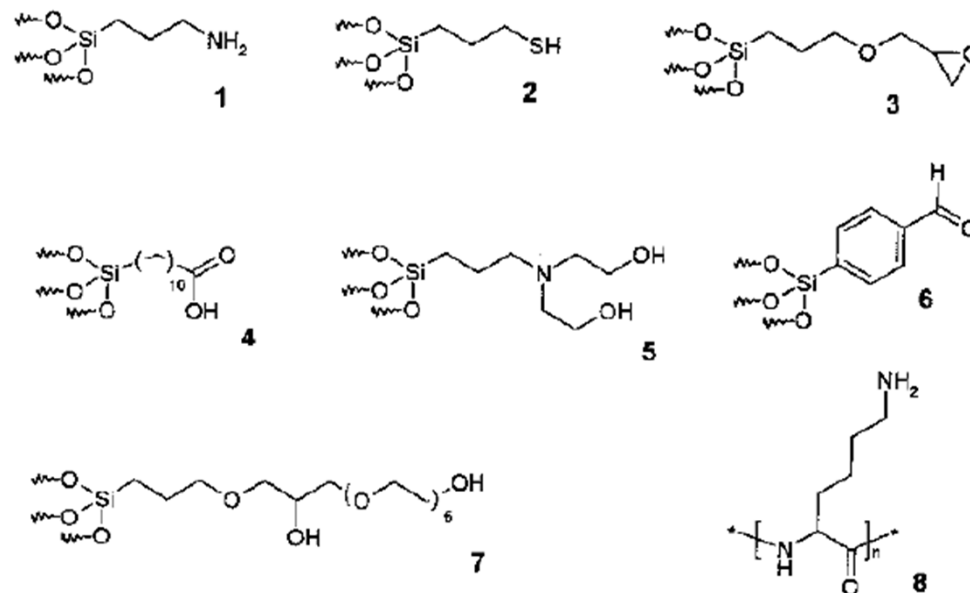
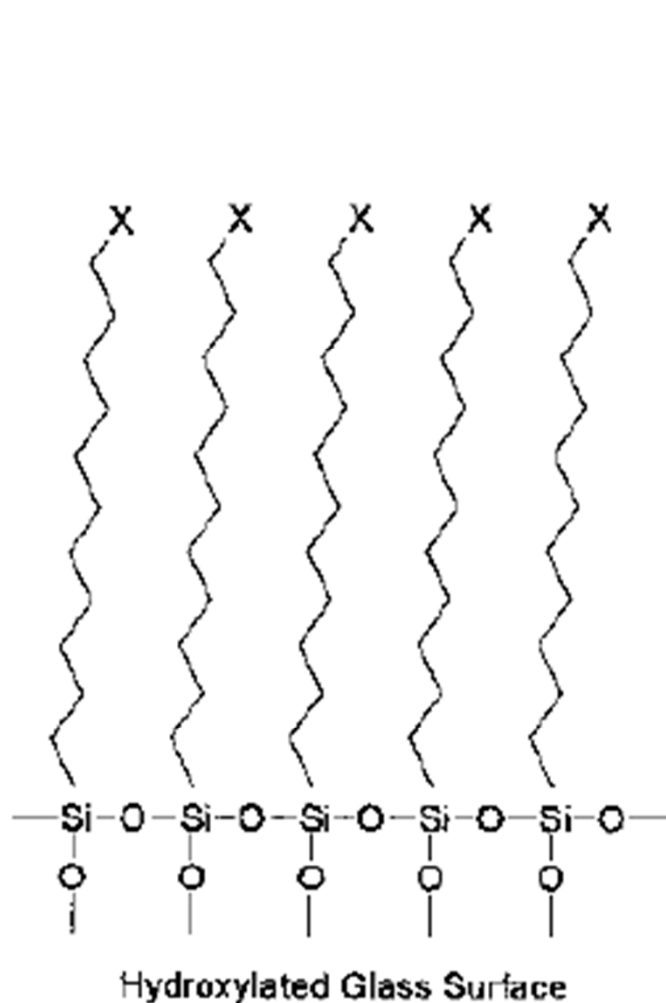


Figure 3. Surface reaction scheme showing the immobilization of thiol-terminated DNA to the array surface. In Step 5 of the DNA array fabrication, the heterobifunctional linker SSMCC is used to attach 5'-thiol modified oligonucleotide sequences to reactive pads of MUAM. This linker contains an NHSS ester functionality (reactive toward amines) and a maleimide functionality (reactive toward thiols). The surface is first exposed to a solution of the linker, whereby the NHSS ester end of the molecule reacts with the MUAM surface. Excess linker is rinsed away and the array surface is then spotted with 5'-thiol-modified DNA that reacts with the maleimide groups forming a covalent bond to the surface monolayer.



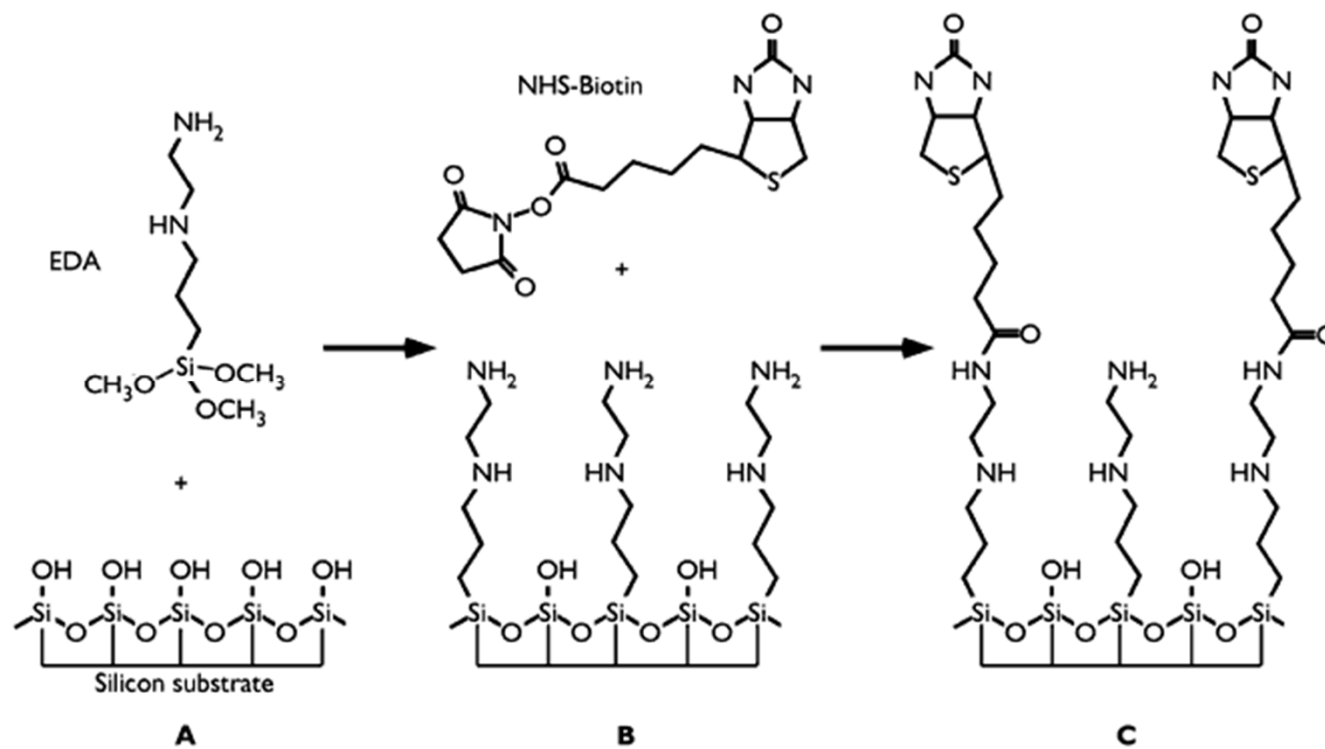
Glass Surface Modification



Scheme 2.2 Reagents for derivatization of glass surfaces. 1 APTES = aminopropyltriethoxysilane; 2 MPTS = 3-mercaptopropyltrimethoxysilane; 3 GPTS = glycidoxypropyltrimethoxysilane; 4 TETU = triethoxysilane undecanoic acid;

5 HE-APTS = bis(hydroxyethyl)aminopropyltriethoxysilane; 6 4-trimethoxysilylbenzaldehyde; 7 GPTS/HEG = glycidoxypropyltrimethoxysilane-hexaethylene glycol; 8 poly(lysine).

Scheme 2.1 2D schematic description of a polysiloxane monolayer on a glass surface (X = terminal functional)



Biotin-Streptavidin

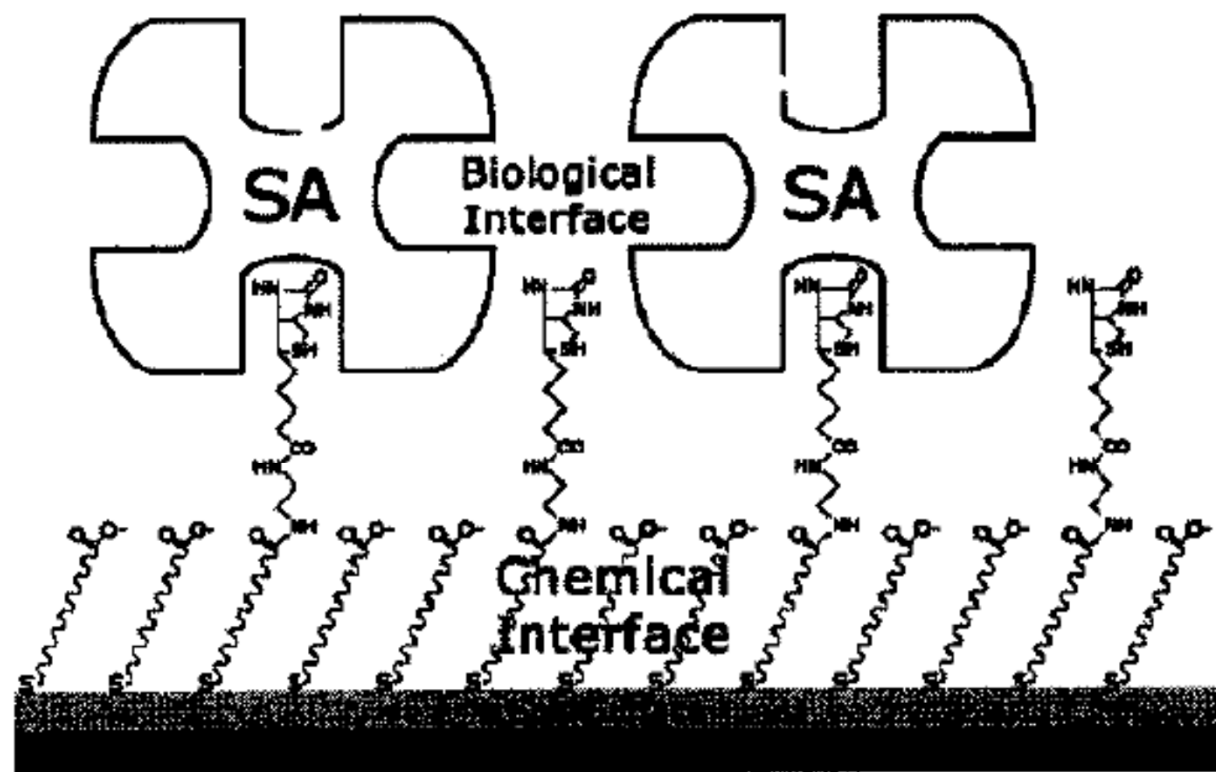
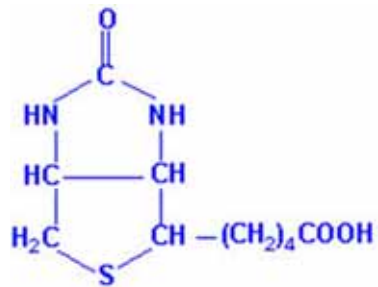


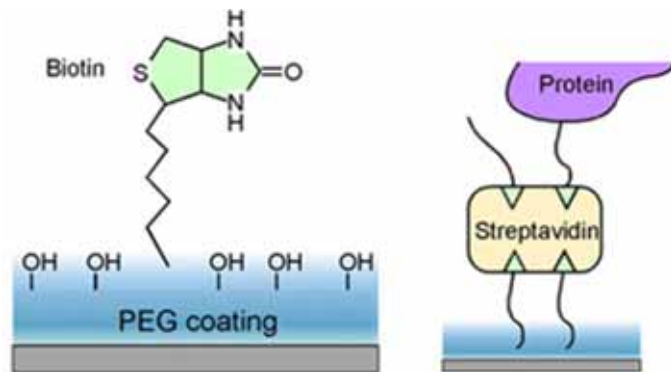
Figure 2.3 Schematic representation of a streptavidin sensor surface assembled on a reaction-controlled biotinylated SAM [28].

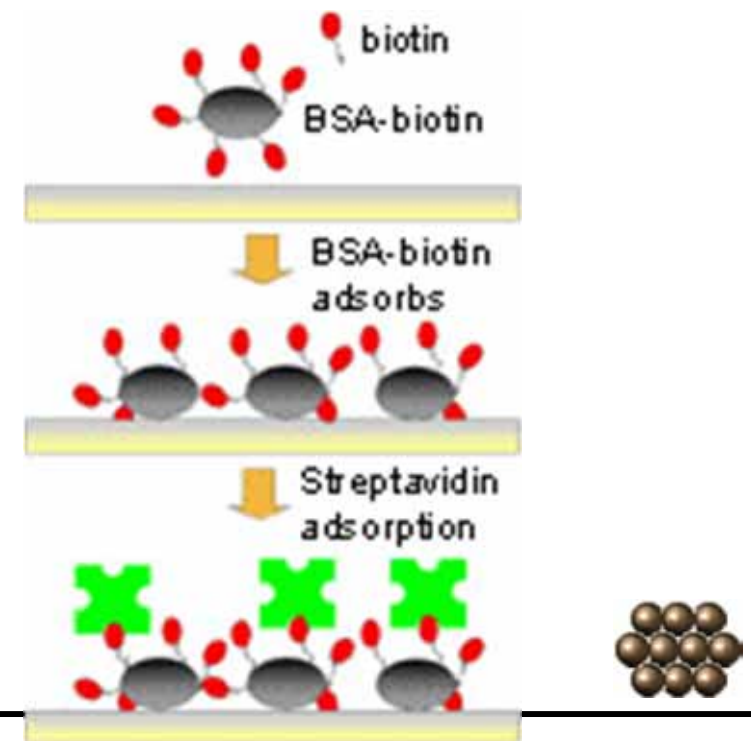
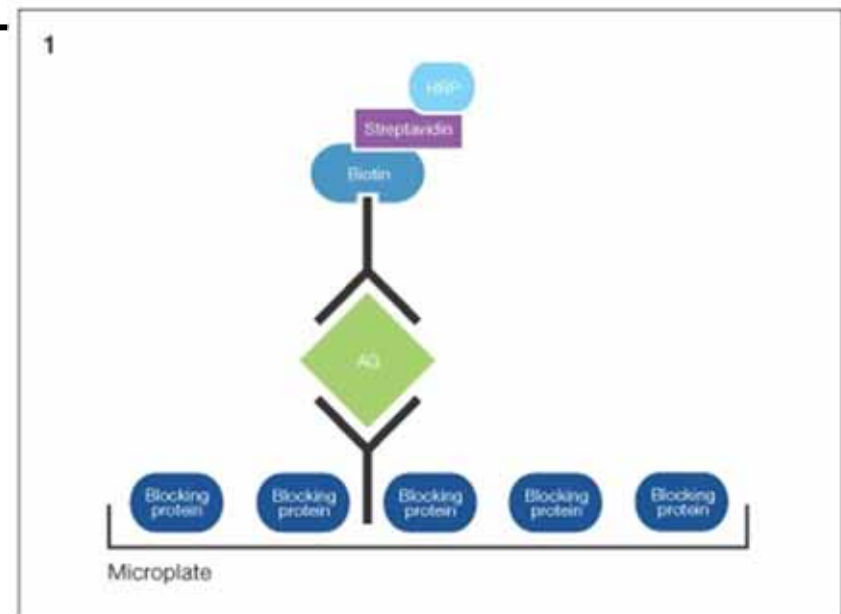
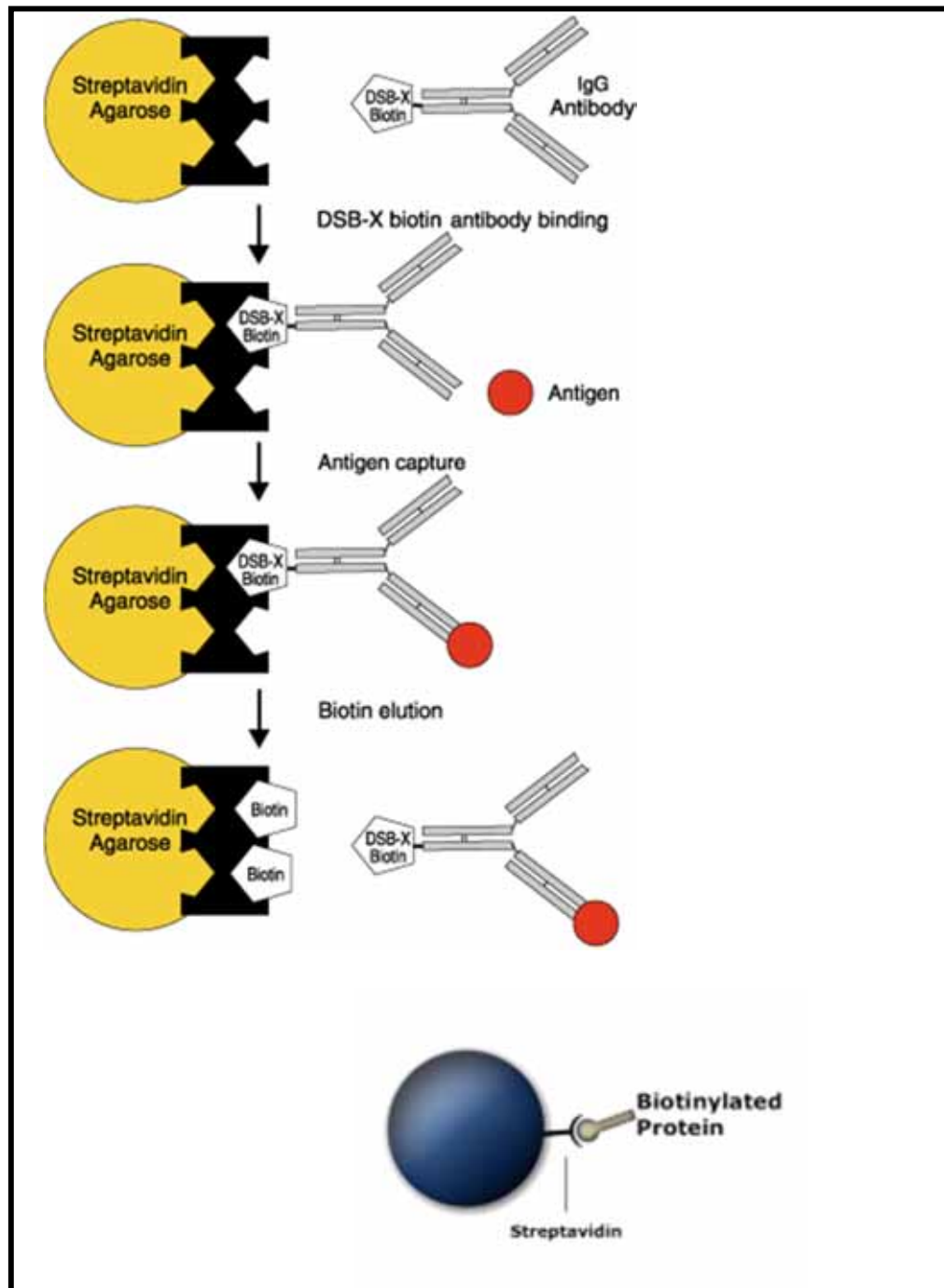


Biotin

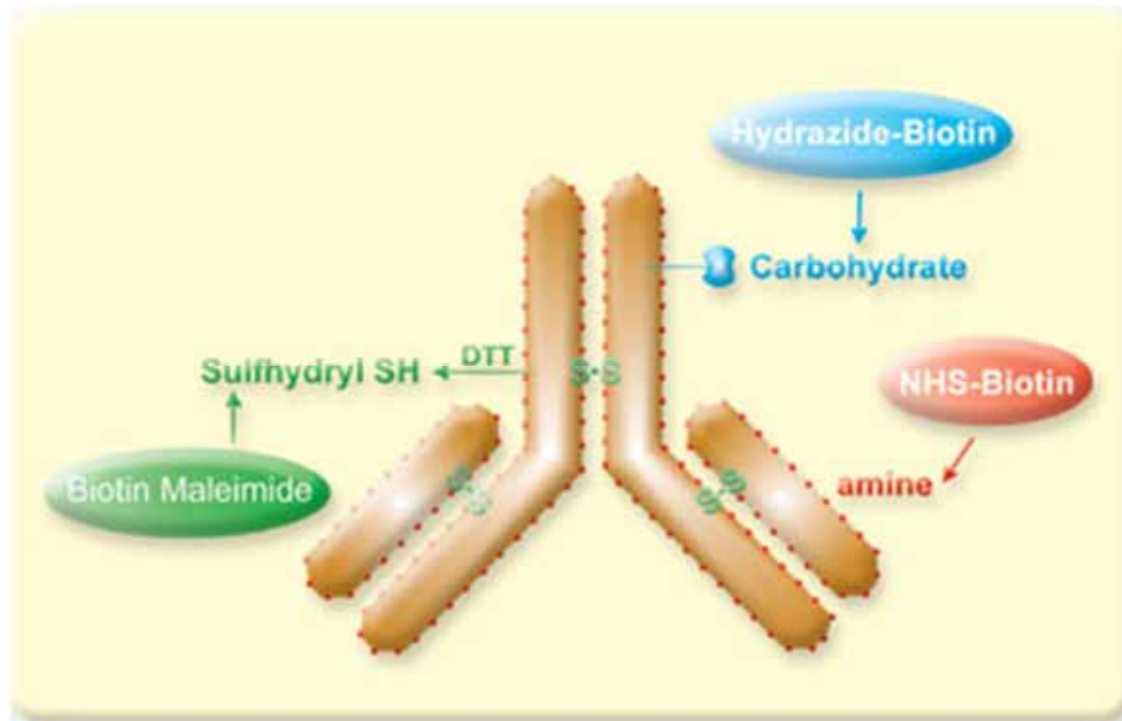


Avidin has a very strong affinity for biotin with a K_D (dissociation constant) of approximately 10^{-15} M^{-1}

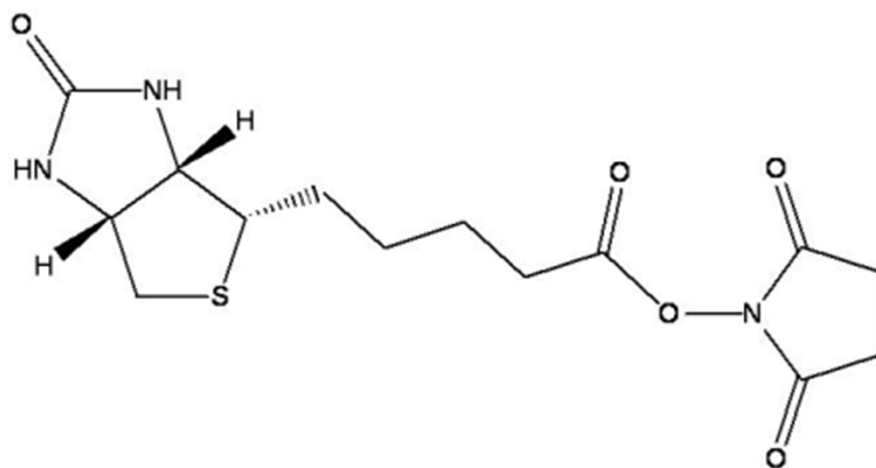




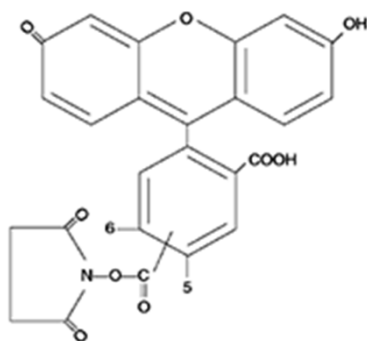
Protein Labeling



Amine Reactive Labeling



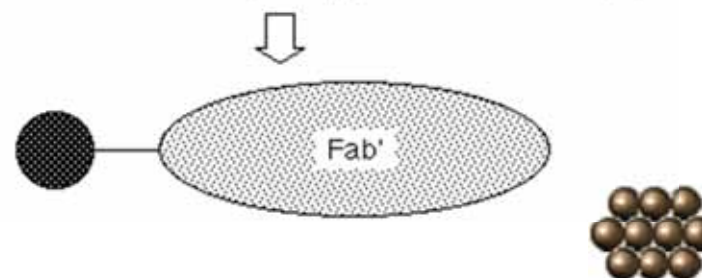
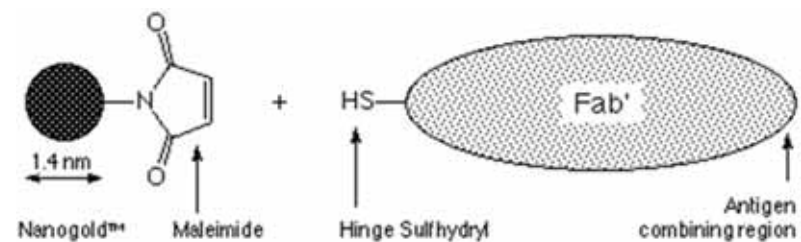
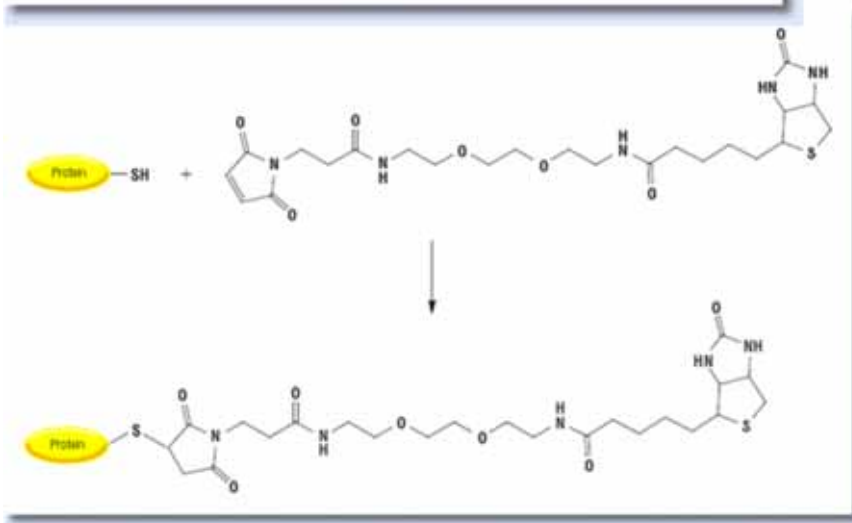
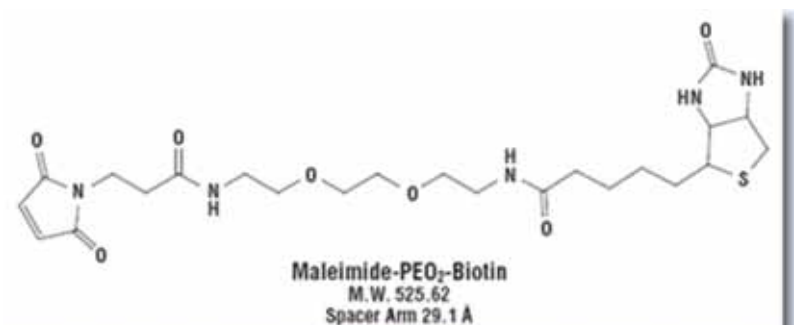
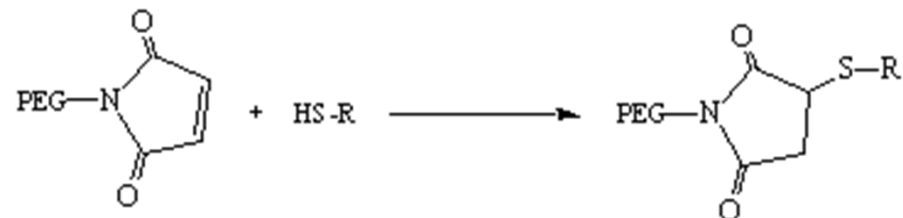
NHS ester

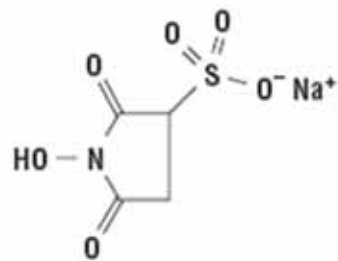


NHS-Fluorescein
MW 473.4

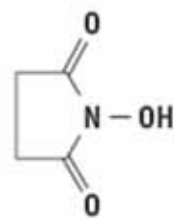


Sulfhydryl Labeling

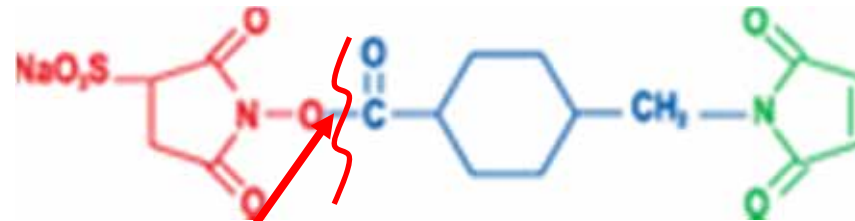




Sulfo-NHS
M.W. 217.13



NHS
M.W. 115.09

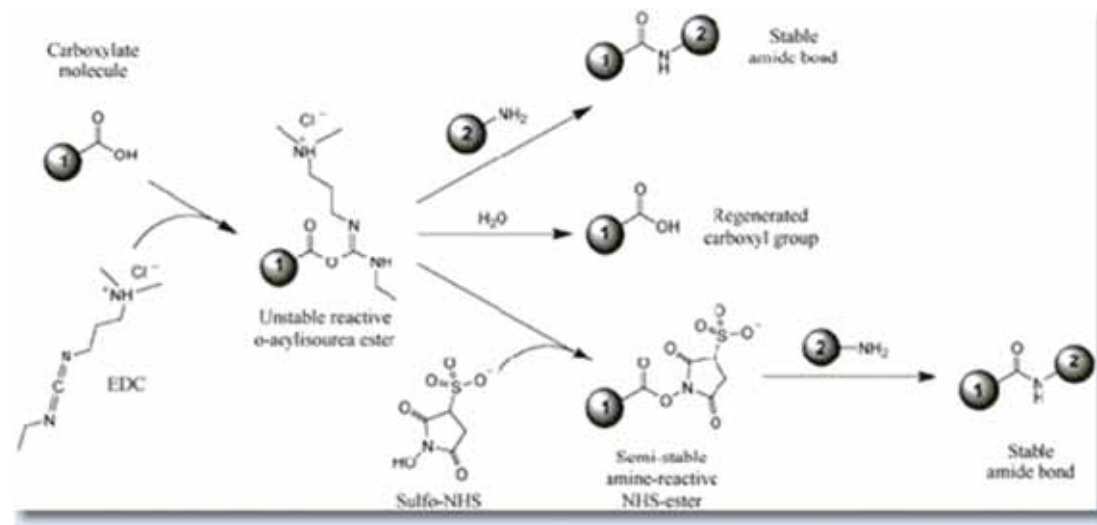
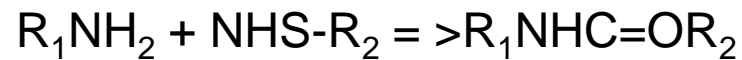


SulfoSuccinimidyl-4-(N-Maleimidomethyl)Cyclohexane-1-Carboxylate
SSMCC

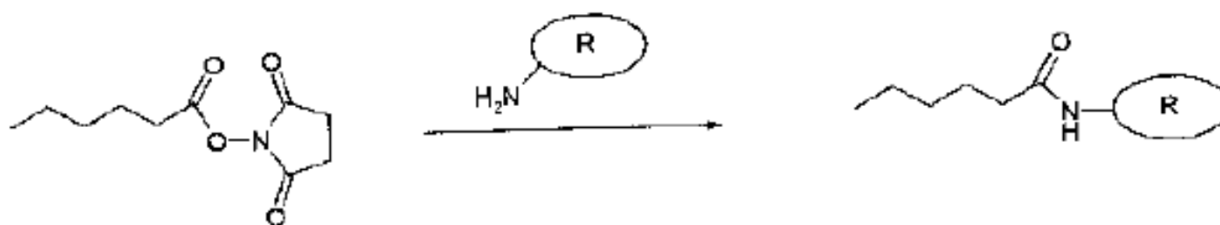
The most popular NH_2 - and SH - crosslinker

N-hydroxysuccinimide

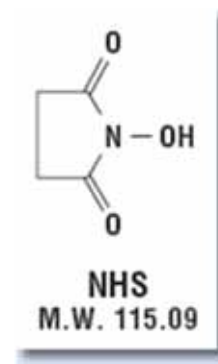
$\text{NH}_2 \Rightarrow$ amide



N-hydroxysuccinimide (NHS)



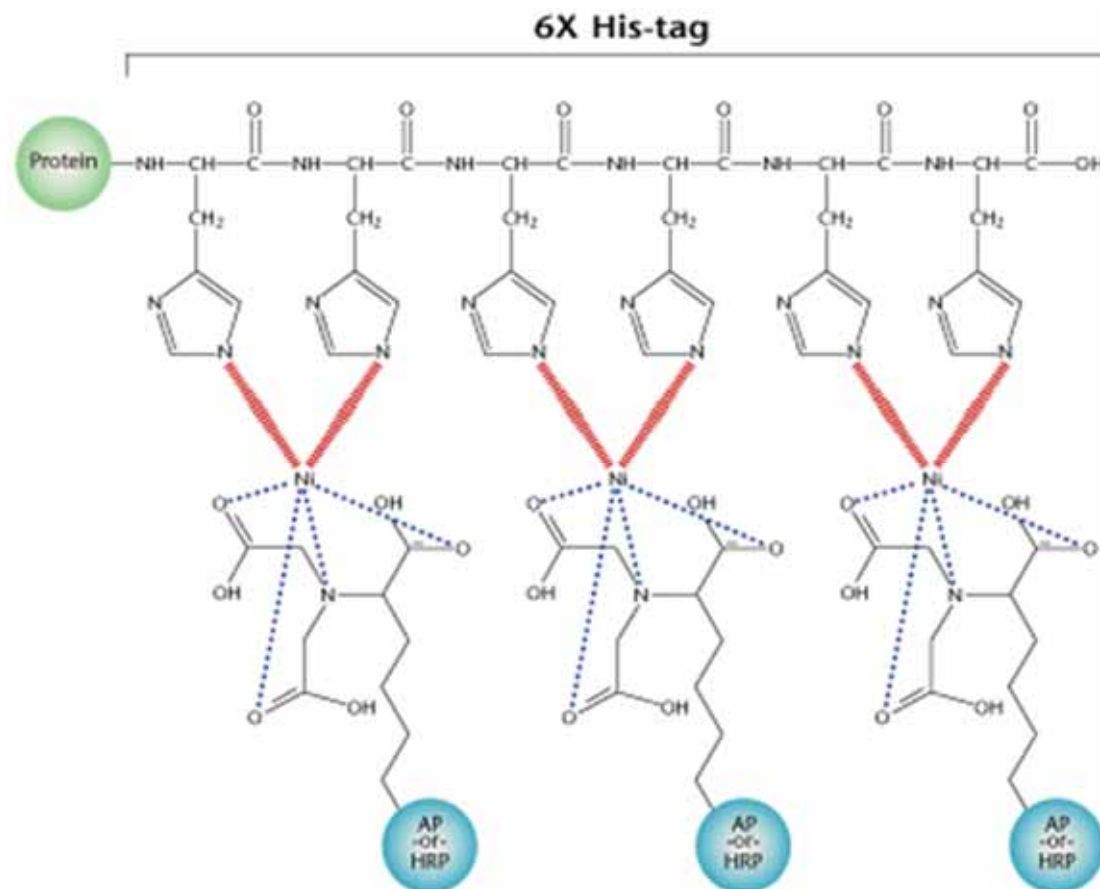
Scheme 2.6 Surface coupling reaction of NHS-esters with the amino residues of the side-chains of polypeptides (lysine units). R, protein.



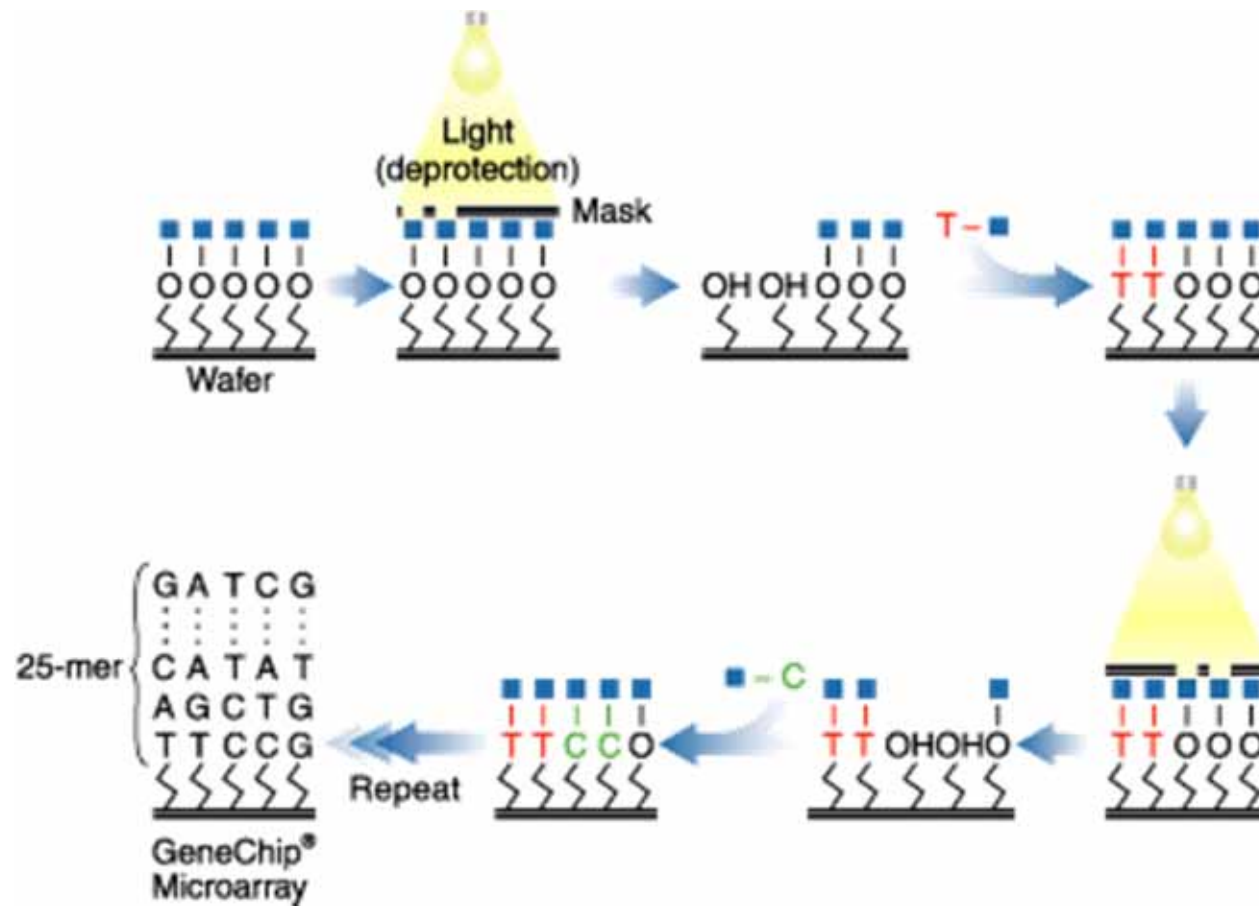
N-hydroxysuccinimide



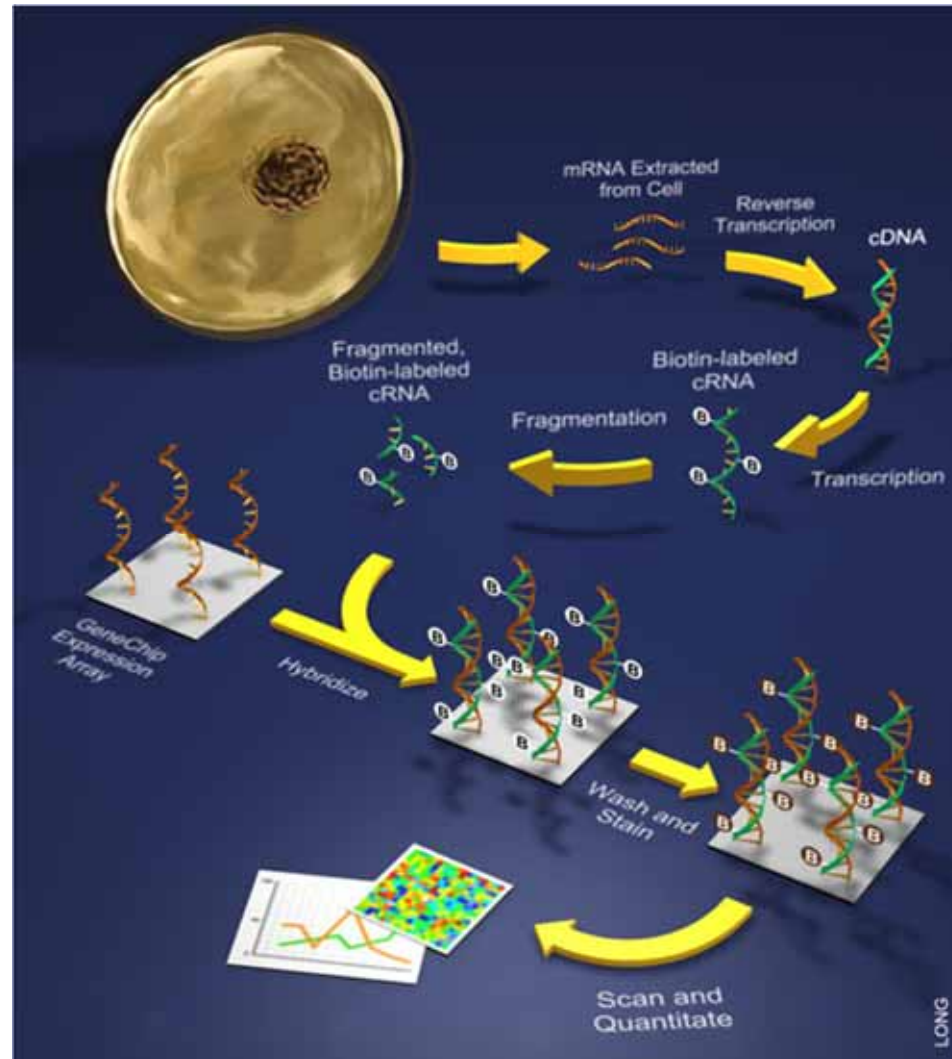
His Tag



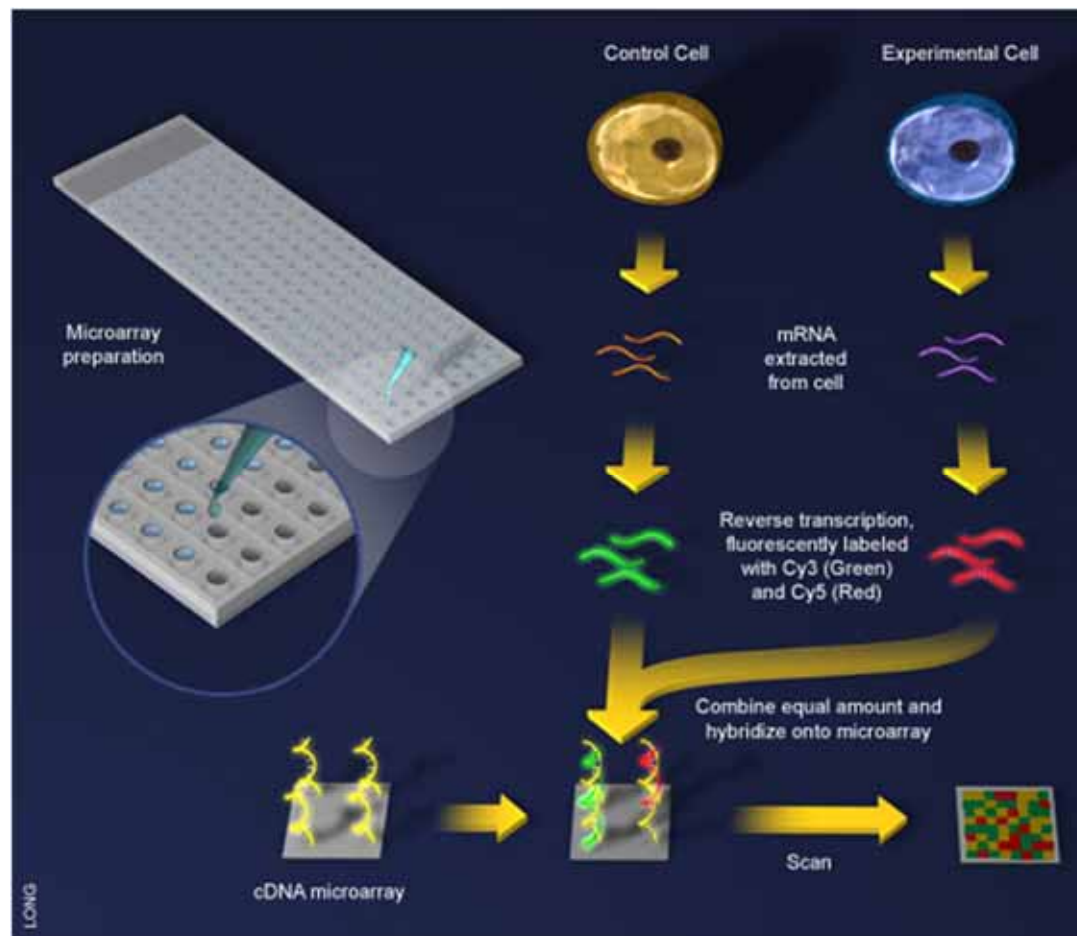
GeneChip



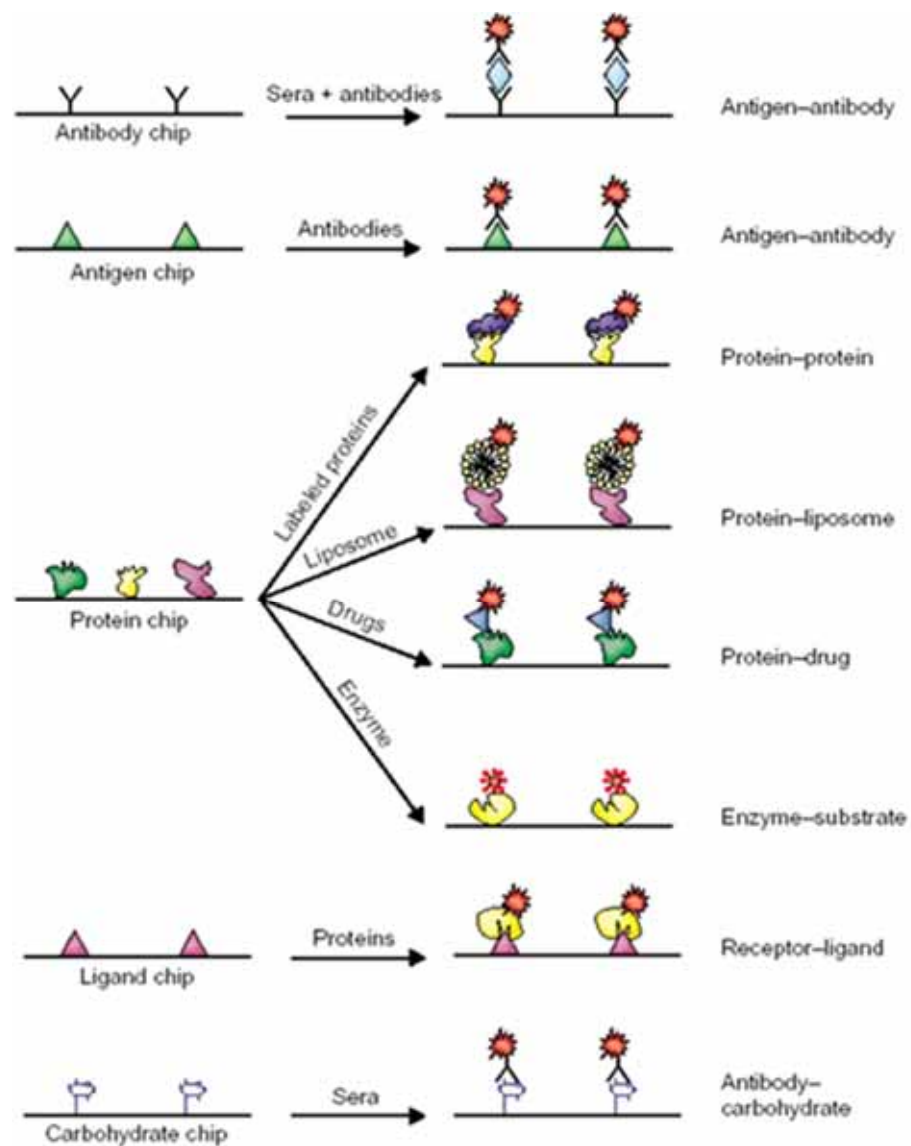
Scheme



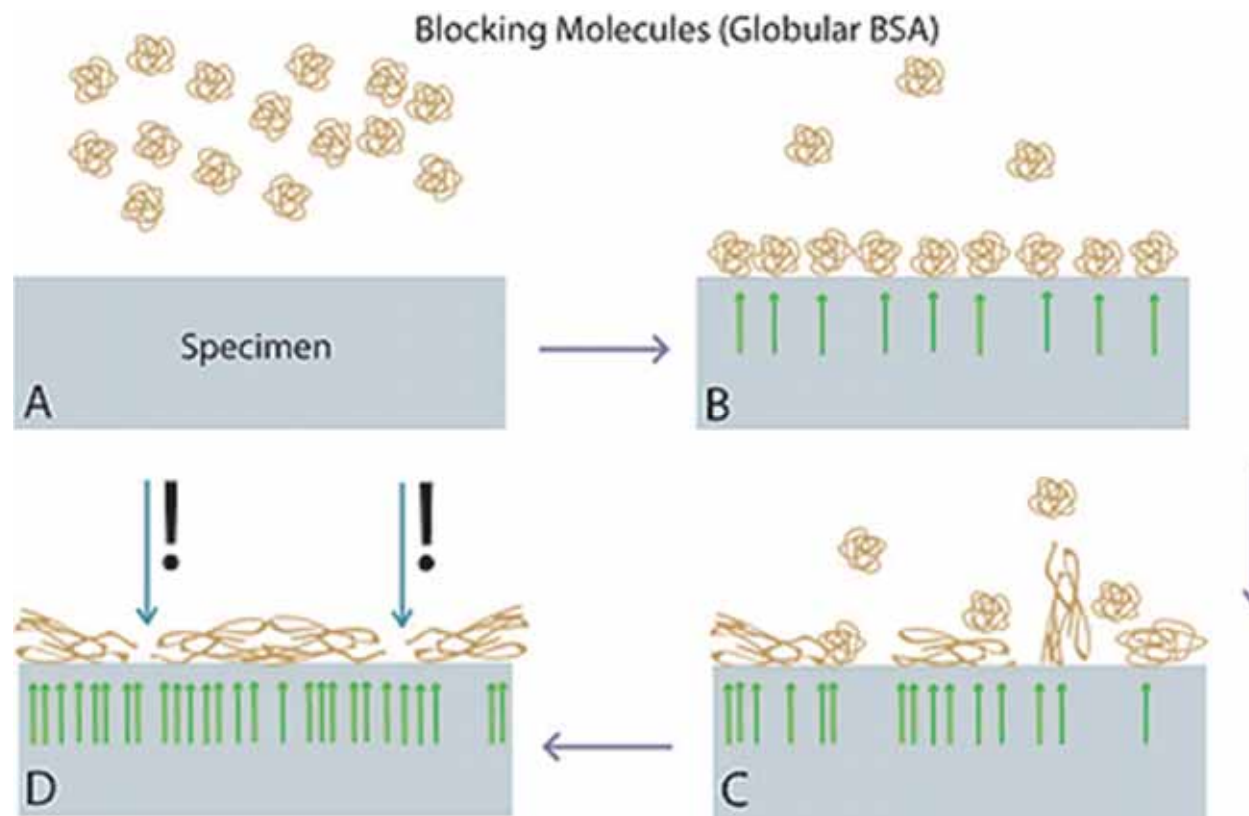
cDNA Microarray



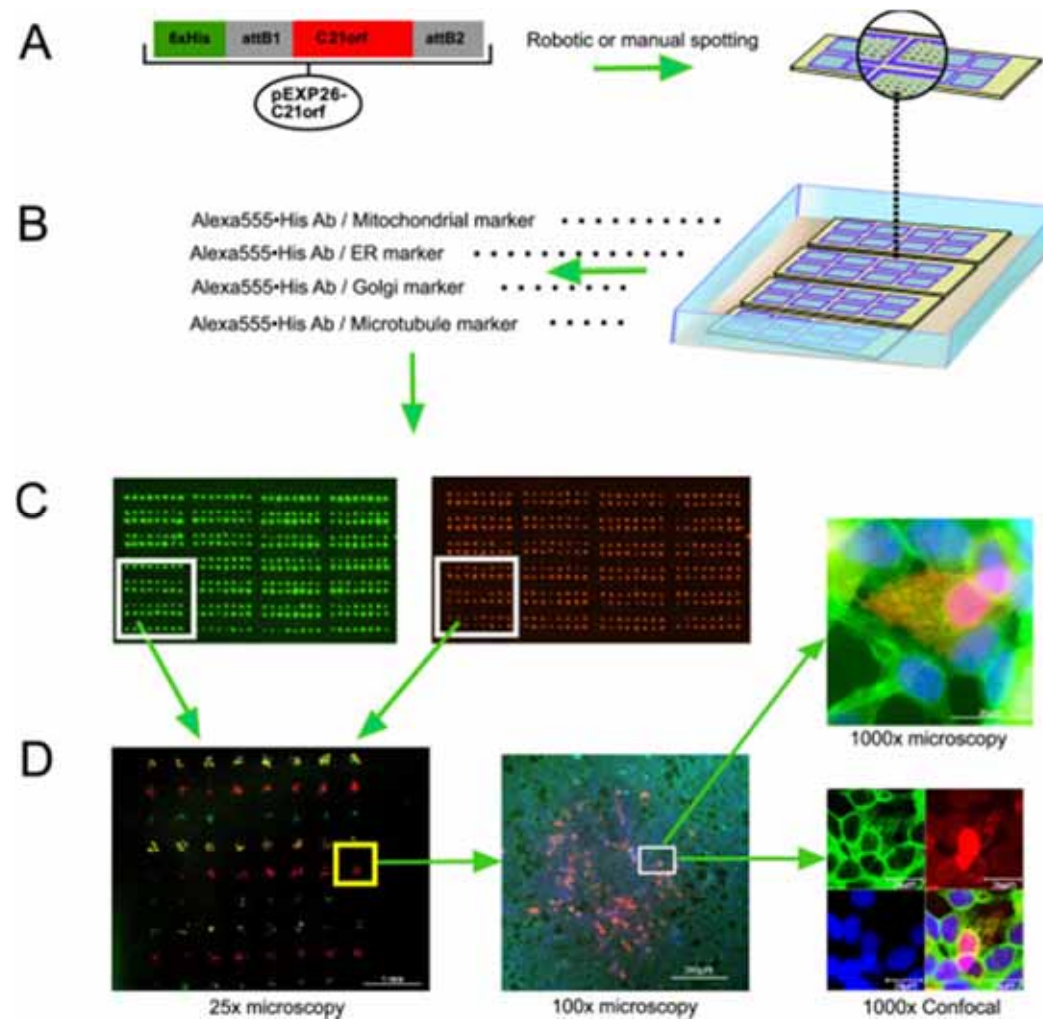
Protein Array



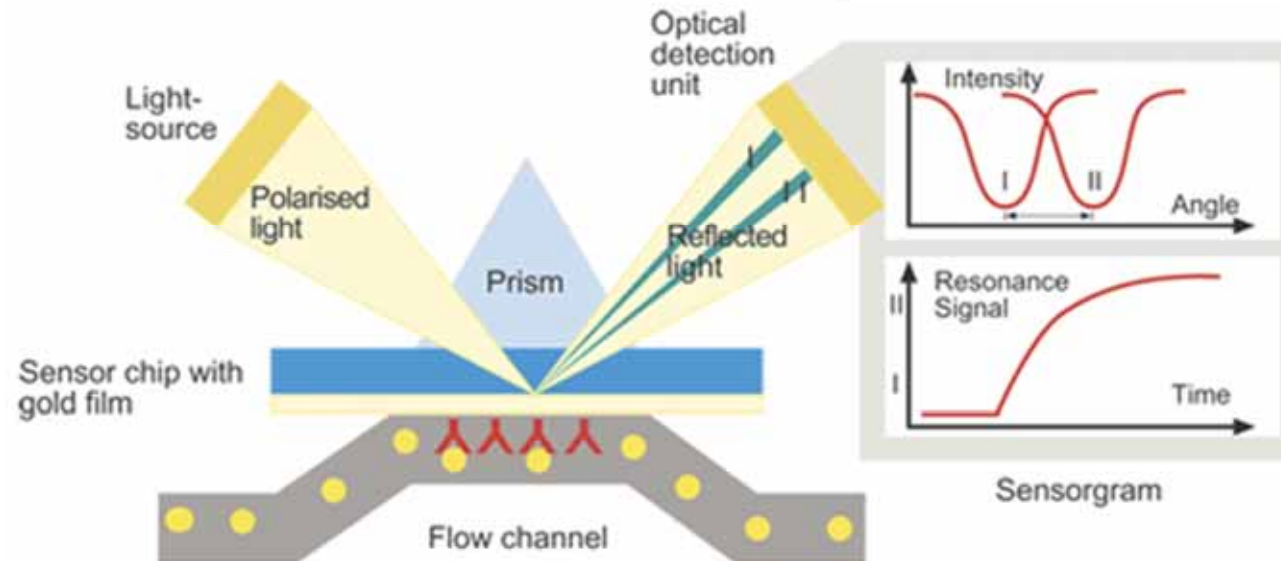
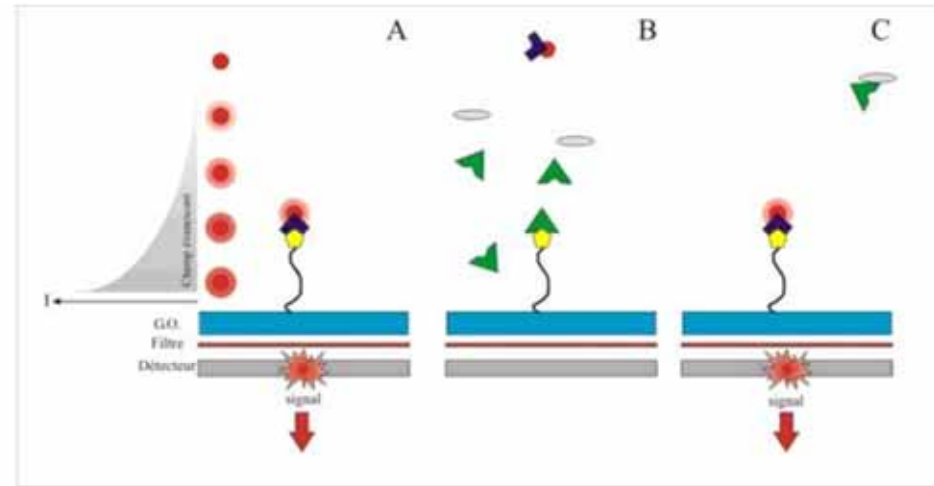
BSA Blocking



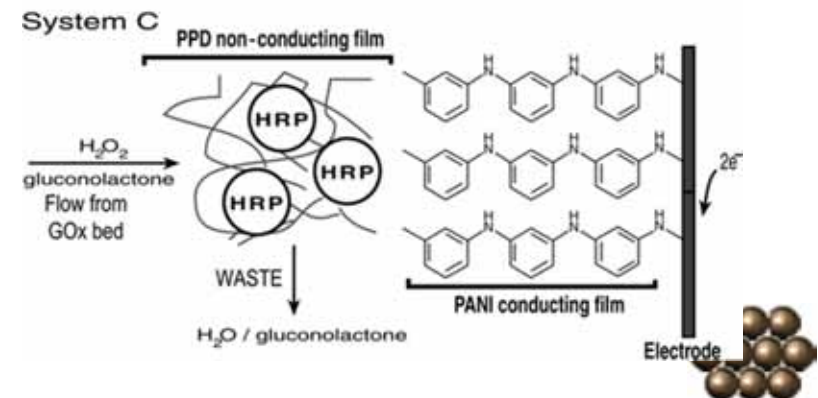
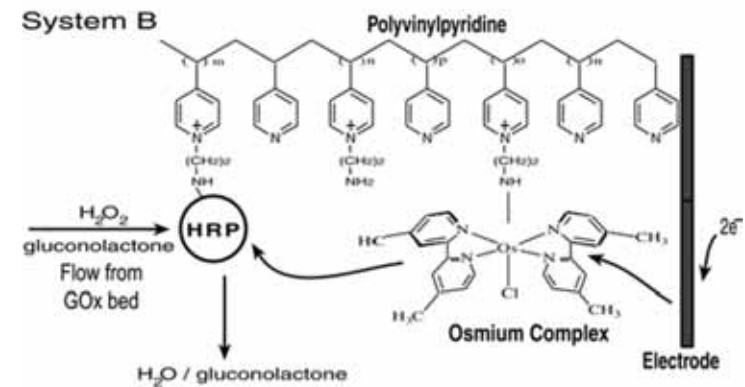
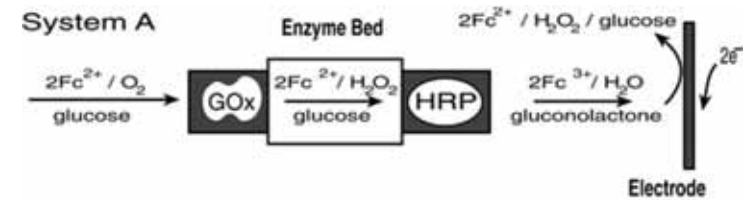
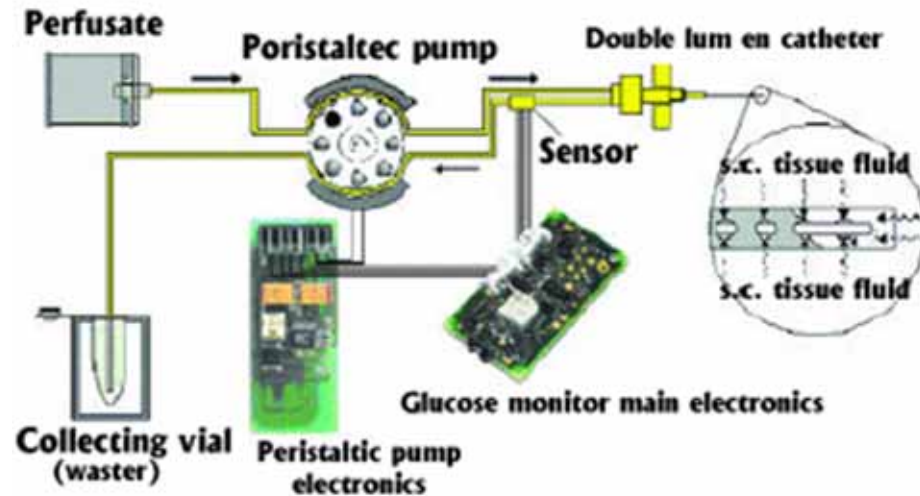
Cell Array



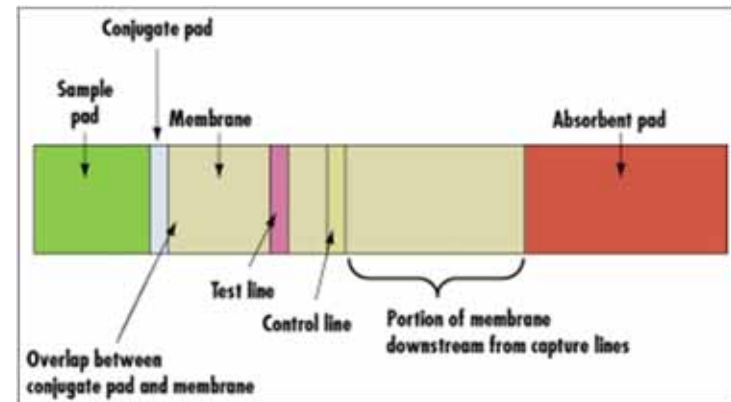
Surface Plasmon Resonance (SPR)



Glucose Sensor



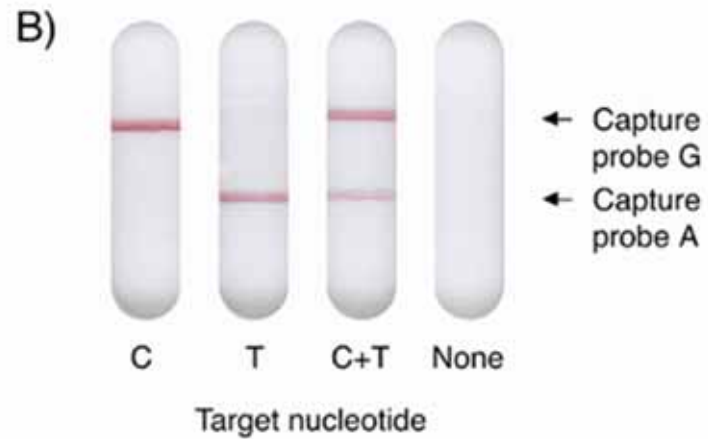
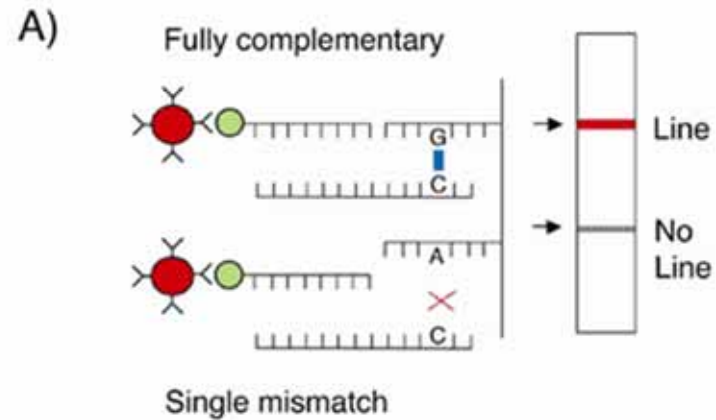
hCG immunoassay



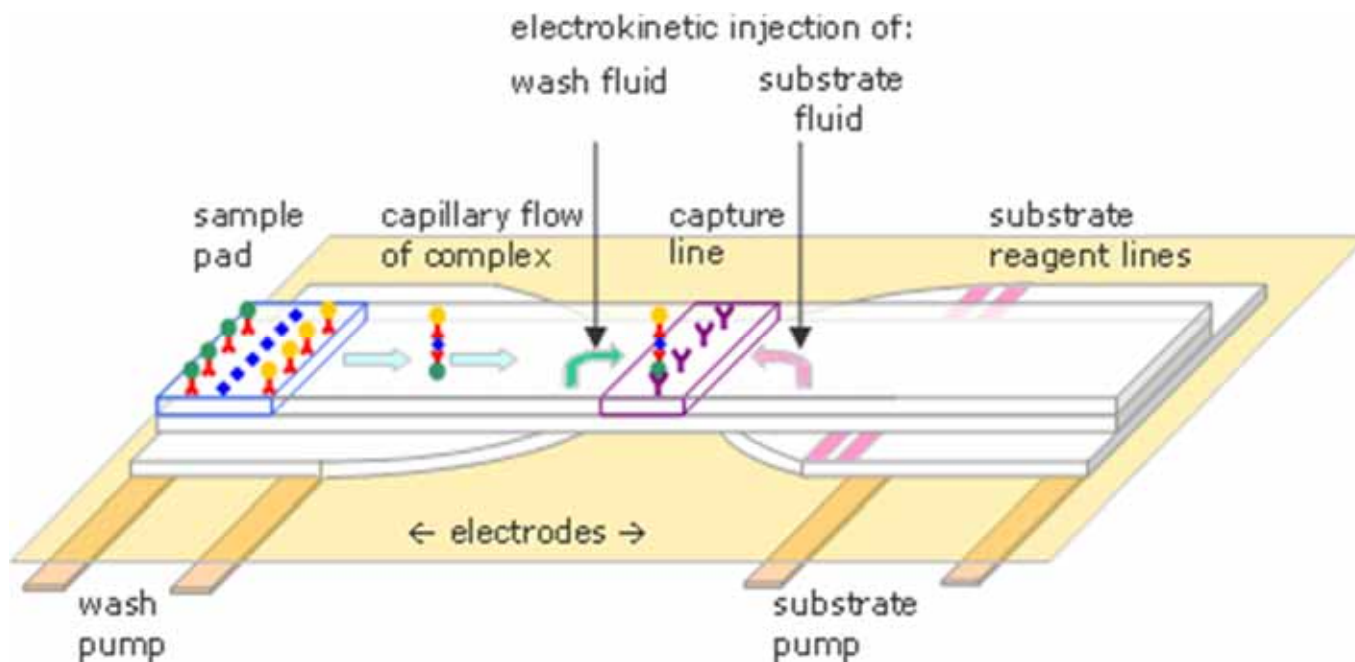
human chorionic gonadotropin (hCG)



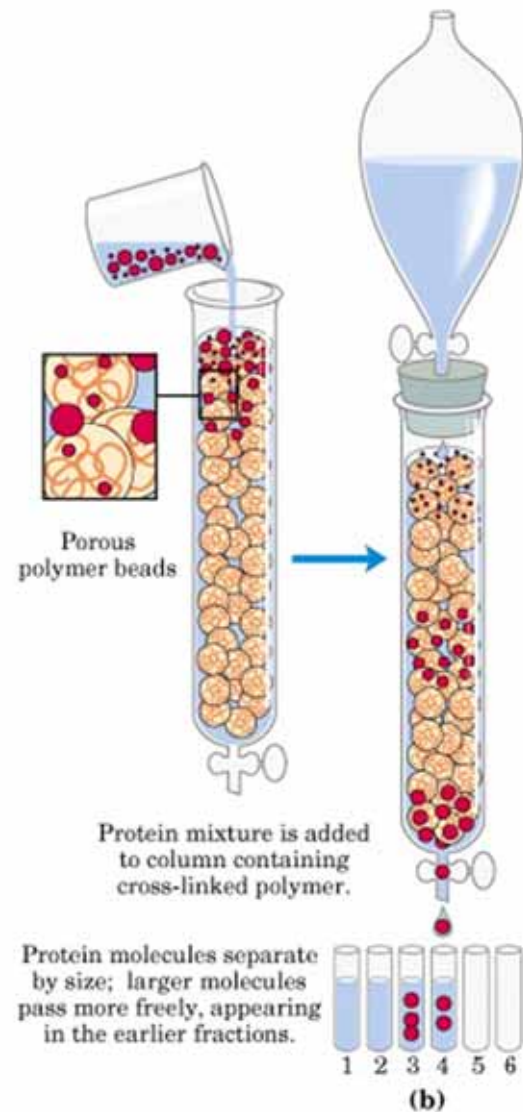
Nucleotide Sensor



Microfluidic Immunoassay

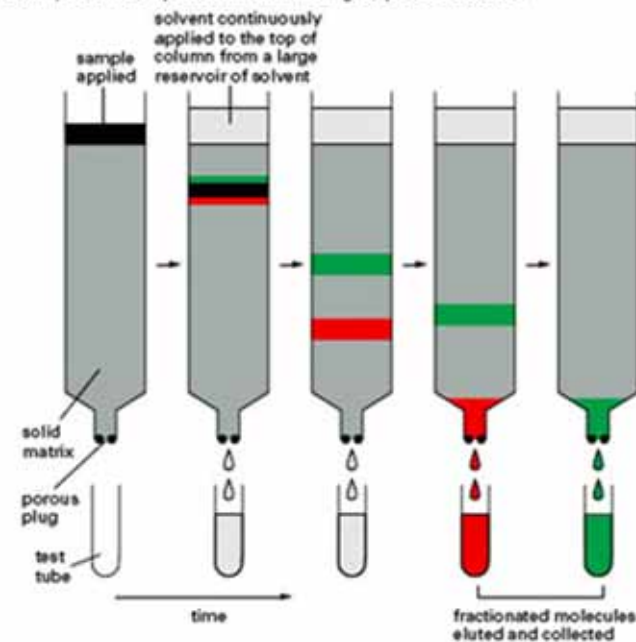


Chromatography

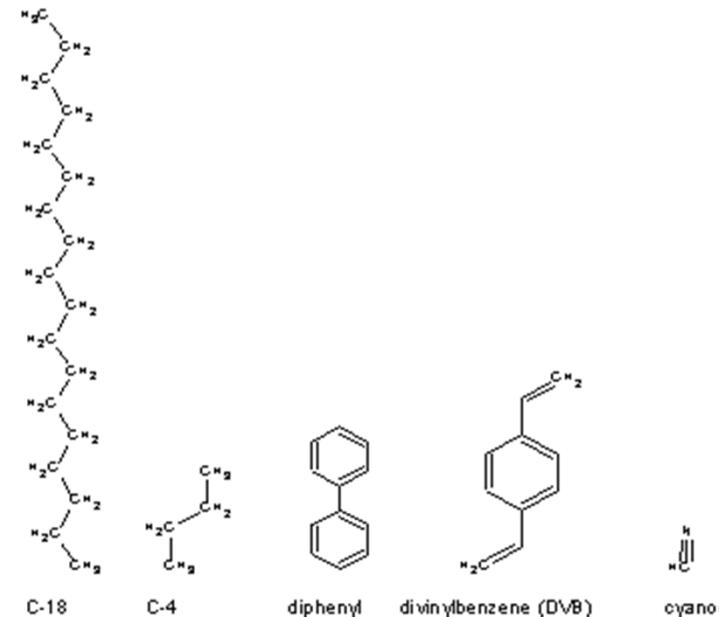
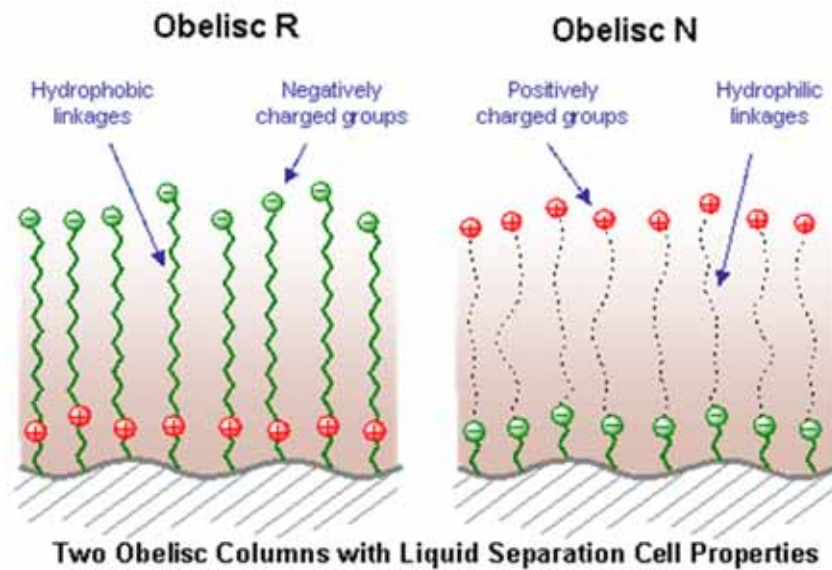


COLUMN CHROMATOGRAPHY

Proteins are often fractionated by **column chromatography**. A mixture of proteins in solution is applied to the top of a cylindrical column filled with a permeable solid matrix immersed in solvent. A large amount of solvent is then pumped through the column. Because different proteins are retarded to different extents by their interaction with the matrix, they can be collected separately as they flow out from the bottom. According to the choice of matrix, proteins can be separated according to their charge, hydrophobicity, size, or ability to bind to particular chemical groups (see *below*).



Reverse Phase



Surface Plasmon

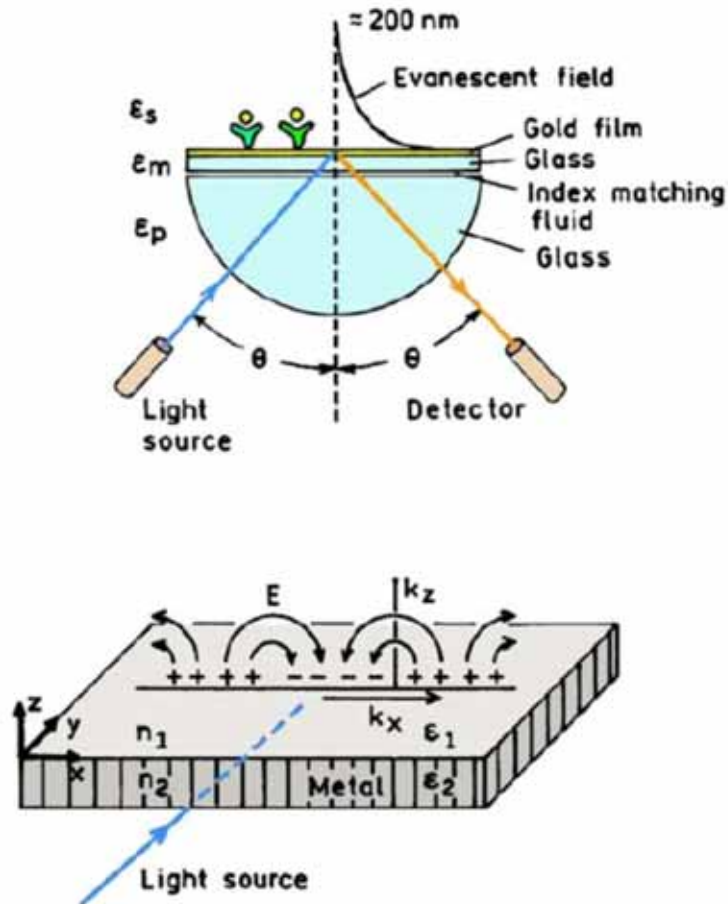
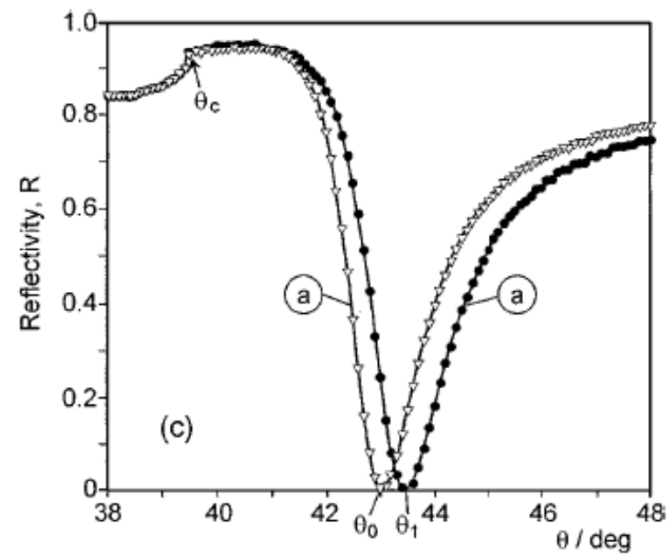
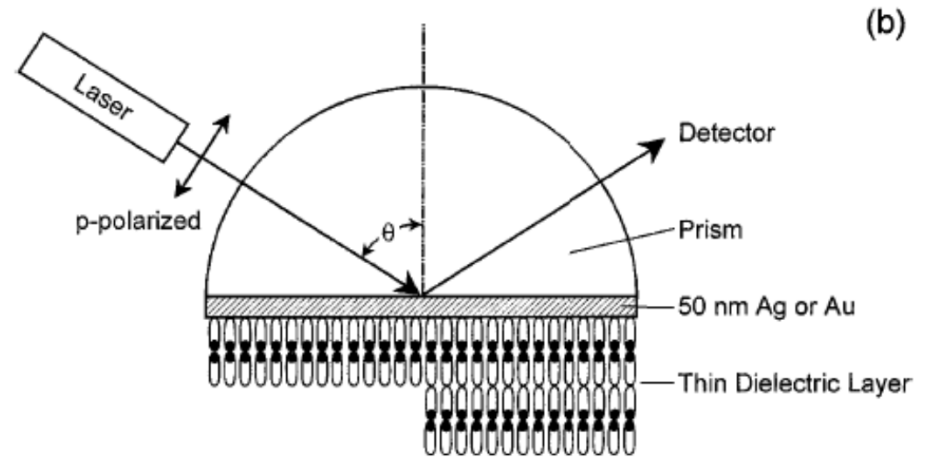
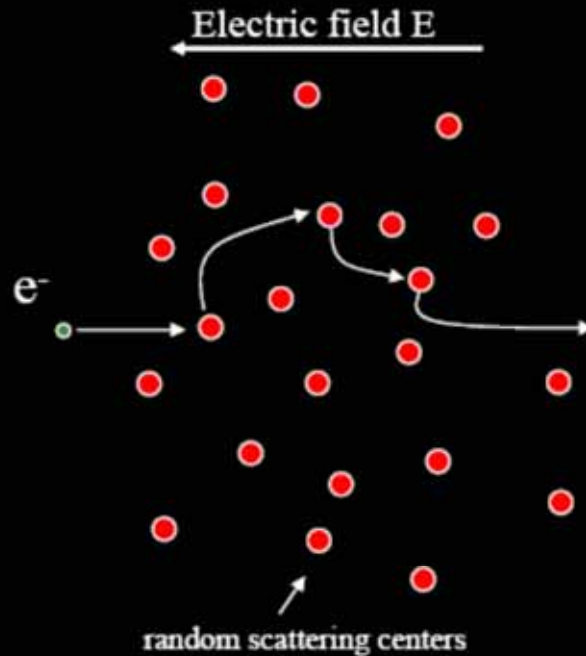


Figure 3. Schematics of an SPR experiment (top) and of the light-induced surface plasmons (bottom).



Drift: Drude model



$$F = ma$$

$$eE = m \frac{\partial v}{\partial t}$$

$$v_{avg} = \underbrace{\frac{e\tau}{m}}_{\mu} E$$

$$j = ne v_{avg} = \underbrace{\frac{ne^2\tau}{m}}_{\sigma} E$$

Last modified 4/2/2004

EECS 217C Nanotechnology © 2004 P. Burke

9

$$m \frac{\partial}{\partial t} \langle \vec{v} \rangle = q \vec{E} - \gamma \langle \vec{v} \rangle$$

$$\sigma(\omega) = \frac{\sigma_0}{1 + i\omega\tau}$$



AC Dielectric Response

$$\epsilon_m = 1 - \frac{\omega_p^2}{\omega^2}$$

Plasma frequency

polarizability of a small metal sphere with dielectric function $\epsilon(\lambda)$

$$\alpha = R^3 \frac{\epsilon - 1}{\epsilon + 2}.$$

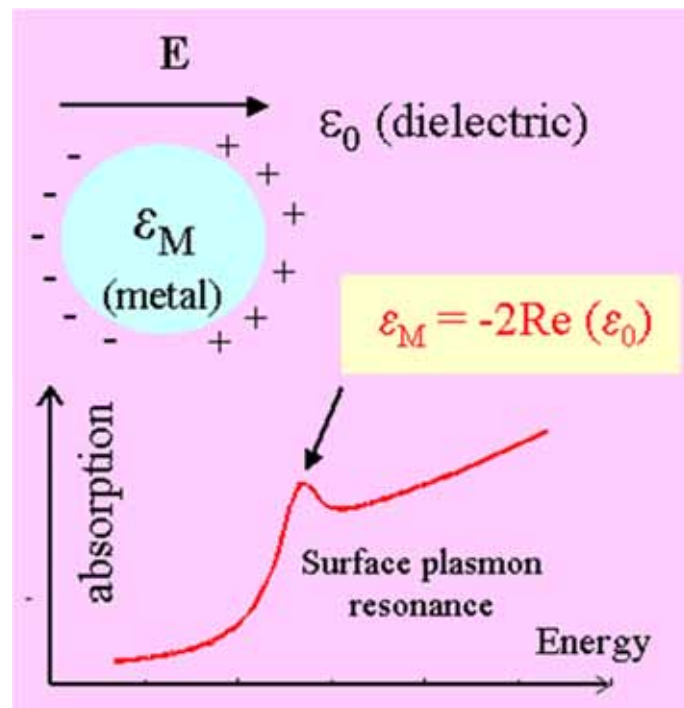
$$\epsilon = \epsilon_b + 1 - \frac{\omega_p^2}{\omega^2 + i\omega\gamma},$$

$$\alpha = \frac{R^3(\epsilon_b\omega^2 - \omega_p^2) + i\omega\gamma\epsilon_b}{[(\epsilon_b + 3)\omega^2 - \omega_p^2] + i\omega\gamma(\epsilon_b + 3)}.$$

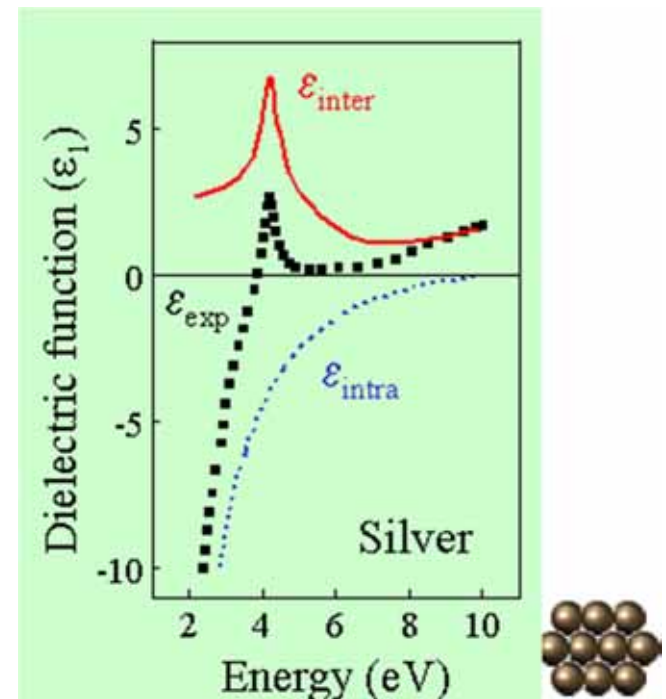
$$\omega_R = \frac{\omega_p}{\sqrt{\epsilon_b + 3}}$$

$$\gamma(\epsilon_b + 3).$$



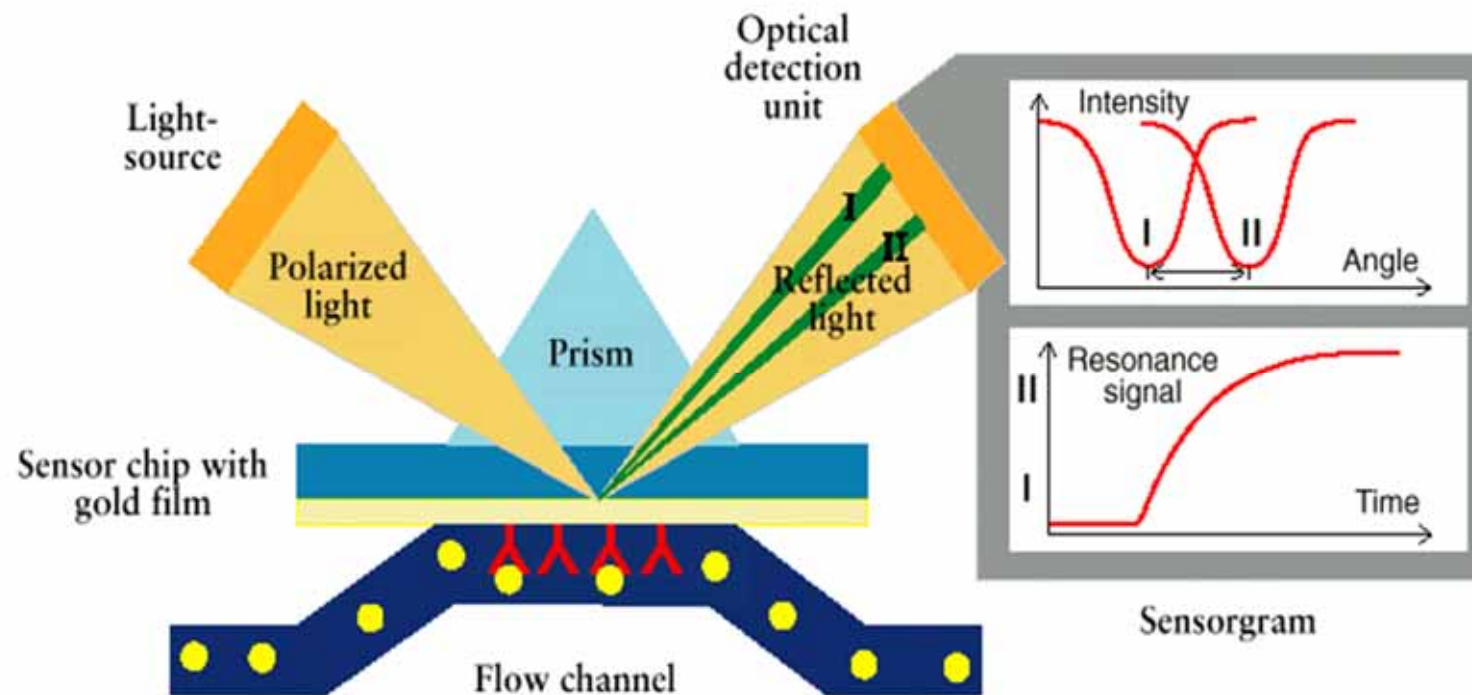


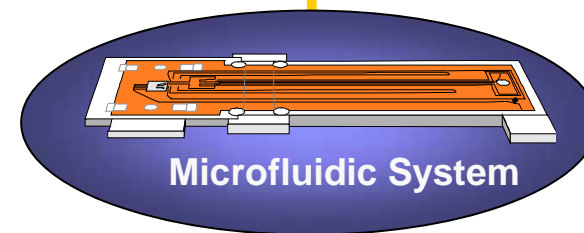
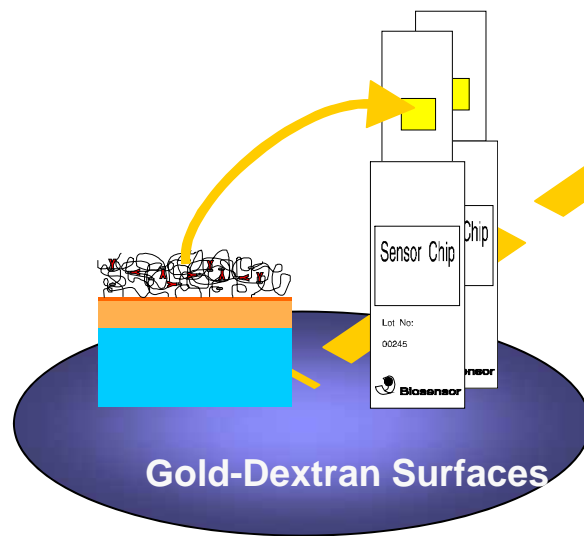
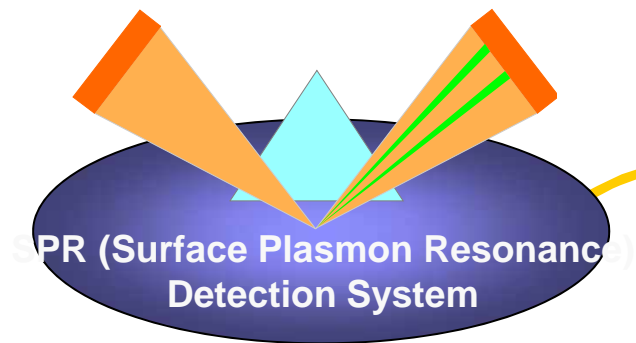
$$\epsilon_{eff} = \epsilon_0 + 3N\epsilon_0 \frac{\epsilon_M - \epsilon_0}{\epsilon_M + 2\epsilon_0}$$



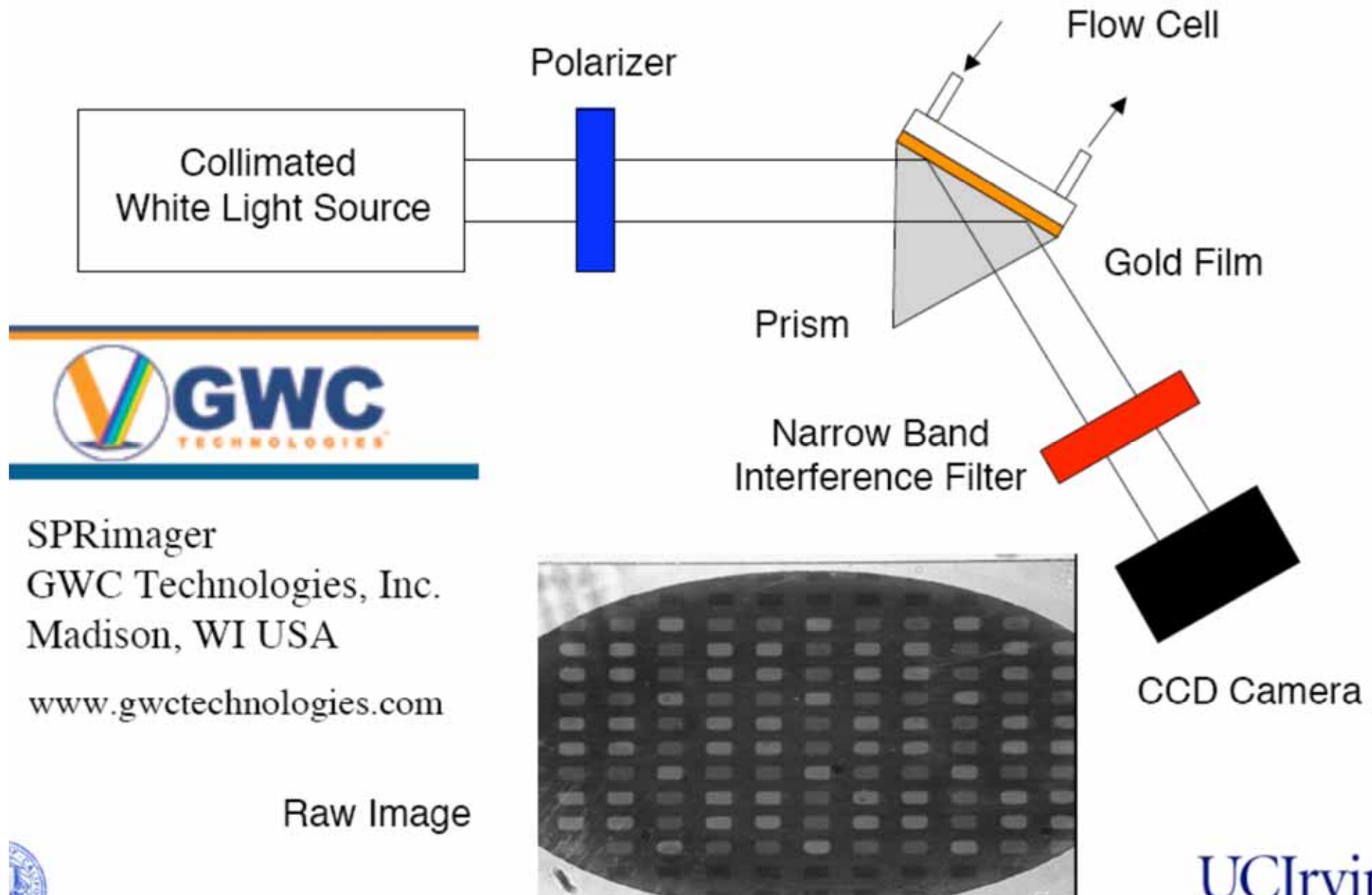
Biomolecular Binding in Real Time

Principle of Detection - SPR (Surface Plasmon Resonance)





SPR Imaging Apparatus



SPRimager
GWC Technologies, Inc.
Madison, WI USA

www.gwctechnologies.com

Raw Image



Localized Plasmon

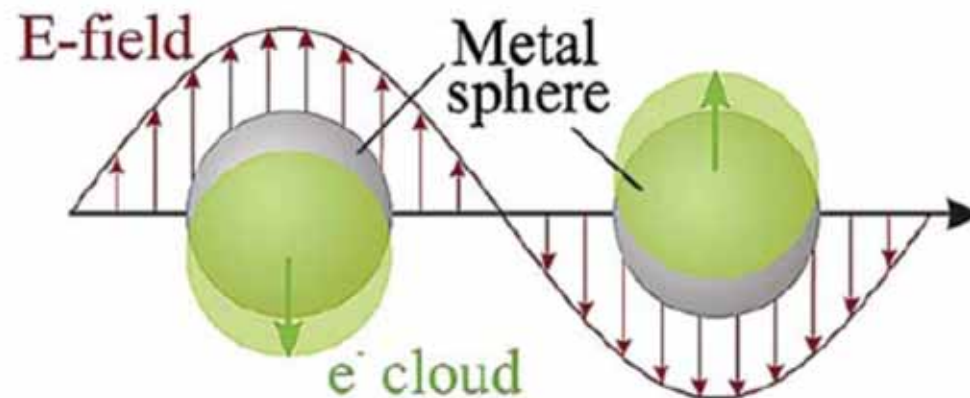
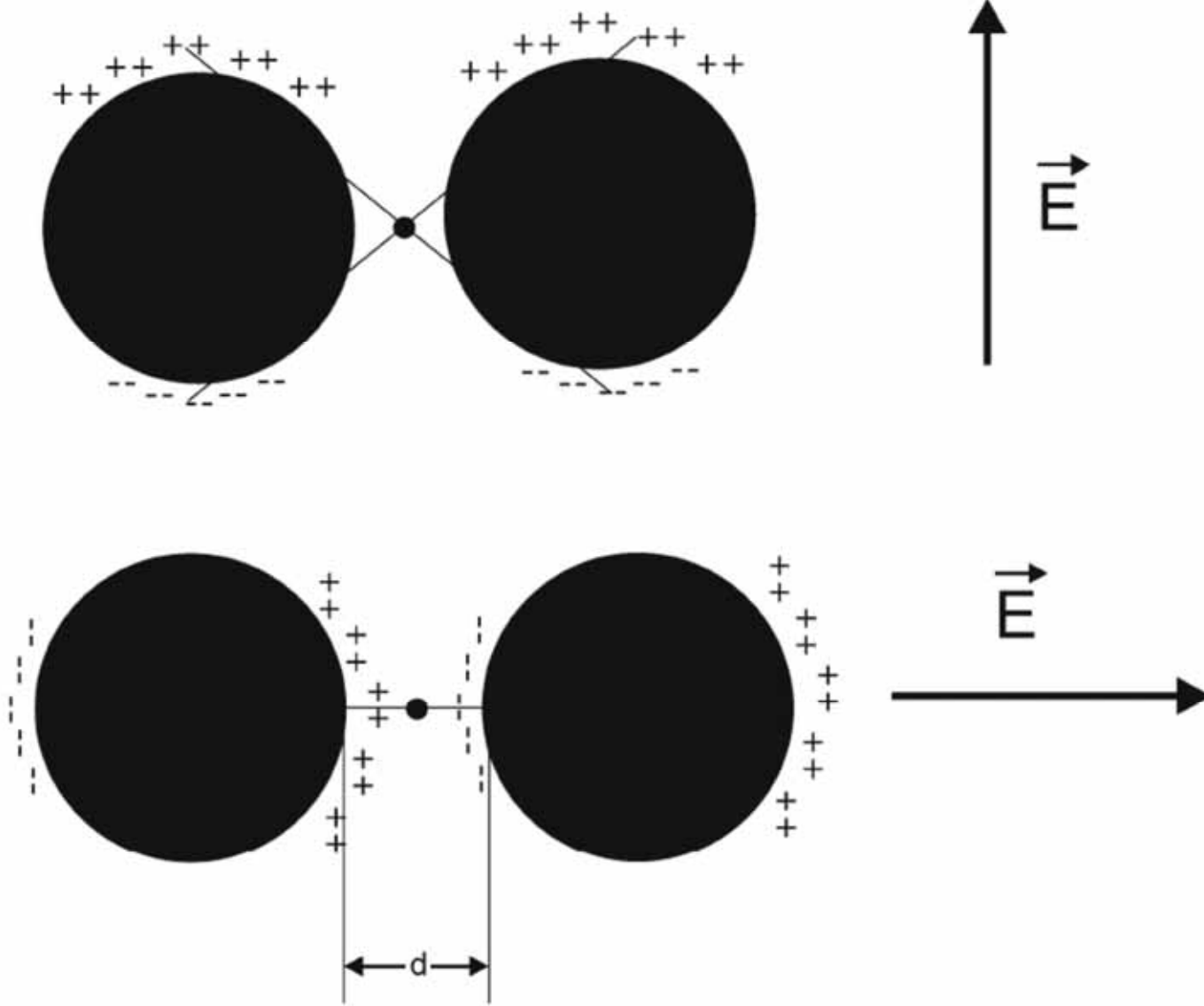


Figure 6. Schematic of plasmon oscillation for a sphere. From [39].





field enhancement

$E_s = gE_0$, where E_0 is the magnitude of the incident field.

$$E_R \propto \alpha_R E_s \propto \alpha_R g E_0$$

$$E_{\text{SERS}} \propto \alpha_R g g' E_0$$

$$I_{\text{SERS}} \propto |\alpha_R|^2 |g g'|^2 I_0$$

$$g \cong g'$$

$$|E_L|^4 = |g|^4.$$



Probing Single Molecules and Single Nanoparticles by Surface-Enhanced Raman Scattering

SCIENCE • VOL. 275 • 21 FEBRUARY 1997

Shuming Nie* and Steven R. Emory

Fig. 1. Single Ag nanoparticles imaged with evanescent-wave excitation. Total internal reflection of the laser beam at the glass-liquid interface was used to reduce the laser scattering background. The instrument setup for evanescent-wave microscopy was adapted from Funatsu *et al.* (11). The images were directly recorded on color photographic film (ASA-1600) with a 30-s exposure by a Nikon 35-mm camera attached to the microscope. (A) Unfiltered photograph showing scattered laser light from all particles immobilized on a polylysine-coated surface. (B) Filtered photograph taken from a blank Ag colloid sample (incubated with 1 mM NaCl and no R6G analyte molecules). (C) and (D) Filtered photographs taken from a Ag colloid sample incubated with 2×10^{-11} M R6G. These images were selected to show at least one Raman scattering particle. Different areas of the cover slip were rapidly screened, and most fields of view did not contain visible particles. (E) Filtered photograph taken from Ag colloid incubated with 2×10^{-10} M R6G. (F) Filtered photograph taken from Ag colloid incubated with 2×10^{-9} M R6G. A high-performance bandpass filter was used to remove the scattered laser light and to pass Stokes-shifted Raman signals from 540 to 580 nm (920 to 2200 cm^{-1}). Continuous-wave excitation at 514.5 nm was provided by an Ar ion laser. The total laser power at the sample was 10 mW. Note the color differences between the scattered laser light in (A) and the red-shifted light in (C) through (F).

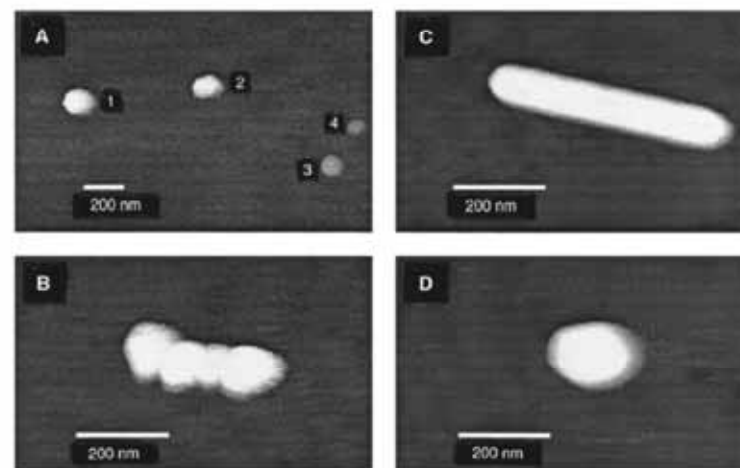
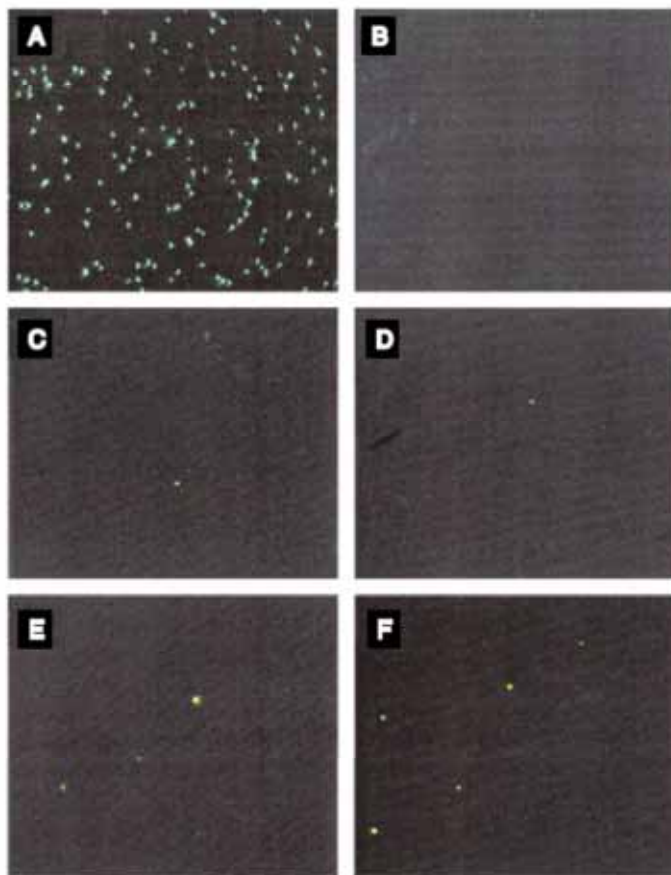
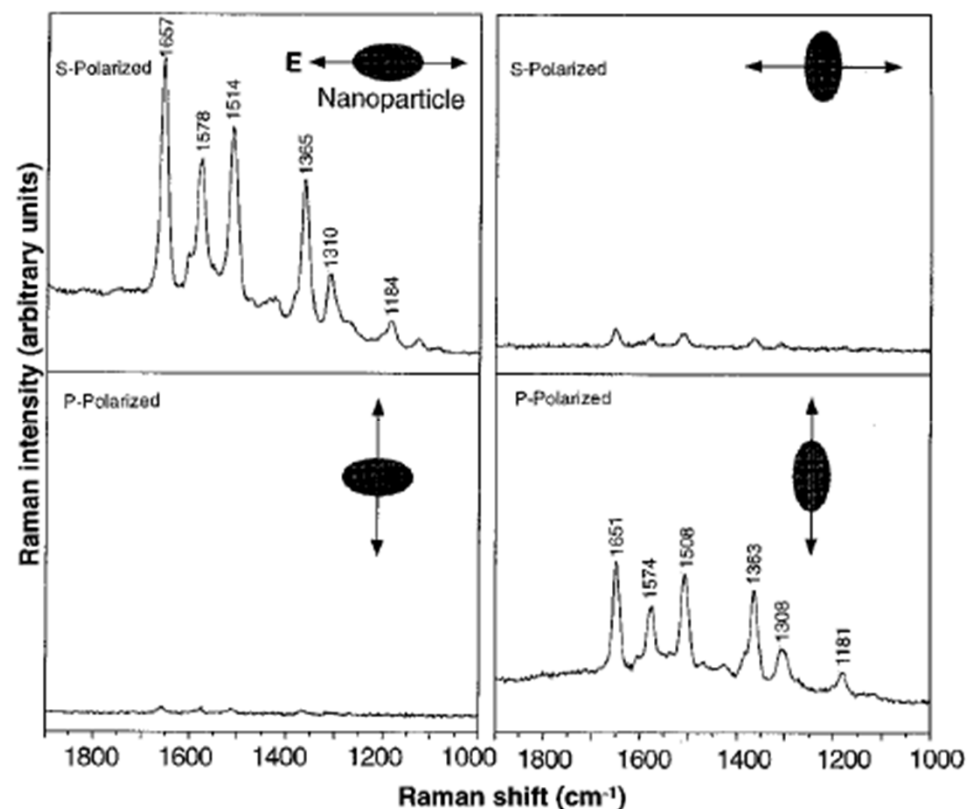


Fig. 2. Tapping-mode AFM images of screened Ag nanoparticles. (A) Large area survey image showing four single nanoparticles. Particles 1 and 2 were highly efficient for Raman enhancement, but particles 3 and 4 (smaller in size) were not. (B) Close-up image of a hot aggregate containing four linearly arranged particles. (C) Close-up image of a rod-shaped hot particle. (D) Close-up image of a faceted hot particle.



Fig. 3. Surface-enhanced Raman spectra of R6G obtained with a linearly polarized confocal laser beam from two Ag nanoparticles. The R6G concentration was 2×10^{-11} M, corresponding to an average of 0.1 analyte molecule per particle. The direction of laser polarization and the expected particle orientation are shown schematically for each spectrum. Laser wavelength, 514.5 nm; laser power, 250 nW; laser focal radius, ~ 250 nm; integration time, 30 s. All spectra were plotted on the same intensity scale in arbitrary units of the CCD detector readout signal.



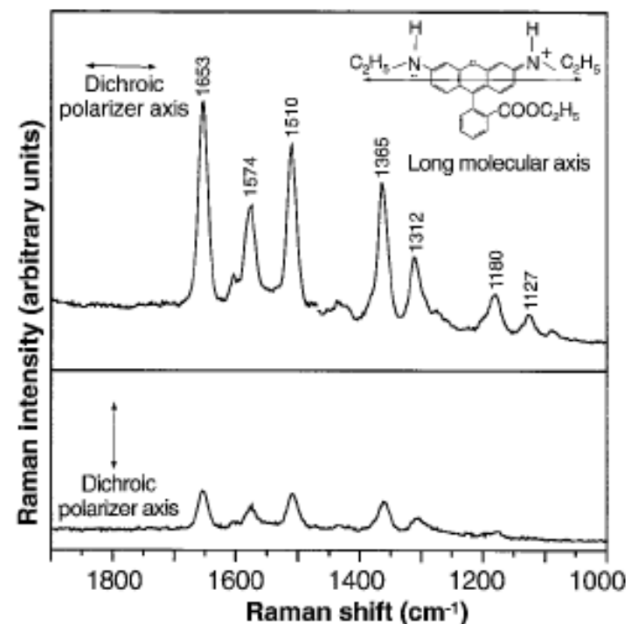


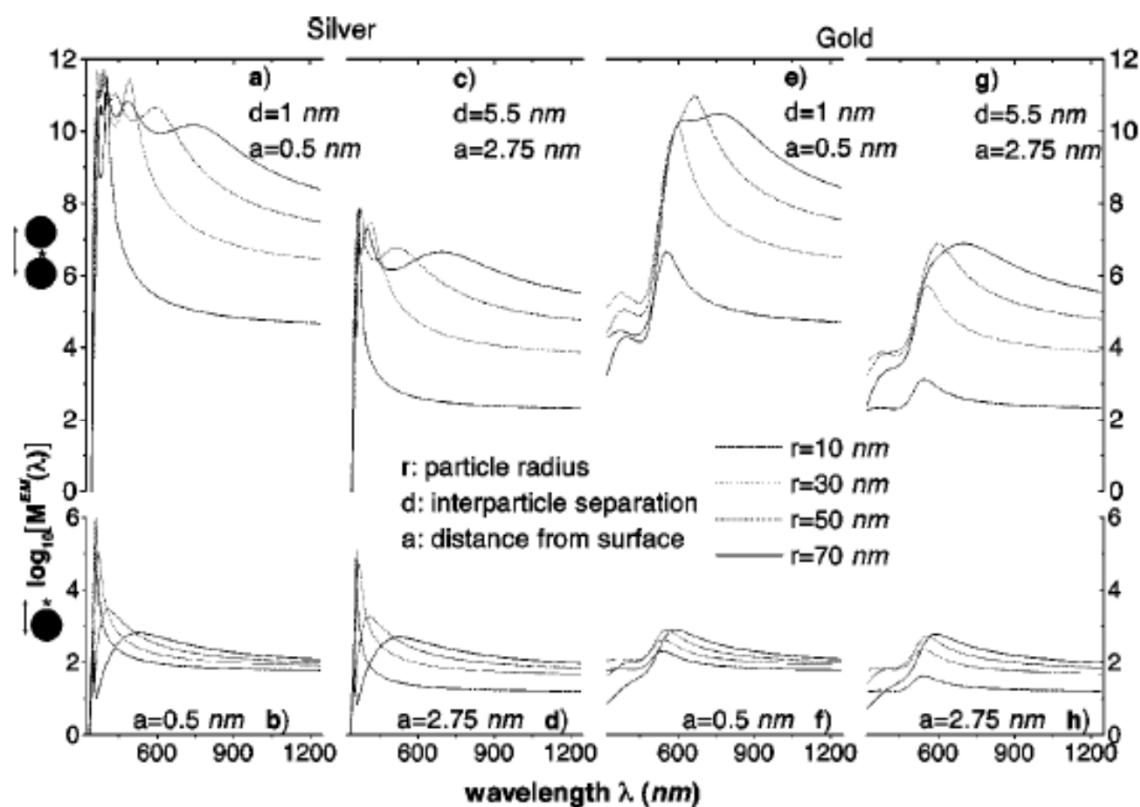
Fig. 4. Emission-polarized surface-enhanced Raman signals of R6G observed from a single Ag nanoparticle with a polarization-scrambled confocal laser beam. A dichroic sheet polarizer was rotated 90° to select Raman scattering signals polarized parallel (upper spectrum) or perpendicular (lower spectrum) to the long molecular axis of R6G. (**Inserts**) Structure of R6G, the electronic transition dipole (along the long axis when excited at 514.5 nm), and the dichroic polarizer orientations. Other conditions as in Fig. 3.

troscopic signatures of adsorbed molecules. For single rhodamine 6G molecules adsorbed on the selected nanoparticles, the intrinsic Raman enhancement factors were on the order of 10^{14} to 10^{15} , much larger than the ensemble-averaged values derived from conventional measurements. This enormous enhancement leads to vibrational Raman signals that are more intense and more stable than single-molecule fluorescence.



Electromagnetic contributions to single-molecule sensitivity in surface-enhanced Raman scattering

PRE 62 4318



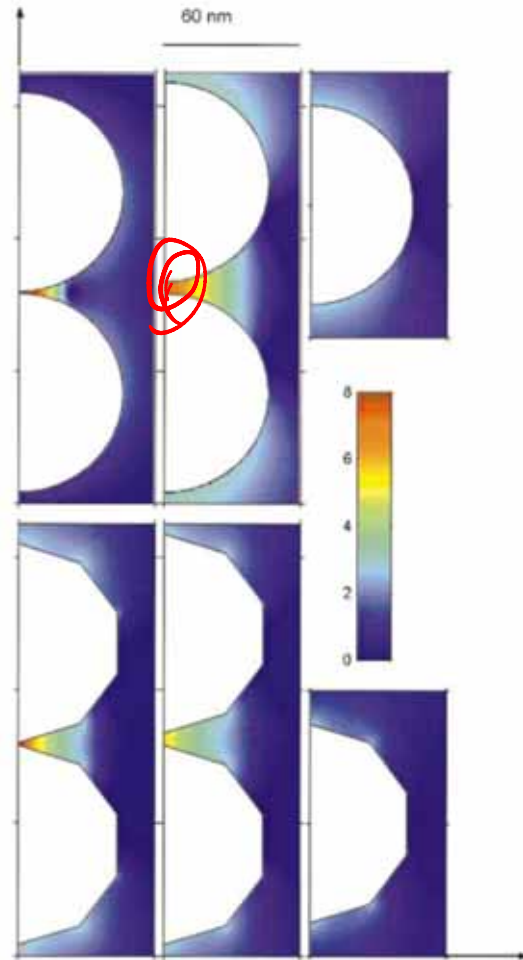


FIG. 3. (Color) EM-enhancement factor M^{EM} at a cross section through six different silver particle configurations. The wavelength of the incident field is $\lambda = 514.5$ nm with vertical polarization. The left-hand column illustrates the EM enhancement for dimer configurations of two spheres (top) and two polygons (bottom) with a separation of 1 nm. The middle column shows the same situation, but with a separation distance of 5.5 nm. The right-hand column shows the case of an isolated single particle. All particles share a common largest dimension of 90 nm. Note that the color scale from dark blue to dark red is logarithmic, covering the interval $10^0 < M^{EM} < 10^8$. Regions with enhancement outside this interval are shown in dark blue and dark red, respectively.

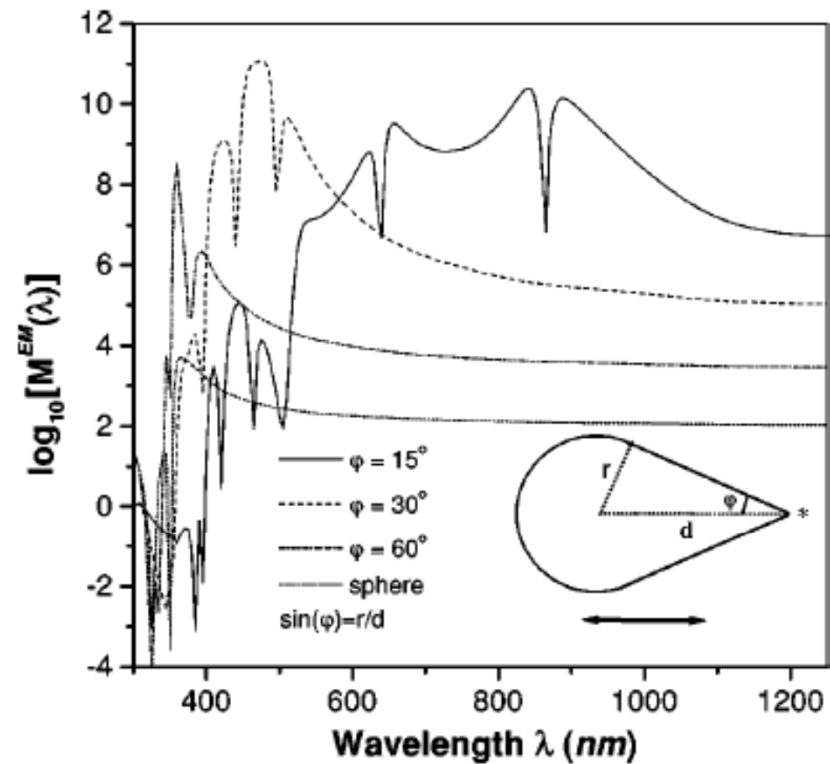


FIG. 5. EM-enhancement factor for a rotationally symmetric silver droplet as a function of the angle defining the opening edge ϕ . The field is polarized parallel to the axis of the droplet and the evaluation position (star) is located 0.5 nm outside the tip. As the droplet becomes sharper the enhancement increases several orders of magnitude.



Nanosphere Arrays with Controlled Sub-10-nm Gaps as Surface-Enhanced Raman Spectroscopy Substrates

J. AM. CHEM. SOC. 2005, 127, 14992–14993

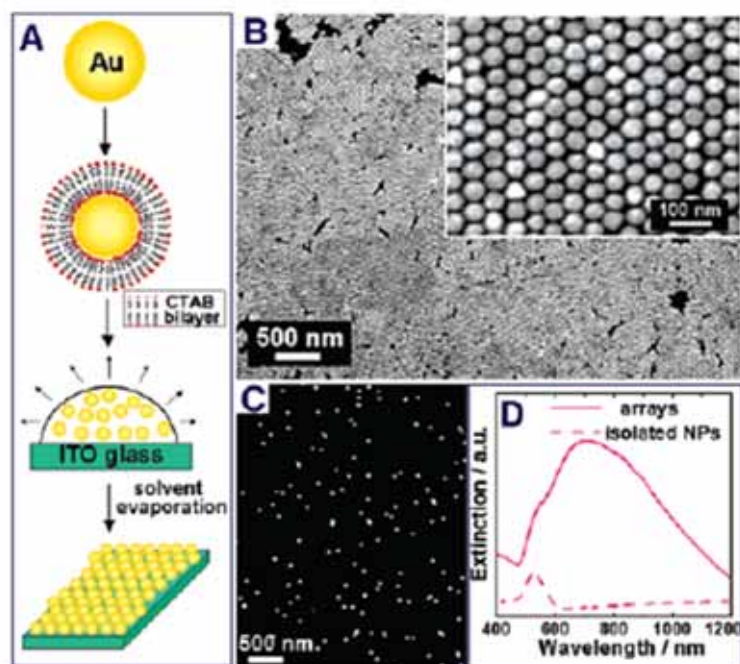


Figure 1. (A) Schematic illustration of the fabrication of sub-10-nm gap Au NP arrays. (B) SEM image of the arrays. (C) SEM image of monolayer of isolated Au NPs on ITO glass. (D) Vis-NIR extinction spectrum of the monolayer of isolated Au NPs and arrays.

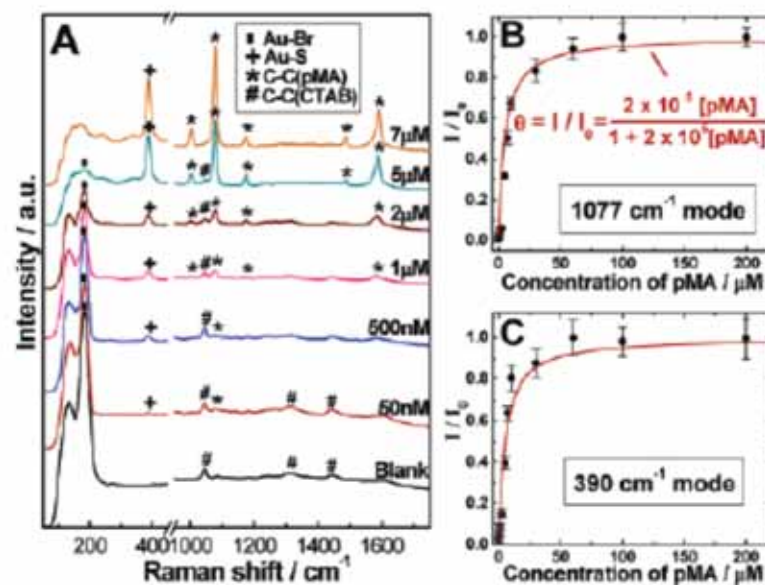


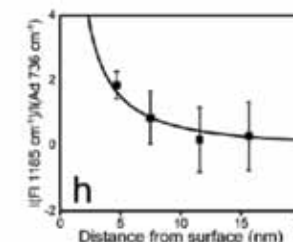
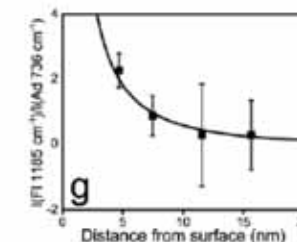
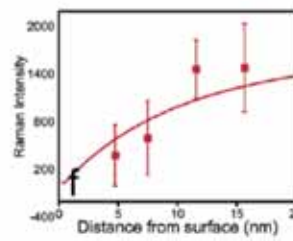
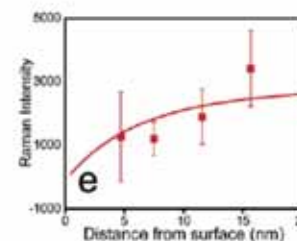
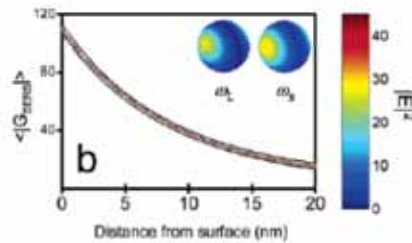
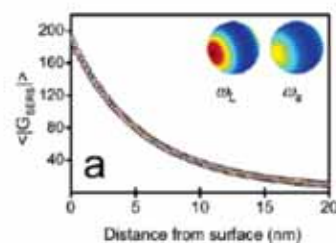
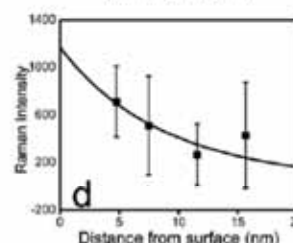
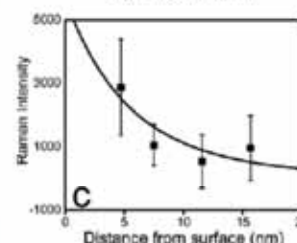
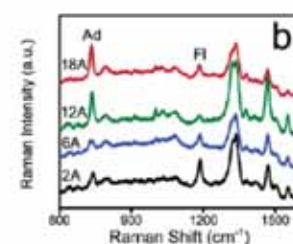
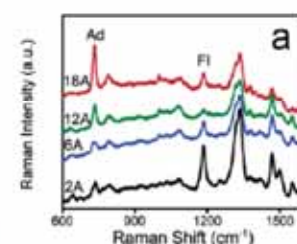
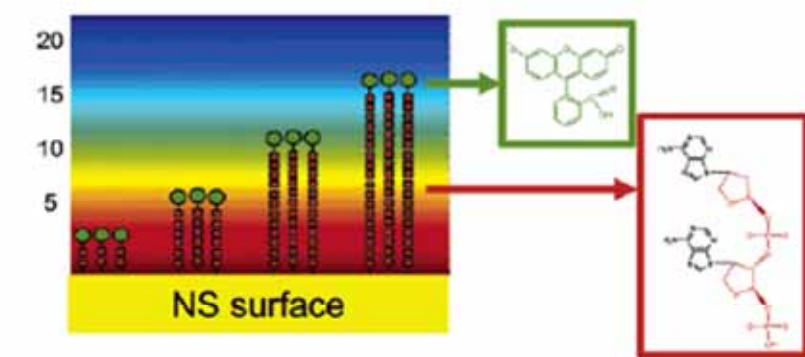
Figure 2. (A) SERS spectra of 5 μL of pMA with different concentrations deposited on the NP arrays. The excitation laser wavelength is 785 nm. Adsorption isotherm of pMA on the NP arrays obtained according to (B) 1077 and (C) 390 cm^{-1} modes in the SERS spectra. I_0 is the peak intensity of a saturated pMA monolayer.



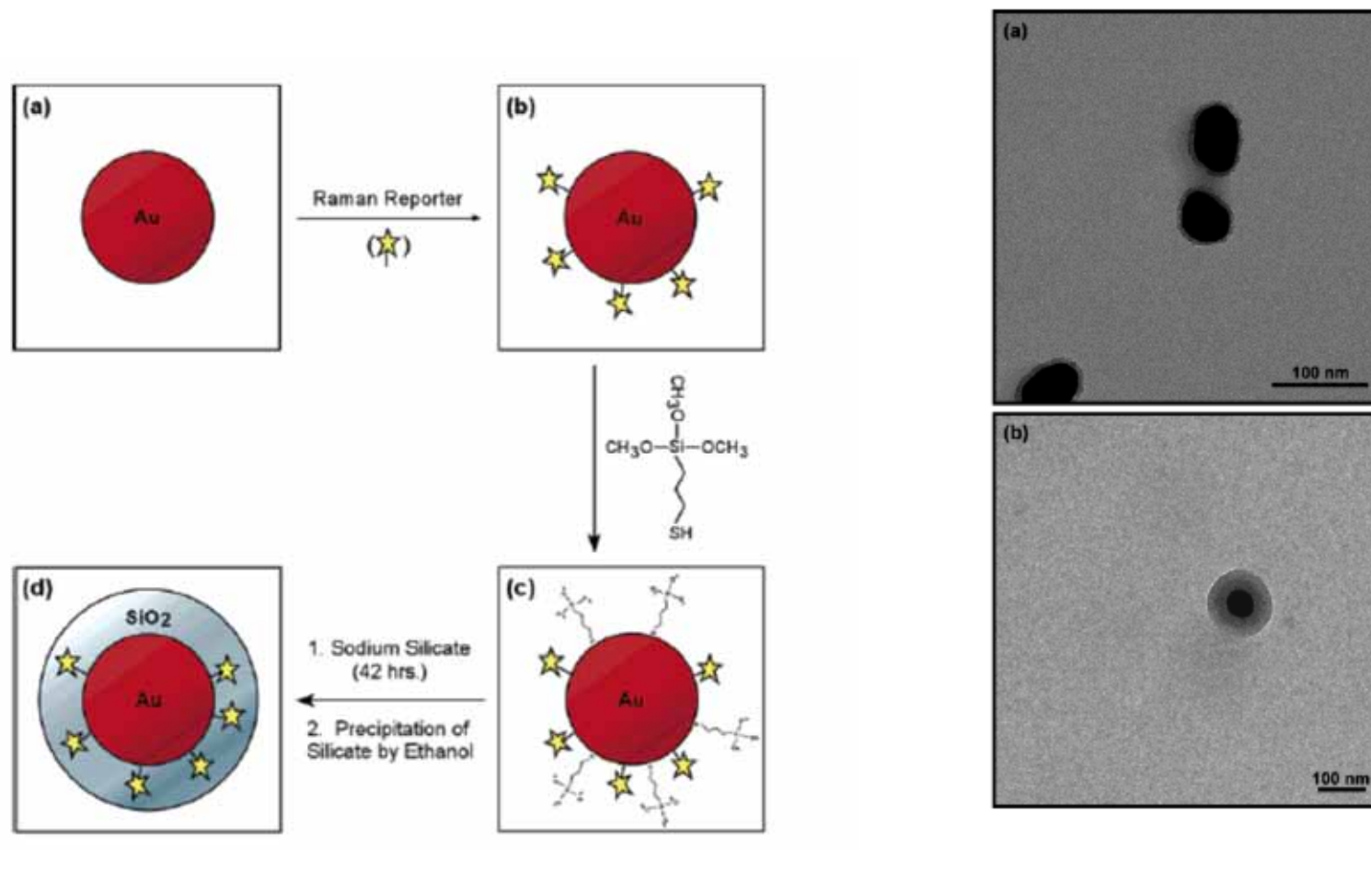
Profiling the Near Field of a Plasmonic Nanoparticle with Raman-Based Molecular Rulers

NANO
LETTERS

2006
Vol. 6, No. 10
2338–2343



Spectroscopic Tags Using Dye-Embedded Nanoparticles and Surface-Enhanced Raman Scattering



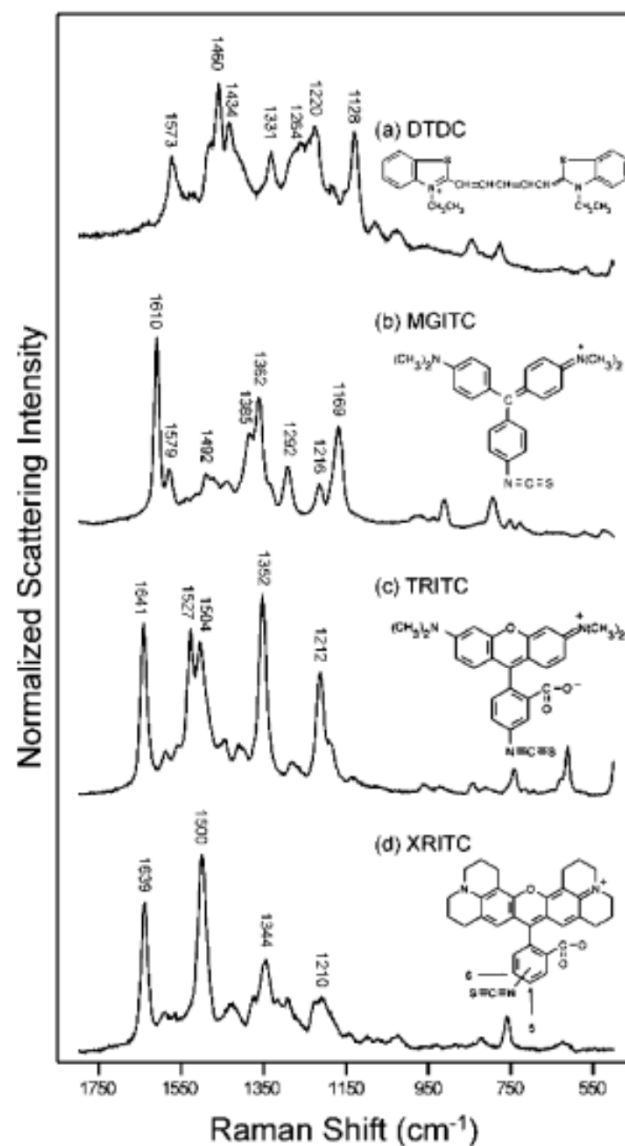
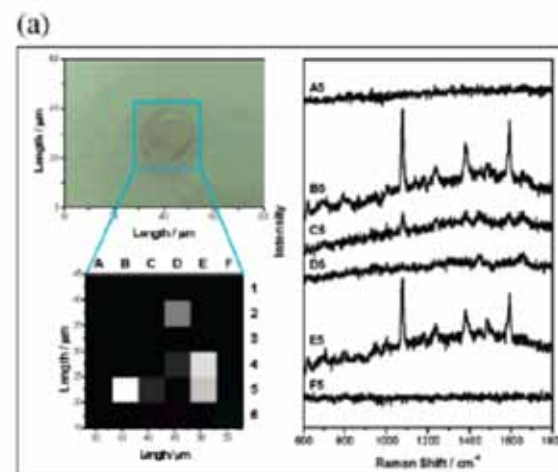
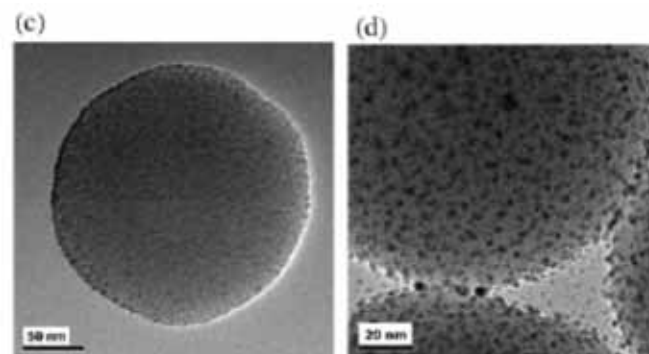
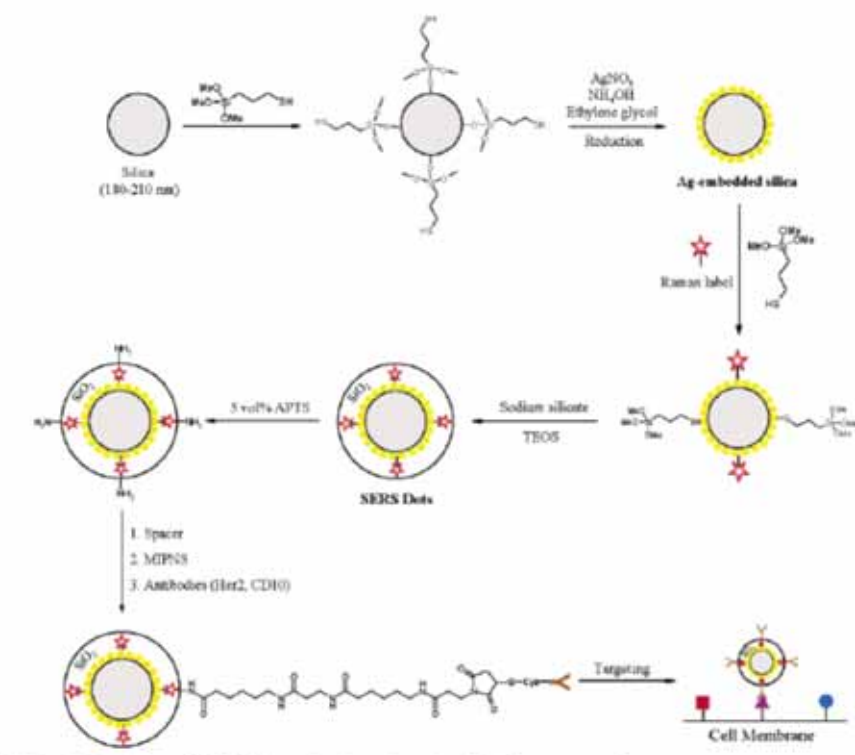


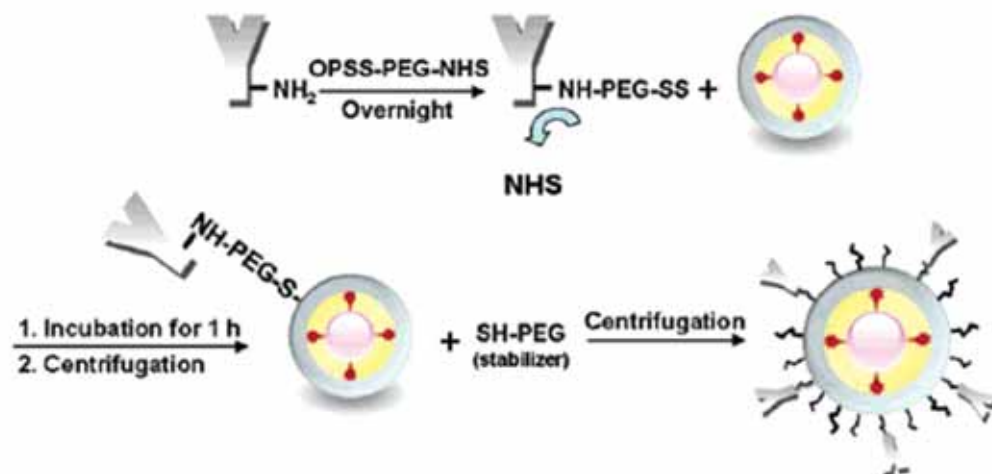
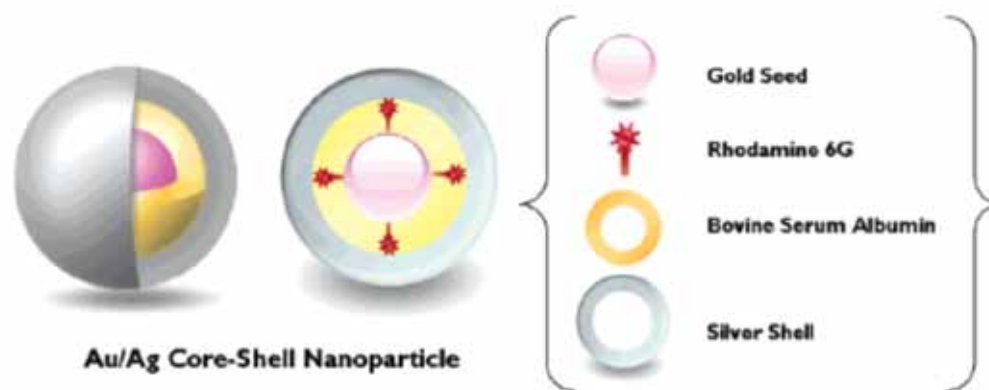
Figure 4. Chemical structures of four Raman reporters and their surface-enhanced resonance Raman spectra: (a) 3,3'-Diethylthiadicarbocyanine iodide (DTDC); (b) malachite green isothiocyanate (MGITC); (c) tetramethylrhodamine-5-isothiocyanate (TRITC); and (e) rhodamine-5-(and-8)-isothiocyanate (XRITC).



Nanoparticle Probes with Surface Enhanced Raman Spectroscopic Tags for Cellular Cancer Targeting



Biological Imaging of HEK293 Cells Expressing PLC γ 1 Using Surface-Enhanced Raman Microscopy



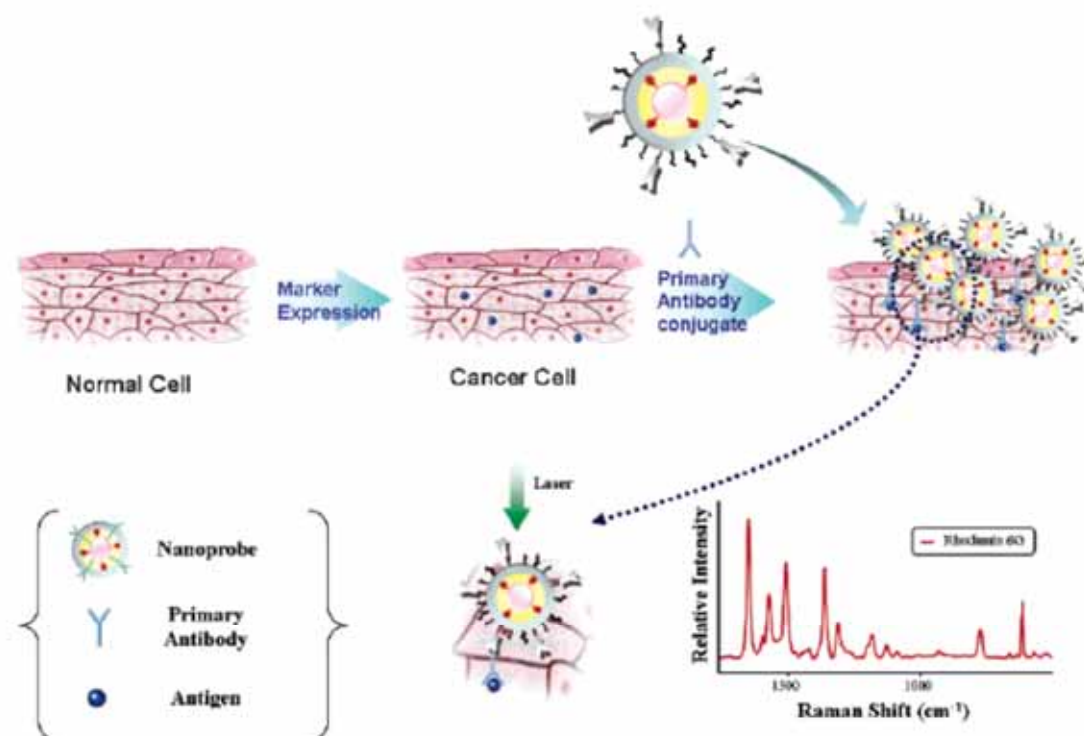


Figure 4. Schematic diagram depicting immobilization of Au/Ag core-shell nanoprobes on PLCγ1-expressing HEK293 cells and their SERS detection.

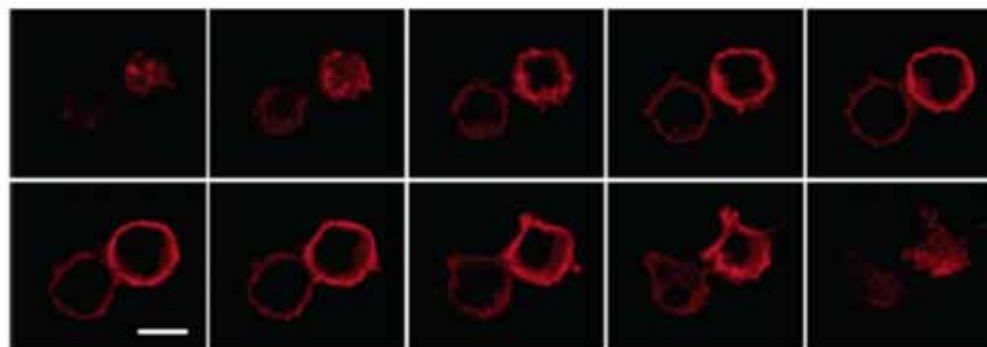


Figure 5. Serial fluorescence optical sections of PLCγ1-expressing HEK293 cells using red QDs. The z-axis interval of optical slices is 1.3 μm. Cells were incubated for 30 min in red QDs, after which the free QDs were washed away. These fluorescence images indicate that PLCγ1 markers are only expressed on the surface membranes. Scale bar, 10 μm.



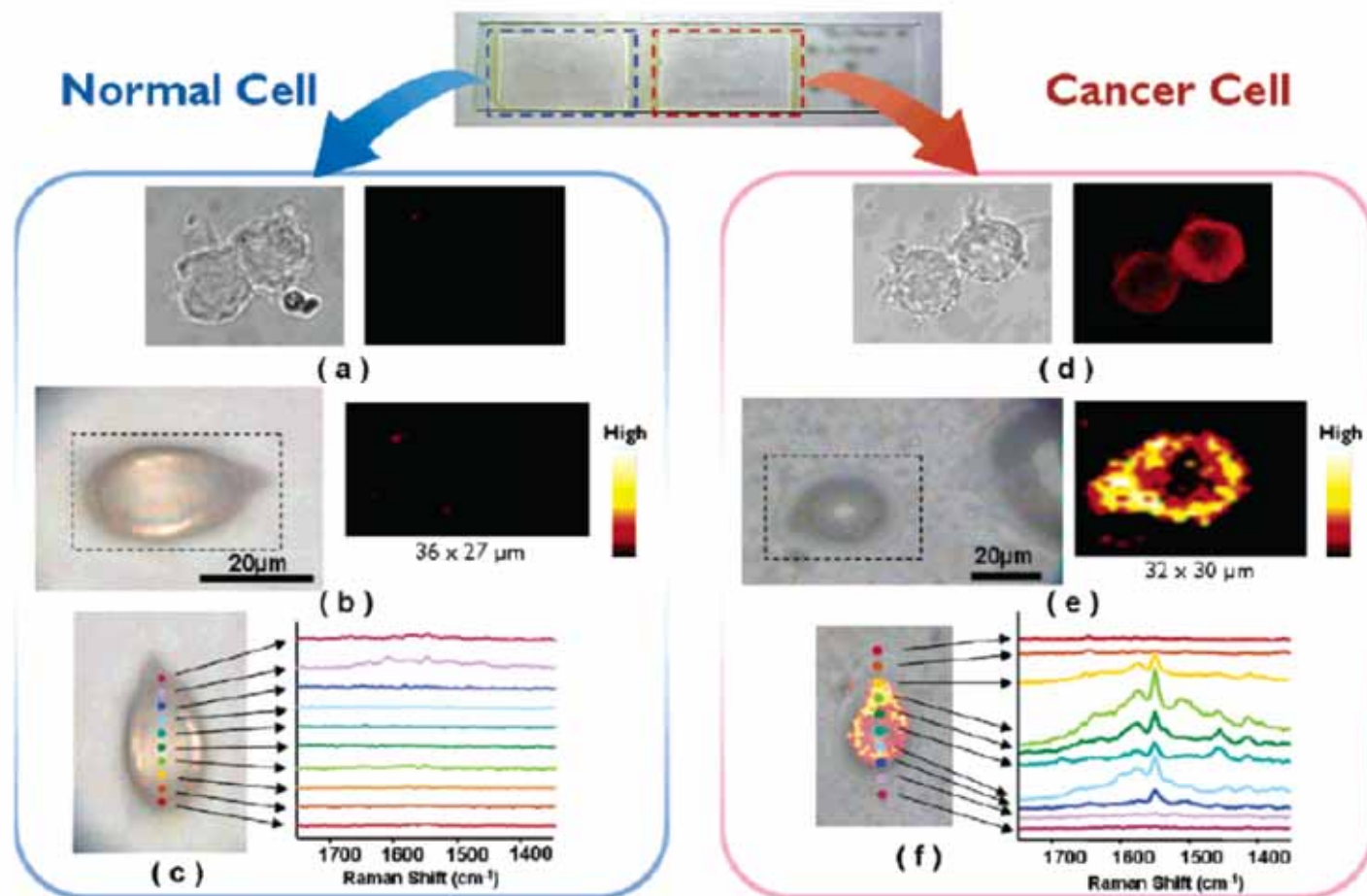


Figure 6. Fluorescence and SERS images of normal HEK293 cells and PLC γ 1-expressing HEK293 cells. (a) QD-labeled fluorescence images of normal cells: (left) brightfield image, (right) fluorescence image. (b) SERS images of single normal cell: (left) brightfield image, (right) Raman mapping image of single normal cell based on the 1650-cm $^{-1}$ R6G peak. The cell area was scanned with an interval of 1 μ m. Intensities are scaled to the highest value in each area. (c) Overlay image of brightfield and Raman mapping for single normal cell. Colorful spots indicate the laser spots across the middle of the cell along the y axis. (d) QD-labeled fluorescence images of cancer cells: (left) brightfield image, (right) fluorescence image. (e) SERS images of single cancer cell: (left) brightfield image, (right) Raman mapping image of single cancer cell based on the 1650-cm $^{-1}$ R6G peak. The cell area was scanned with an interval of 1 μ m. Intensities are scaled to the highest value in each area. (f) Overlay image of brightfield and Raman mapping for single cancer cell. Colorful spots indicate the laser spots across the middle of the cell along the y axis.



Mammalian Cell Surface Imaging with Nitrile-Functionalized Nanoprobes:
Biophysical Characterization of Aggregation and Polarization Anisotropy in
SERS Imaging

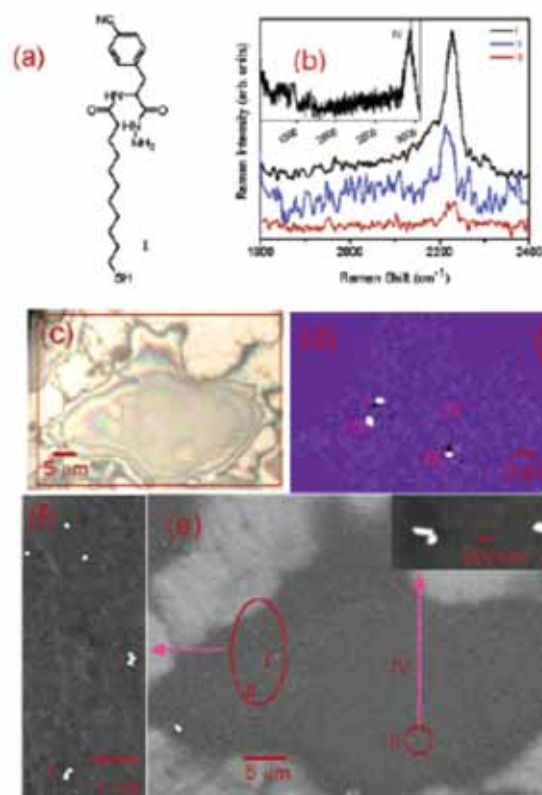


Figure 1. (a) The chemical structure of Raman reporter 1; (b) Raman spectra of the CN vibration mode extracted from positions I, II, and III of the cell shown in the optical image (c). Inset of (b) is a cellular Raman spectrum taken from spot IV of the same cell. (d) Raman intensity map of the C≡N band of the same cell, and (e) the corresponding SEM image. Inset in (e) showed the NPs in the lower right circle. (f) The group of NPs as shown in the large oval of (e).

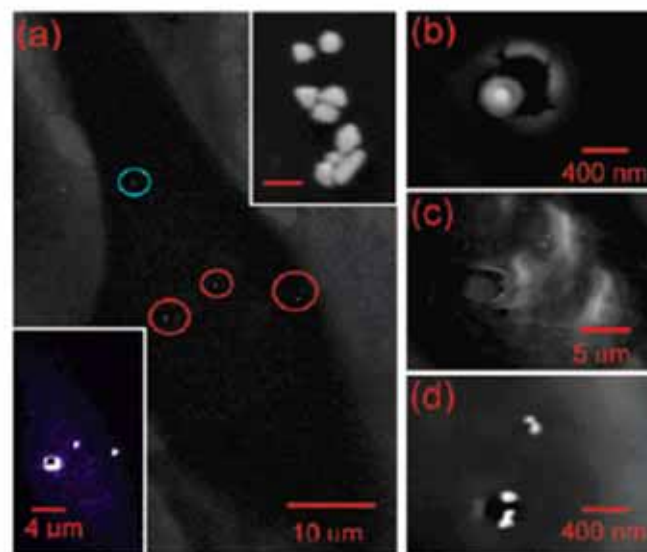


Figure 2. (a) SEM image of a cell. Upper right inset: magnification of a group of aggregated NPs. The scale bar is 200 nm. Lower left inset: the corresponding Raman intensity image of the same cell obtained with a power density of 10^5 W/cm². Laser-induced damage to the cell is shown in (b) the monomer (blue circle in a), (c) the aggregates, and (d) a pair of dimers.



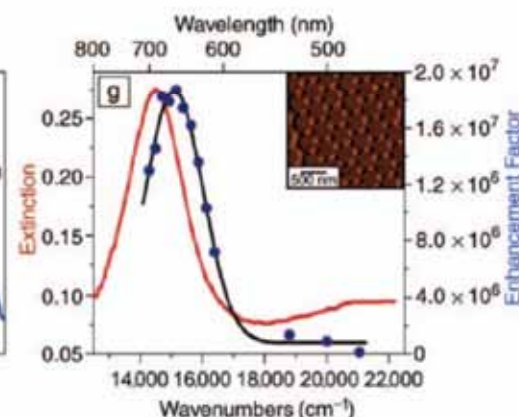
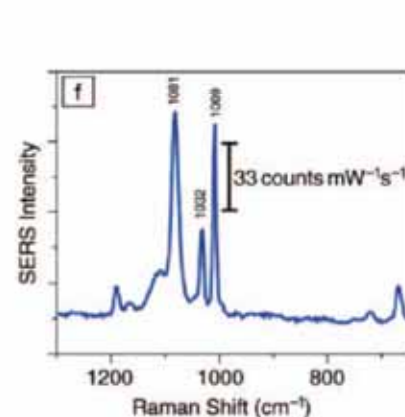
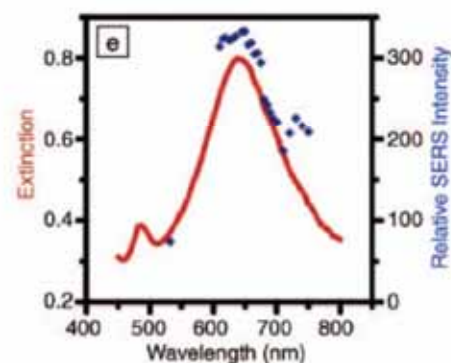
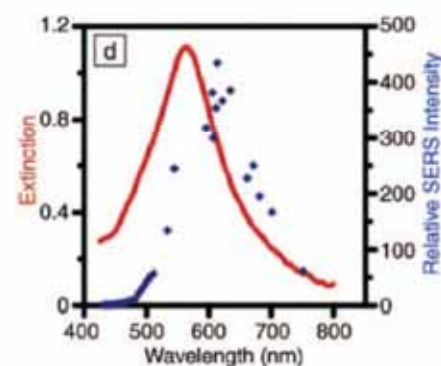
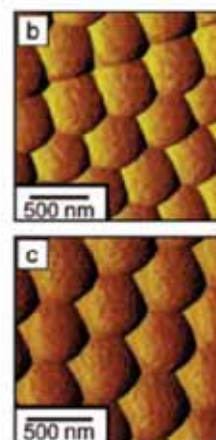
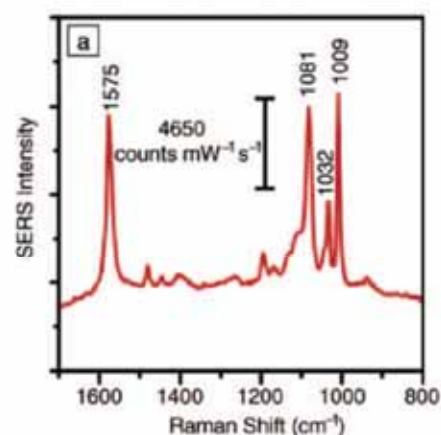


Figure 6. Localized surface plasmon resonance (LSPR), surface-enhanced Raman spectroscopy (SERS), and wavelength-scanned surface-enhanced Raman excitation spectroscopy (WS-SERES) results for benzenethiol adsorbed on Ag film-over-nanosphere (Ag FON) surfaces and nanoparticle arrays fabricated by nanosphere lithography (NSL). (a) SERS spectrum measured from Ag FON surface with excitation wavelength $\lambda_{\text{ex}} = 532$ nm, power = 3.0 mW, and 100 s data acquisition time. (b) Contact-mode atomic force microscopy (AFM) image of Ag FON surface (nanosphere diameter $D = 410$ nm, deposited mass thickness $d_m = 200$ nm) used for SERS in (a). (c) Contact-mode AFM image of Ag FON surface ($D = 500$ nm, $d_m = 250$ nm) used for WS-SERES in (e). (d) LSPR spectrum (solid line, $\lambda_{\text{max}} = 562$ nm, FWHM = 144 nm) and WS-SERES spectra (data points) for the 1081 cm^{-1} band of benzenethiol measured from the Ag FON surface in (b). (e) LSPR spectrum (solid line, $\lambda_{\text{max}} = 638$ nm, FWHM = 131 nm) and WS-SERES spectra (data points) for the 1081 cm^{-1} band of benzenethiol measured from Ag FON surface in (c). (f) SERS spectrum measured from Ag nanoparticle array surface ($\lambda_{\text{ex}} = 532$ nm, power = 3.0 mW, 100 s data acquisition time). (g) LSPR spectrum (solid line, $\lambda_{\text{max}} = 688$ nm, FWHM = 95 nm) and WS-SERES spectra (data points) for the 1081 cm^{-1} band of benzenethiol measured from a Ag nanoparticle array surface. (inset) Tapping-mode AFM image of a representative array surface.



Tip Enhanced Raman

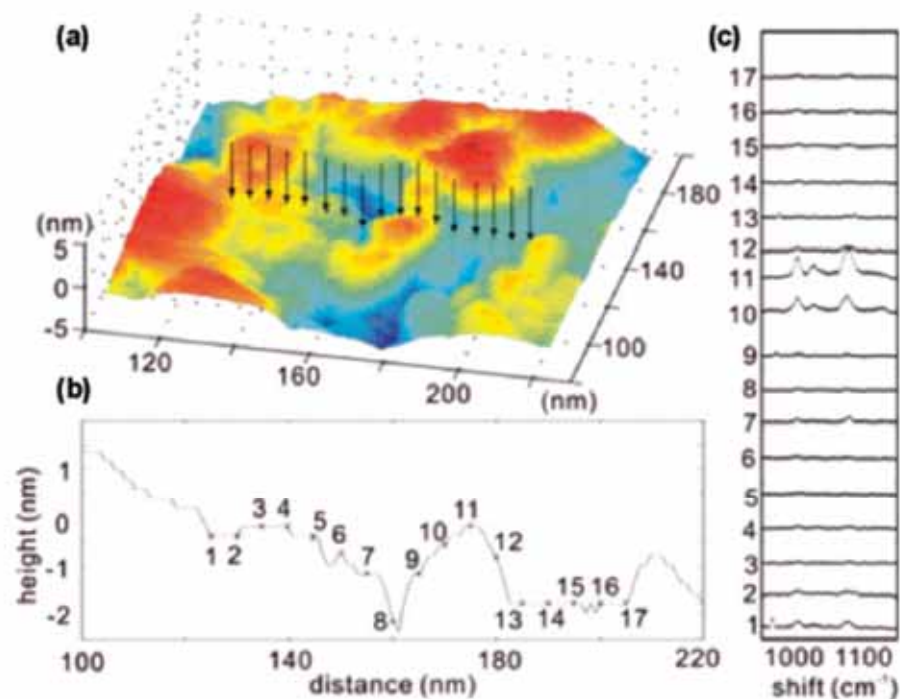


Figure 24. TERS mapping on a rough Au surface. An STM image of the sample is shown in a. TERS data was collected at the positions indicated by the arrows. The cross section of the topography image is shown in b, and the TERS collection sites are labeled with crosses. (c) Corresponding TERS sequence. The numbers denote the sites where the spectra were collected. Reprinted with permission from ref 463. Copyright 2007 American Chemical Society.

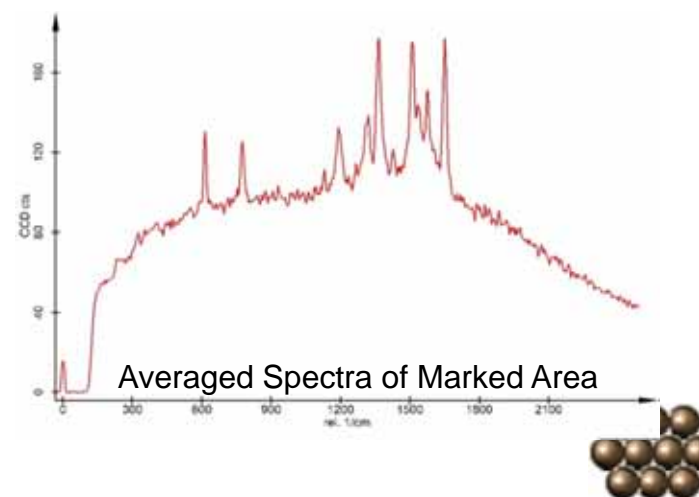
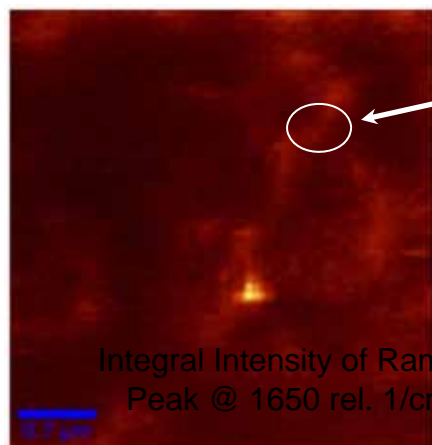
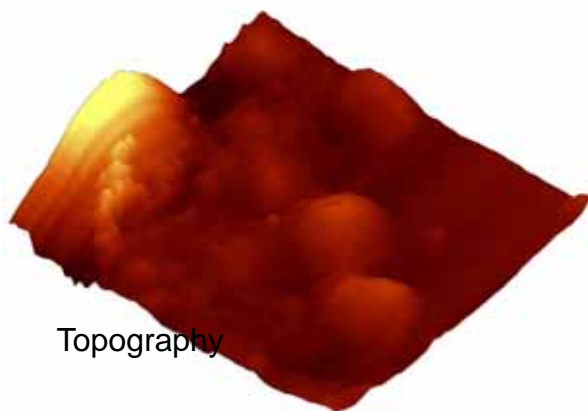


Near-Field Raman Microscopy

Droplet of AG nano particles labelled with Rhodamine 6G on cover glass

Experiment Parameters:

Excitation Laser:	532 nm
Scan Range:	4 μm x 4 μm
Resolution:	100 x 100 pixel
Integration Time:	110 ms per spectrum
Feedback:	SNOM AC Mode



Periodic Hole Array

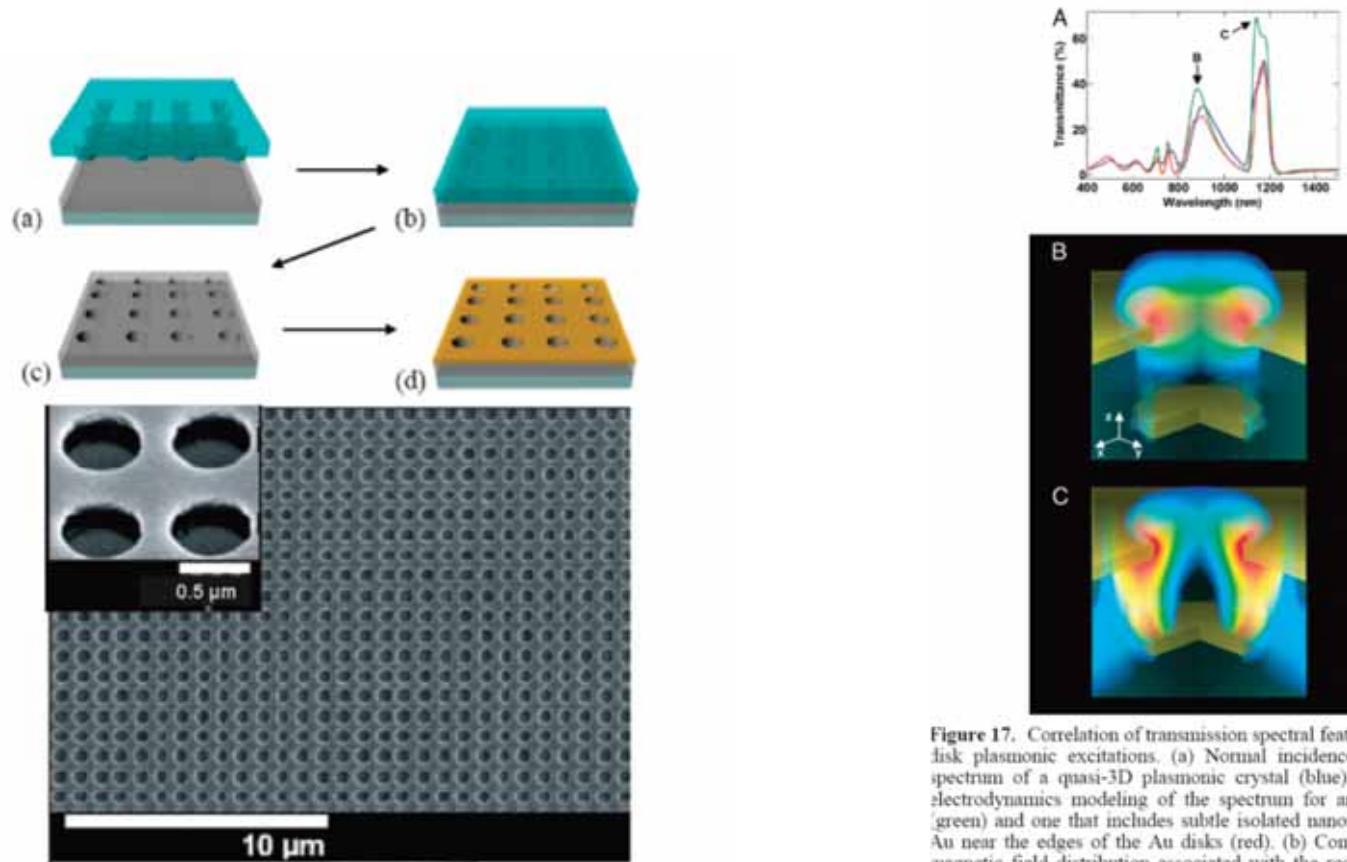


Figure 17. Correlation of transmission spectral features with hole/disk plasmonic excitations. (a) Normal incidence transmission spectrum of a quasi-3D plasmonic crystal (blue), and rigorous electrodynamics modeling of the spectrum for an ideal crystal (green) and one that includes subtle isolated nanoscale grains of Au near the edges of the Au disks (red). (b) Computed electromagnetic field distribution associated with the resonance at 883 nm (labeled B in a). The intensity is concentrated at the edges of the nanoholes in the upper level of the crystal. (c) Field distribution associated with the resonance at 1138 nm (labeled C in a), showing strong coupling between the upper and lower levels of the crystal. Reprinted with permission from ref 77. Copyright 2006 The National Academy of Sciences of the USA.



